Journal of the Electrochemical Society of India

Indian Institute of Science Campus,
Bengaluru - 560 012, India

Guest Editor

Dr. Rajalakshmi N

Vol. No. 73 (3&4), April-June 2024

CODEN - JESIA 73 [3&4] 2024 ISSN:0013-466X

INSTRUCTIONS TO AUTHORS

GENERAL

Address all manuscripts to the Managing Editor, Electrochemical Society of India,(JECSI) Bengaluru-560012 and send it by email to arunaecsi@gmail.com / ecsiiisc@gmail.com. Submission of an article will be taken to imply that it has not been previously published and is not under consideration for publication elsewhere. And further that if accepted, it will not be published elsewhere. Submit an electronic version of the paper in WORD format along with a pdf version in order not to miss any portion due to transmission faults. Identify the address, affiliation, email address of the author (corresponding author in case of multiple authors). Also, identify the category in which the paper qualifies for publication.

Journal of the Electrochemical Society of India (JECSI) is a multidisciplinary journal in the general area of Electrochemical Science and Technology. Research and review papers of general significance that are written clearly and well organized will be given preference. All submitted papers will be reviewed by three experts to determine suitability. Paper found unsuitable in terms of the overall requirements of the Journal and those not accepted by the reviewers will be returned to the authors. Both solicited and unsolicited papers will be reviewed. Authors will be notified of acceptance, rejection or any need for revision before acceptance for publication. Any illustrations or other material reproduced from other publications must be properly credited. It is the author’s responsibility to obtain the necessary permission in such cases.

CATEGORIES OF MANUSCRIPTS

General Articles, not exceeding 5000 words in length, should discuss current trends in research in a field that will be of interest to readers outside the field; interdisciplinary topics; Science policy and administration; Impact of Science and Technology on Society, etc. The paper should include a summary not exceeding 200 words, introductory paragraph(s), brief subheads at appropriate places to point to what follows, Illustrations that will help a general reader and references.

Review Articles, not exceeding 5000 words, are expected to survey and discuss recent developments in a relevant field. They should be well focused and organized. General text book style is not acceptable. Research Articles should report and discuss results of work of a fairly major significance. They should include an Abstract, introductory paragraph(s) and brief subheads indicating materials and methods used, major results and discussion of results, relevant illustrations and references.

Research Communications, not exceeding 2000 words, should contain important findings that are novel and are of fairly broad interest. They should not be broken up under subheads. Correspondences include letters, not exceeding 500 words that are of general interest to Scientist, Engineers and Technologists. Only selected letters will be published. Scientific Correspondence contains technical comments, including those on articles or communications published in JECSI. Appropriate letters will be published.

Book Reviews are reviews of books published in the major areas of Electrochemical Science, Technology and Engineering. Unsolicited reviews will also be considered. Reviews that simply ‘list’ the contents will not be acceptable for publication. Reviews should have ‘context’ and convey information about the subject of the book. Historical Comments and Notes inform readers about interesting aspects of personalities or institutions of Science or about watershed events in the history/ development of science. Most are expected to relate to India. Illustrations are welcome with due credit if already published elsewhere.

MANUSCRIPT PREPARATION

The manuscript should be in double line spacing in an area corresponding to A-4 size paper with 25 mm margin all around. Page numbers, including that for the first page should be given at the bottom centre of the page. The title should be brief, specific and amenable to indexing. Give a maximum of 5 keywords which are carefully chosen and not phrases of several words. Summary and abstract should not have more than 200 words and should convey the main point of the paper, outline the results and conclusions and explain the significance of the work and results.

Text

Papers should begin with an introduction. The text should be intelligible to readers in different disciplines and technical terms should be defined. Tables and figures should be arranged in numerical order and referred to in that order. All symbols and abbreviations must be defined and used only when absolutely necessary. Superscripts and subscripts and ambiguous characters should be clearly indicated. Units of measure should be metric and preferably SI. Methods should, as far as possible, be described briefly in appropriate table and figure legends.

Figures are to be drawn in sizes that are clearly intelligible. Location and orientation of figures is the entire responsibility of the author(s). The actual location of figures and tables may be clearly indicated in the pdf format that accompanies the main word format submission. The same data should not be given in both tables and figures. Photomicrographs and other photographs that require a scale bar or a micron marker should be defined clearly in the caption. Magnifications are not acceptable in place of micron markers. Primary data should be submitted as far as possible as for example actual photograph of an electrophoretic gel rather than an idealized diagram.

References should be numbered in the order in which they appear first through the text and then through table and figure legends. Following examples indicate the different ways of writing the references:

Reference to a journal publication:

[1] J. Name, J.A.J. Name, R.A. Name, Title of article, J. Sci. Commun. Vol.no (year) page number xx–xy. https://doi.org/10.1016/j.Sc.2010.00372.

Reference to a book:

[3] W. Name, E.B. Name, Title of the book, Edition, Publisher, Place name, year.

Reference to a chapter in an edited book:

[4] G.R. Name, L.B. Name, Chapter title, in: B.S. Name, R.Z. Name (Eds.), Title of book, Publisher, Place name, Year, pp. xxx–yyy.

Acknowledgments should be brief and clear.

Funding: This work was supported by Granting Agency Name [grant numbers xxxx, yyyy];

Cover Photographs. Good photographs (colour or black and white) that pertain to a submitted paper will be considered for use on the cover of an issue.

Proofs and Publication: A final pdf version of the paper may be sent to the author before publication if there are any inaccuracies or doubts of any nature. Such a procedure is redundant in case no major editorial changes are made in the paper.

Journal of the Electrochemical Society of India

Vol. No. 73 (3&4), April-June 2024
CODEN - JESIA 73 [3&4] 2024 ISSN:0013-466X
Email : ecsiiisc@gmail.com

E-mail : ecsiiisc@gmail.com

Publication Ethics and Publication Malpractice Statement

The Journal of Electrochemical Society of India (JECSI) follows the Committee on Publication Ethics (COPE) *Code of Conduct and Best Practice Guidelines for Journal Editors* and the *Code of Conduct for Journal Publishers*. It is expected that authors, reviewers and editors follow the best-practice guidelines on ethical behaviour.

Responsibilities of Editorial Board

Editors evaluate submitted manuscripts only on the basis of their merit such as novelty, originality, importance, and its relevance to the journal's scope. The information or ideas imparted to the editors due to handling the manuscript will be kept confidential and will not be used for their own benefit. The editors will refrain from reviewing a manuscript in which they have conflict of interest and will be handled by other editorial board members. Editors and editorial staff will maintain confidentiality about the submitted manuscripts.

All the manuscripts submitted to the journal will undergo peer-review by at least two reviewers who are experts in that area. Based on the evaluation reports received from the reviewers, copyright permissions and plagiarism will be checked and then the Chief Editor decides on the publication of the manuscript.

The Chief Editor will take actions when ethical concerns are raised with regard to a submitted manuscript or published paper followed by a correction, retraction, expression of concern or relevant other notes will be published in JECSI.

Responsibilities of Authors

The Authors should present detailed and correct account of the work to enable others to reproduce the work. Fraudulent or inaccurate statements are not accepted. If required the authors will be asked to provide the raw data of their study if some suspicious figures are provided in the manuscript. Authors should check their manuscript for originality check using the standard software. Only manuscripts with similarity report <20% will be considered for peer review. The authors should not simultaneously submit the same manuscript to multiple journals and is treated as unethical and such papers will be sent back to the authors and authors will be black listed.

Authors who have made significant contributions to the paper should only be included as authors in the manuscript and the role of each author has to be listed. The other peoples' name should be included in the acknowledgement section.

The authors should disclose the conflict of interest that would have influenced the results or their interpretation. Authors should also properly acknowledge the work of others and ensure proper citation of such works in the manuscript. The authors should clearly state in the manuscript if the work involved the use of hazardous chemicals, procedures or equipment. The authors should co-operate in submitting the revised manuscripts before the deadline and providing befitting replies to the reviewer comments.

The authors should inform the Chief Editor when they discover significant errors or inaccuracies in their own published work and publish a corrigendum or retract the paper.

About Guest Editor

Dr. N. Rajalakshmi
Former Senior Scientist and Head,
Centre for Fuel Cell Technology, ARCI, IIT Madras Research Park, Chennai - 600 113

After obtaining Ph.D in Physics from IIT, Madras, she worked as post doctoral fellow in TH Darmstadt, Germany and University of Geneva, Switzerland for about 8 years. She has worked on various aspects of Hydrogen economy like production, storage and utilization.

She has gained vast experience in Fuel cell technology both in Material aspects and Engineering challenges from SPIC Science foundation and Center for Fuel cell Technology, ARCI for the past 20 years. She has received the Technology award from Spic Science Foundation, Bharat Vikas Award from Institute of Self-Reliance for clean energy generation, Nature publishing award etc.,

She has chaired many sessions and given invited talks in various International conferences on Fuel cell science, Engineering technology, Gordon Research Conference on Fuel cells, Society of Automobile Engineers etc., in India and Abroad. She is a reviewer for many journals related to Hydrogen and / Fuel cells.

Member of Working group, Hydrogen utilization, IEEJ, Japan, American chemical society, International Association of Hydrogen energy, Materials Research society of India, Electrochemical society, and Indian society of Fuel cell Technologists. She was a visiting scientist of Korea Research Institute of Chemical technology, South Korea under the Brain pool program.

She has about 200 publications in various International Journals, 10 book chapters and 25 patents to her credit.

She is a Top2% of the world Scientists from India by Stanford University ranking during 2020 & 2021.

She is a DST nominated representative in the Hydrogen energy projects at National and International level and also a member of National Hydrogen Mission, Professor of practice at IITDh, Advisor for Deakin University, Australia, CSTEP, Bangalore, a few startups in H_2 technology.

Journal of The Electrochemical Society of India

CODEN JESIA 73 (3 & 4) April-June 2024. ISSN 0013-466X

Chief Editor, JECSI

Dr. U. Kamachi Mudali
Vice Chancellor, Homi Bhabha National Institute, DAE, Mumbai

Managing Editor

Dr. S.T. Aruna, CSIR-NAL, Bengaluru

Editors

Prof. A. Chitharanjan Hegde	NITK, Surathkal
Dr. Francesca Deganello	CNR ISMN - Institution Perlo Studio Dei Materiali Nanostrutturati, Italy
Prof. Jyotsana Mazumdar	IIT Kharagpur
Prof. Michael Rowherder	Max Planck Institute for Iron Research, Dusseldorf, Germany
Dr. S. Ningshen	Indira Gandhi Centre for Atomic Research, Kalpakkam
Prof. Palani Balaya	National University of Singapore, Singapore
Prof. M.V. Sangaranarayanan	IIT Madras, Chennai
Prof. M.G. Sethuraman	Gandhigram Rural University, Gandhigram
Dr. T.M. Sridhar	University of Madras, Chennai
Dr. S. Vasudevan	CSIR-Central Electrochemical Research Institute, Karaikudi

Editorial Advisory Board

Dr. S.T. Aruna	**Chairman, CSIR-NAL, Bengaluru**
Dr. U. Kamachi Mudali	**Chief Editor, Homi Bhabha National Institute, Mumbai**
Prof. E.S. Dwarakadasa	Former Chief Editor, IISc, Bengaluru
Dr. Nagaswarupa H.P.	Former Managing Editor, Davanagere University
Prof. S. Sampath	IISc, Bengaluru
Dr. B.S. Prathibha	BNMIT, Bengaluru
Prof. V.S. Raja	IIT Bombay
Prof. Alka Sharma	University of Rajasthan
Mr. Deepak Parab	Metrohm India, Chennai
Mr. Rajeeva Deekshit	Pyro Technologies, Bengaluru

Patrons of the Society

M/S Ronuk Industries
M/S Titanium Equipment and anode Mfg. Co.,
M/s Reliance Engineers, Bengaluru
M/s Degussa Electroplating Company
M/s B. T. Solders Pvt. Ltd., Mysore
M/s Khoday India Ltd., Bengaluru
M/s Metrohm India Pvt Ltd.
Ms. Mridula Shaw
Dr. C. H. Krishnamurthy Rao
Sri. S. K. Jain
Dr. Franz Simon
Sri. Arvind Toshniwal
Dr. N. Rajalakshmi, Former Head, CFCT, ARCI
Sri. Srihari Khoday
Sri. Deepak Parab

Donor Members

M/s. Mascot Chemical Works, Bengaluru
M/s. Indian Telephone Industries Ltd., Bengaluru
M/s. Kangovi Electronics (P) Ltd., Bengaluru
M/s. Aquair Control Systems, Bengaluru
M/s. Stiver Equipment Pvt. Ltd., Bengaluru
M/s. Hindustan Aeronautics Ltd., Bengaluru
M/s. High Energy Batteries, Madurai
M/s. Electroplating Equipment Co., Bengaluru
M/s. Galvanosols Pvt. Ltd., Bengaluru
M/s. Pyro Technologies, Bengaluru
M/s. Shruthi Enterprises, Bengaluru
M/s. Grauer Weil (India) Ltd., Mumbai
M/s. Zaveri Brothers (P) Ltd., Mumbai
M/s. Standard Batteries, Mumbai
M/s. Geep Industries Syndicate Ltd.
M/s. Larsen and Toubro Ltd., Mysore
M/s. IR Technology Services Pvt. Ltd.
M/s. Brite Platers and Electrical Engineers, Bengaluru
M/s. Vijaya Metal Finishers, Bengaluru
M/s. Vinpla Plating Pvt. Ltd., Bengaluru
M/s. Surface Chem Finishers, Bengaluru

Permanent Sustaining Members

M/s. Tata Chemical
M/s Ashok Charitable Trust, Karaikudi
M/s. Mysore Paper Mills, Bhadravathi
M/s. Tata Iron and Steel Company Ltd., Jamshedpur
M/s. DCM Chemical Works
M/s. Indian Aluminum Company Ltd., Alwaye
M/s. Visveswaraya Iron and Steel Ltd., Bhadravathi

Functionalized Acetylene Black as an Effective Additive for ORR Electrocatalysts

Sruti Muralikrishnan[a,b], P. SahanaDevi[a,b], Raman Vedarajan[a], Y. Vidyalakshmi[b,], K. Ramya[a]*

[a] Centre for Fuel Cell Technology, International Advanced Research Centre for Powder Metallurgy and New Materials, 2nd Floor IITM Research Park, Chennai, 600113, India

[b] Anna University, Chennai 600025, India

*Corresponding Authors: *vedarajan.raman@arci.res.in*

Abstract

Platinum-based electrocatalysts are the most effective materials for Oxygen Reduction Reaction (ORR) in Polymer Electrolyte Membrane (PEM) fuel cells. However, limitations in adapting platinum-based electrocatalyst have greatly hampered fuel cell commercialization. Therefore, studies on functionally active materials and additives have gained significant interest recently, as their addition can partially replace platinum content in the electrocatalysts. Herein, for the first time, we demonstrate the use of Functionalized Acetylene Black (FAB) as an additive to reduce the platinum content in a commercial catalyst 20% Pt/C (Vulcan XC-72). An optimized electrocatalyst recipe was determined by carrying out cyclic voltammetry studies, linear sweep voltammetry, and accelerated degradation test. The optimized electrocatalyst containing 15 wt% of FAB added to the commercial catalyst exhibited better performance than the commercial catalyst, with the platinum content reduced to 17% from 20%. This research concludes that functionalized acetylene black is an effective additive for ORR electrocatalyst.

Keywords: *ORR electrocatalyst; additive; functionalized acetylene black; Platinum reduction*

1. Introduction

Electrochemical methods of energy handling are major contributors for energy sources that can circumvent the environmental problems. Fuel cells, a type of electrochemical device, are potential alternative to existing fuel – consuming systems. The high expense involved has led to efforts to reduce costs and increase efficiency. In the case of PEM fuel cells, improving the kinetics of the reduction reaction at the cathode, which is slower compared to the oxidation at the anode, is crucial to increase the efficiency. Platinum (Pt) or platinum alloy with carbon support are the most common ORR electrocatalysts. However, platinum being an indispensable but expensive and rare element, it is important to reduce it while maintaining efficiency. Further, the formulation of such a catalyst should be facile for large-scale production to reduce costs effectively [1–6].

Several investigations on catalyst supports have proven that Pt-Pt-catalysts with acetylene black (AB) exhibit better performance [5,7]. Pretreatment of carbon enhances the catalytic activity towards ORR by increasing surface functional groups and porosity, thereby contributing to higher surface area and increasing the adsorption sites [8]. Acetylene Black, owing to its high ORR activity on its own due to excellent absorption properties, negligible charge transfer resistance has been considered a primary candidate [9]. Studies on 30 wt% Pt decorated on functionalized acetylene black, 30% Pt/FAB report improved performance in terms of mass activity (MA) and electrochemically active surface area (ECSA), where the acetylene black was chemically pretreated [10,11].

This study explores the use of functionalized acetylene black as an additive to a commercial catalyst. In contrast to the substitution of platinum using other metals via reduction reaction processes to reduce the Pt content [12,13], the functionalized material is added by mechanical mixing. The functionalization increases the binding between the catalyst particles, enhancing the diffusion of oxygen onto the catalyst owing to the oxygen moieties present, thereby improving the kinetics of ORR without loss in mass activity [8]. The functionalized AB was added in different weight ratios to the commercial catalyst 20 % Pt/C (Vulcan XC-72) and the ORR activity of the Pt/C – FAB mixtures was examined using cyclic voltammetry, linear sweep voltammetry and accelerated degradation test.

2. Materials and methods

Commercially procured acetylene black (AB) from Alfa Aesar, and 20% Pt/C (Vulcan XC-72) from Sigma Aldrich were used.

2.1. Pretreatment of acetylene black

Pretreatment of acetylene black was done by mineral acid functionalization. The commercially procured acetylene black was dispersed in a concentrated acid mixture of sulphuric acid and nitric acid (3: 1 ratio of H_2SO_4 and HNO_3), and ultrasonicated for 3 hours. The resulting functionalized and exfoliated AB was then diluted with deionized water and recovered by vacuum filtration. The filtrate was subsequently washed thoroughly with deionized water until the pH was neutralized to remove any acid contaminants. This was then dried at 80 °C overnight in a vacuum oven to obtain functionalized acetylene black [10].

2.2. Characterization

The surface morphology of the AB and FAB was characterized using field – emission scanning electron microscopy (FESEM, Carl ZEISS in SE – Inlens Duo mode) and transmission electron microscopy (JEOL). The thermal stability of the commercial catalyst due to the addition of FAB was studied in air atmosphere at a heating rate of 10 °C per minute using thermogravimetric analysis (Netzsch STA 449 F1). X-ray diffractograms were recorded in the 2θ range of 10°–90° with a step size of 0.01 at 0.3 sec per step speed in Rigaku SmartLab X-ray powder diffractometer with copper radiation (Cu Kα: $\lambda = 1.542$ Å).

To evaluate the electrochemical performance, cyclic voltammetry (CV), linear sweep voltammetry (LSV) and accelerated degradation test (ADT) were conducted. The FAB added catalyst ink was prepared by mixing DI water, isopropyl alcohol and 5 Wt% Nafion (in the ratio – 3:2:0.44) to 1 mg of the catalyst and ultrasonicated for 15 minutes to prevent agglomeration. This catalyst was coated onto a glassy carbon electrode (GCE) of area 0.0707 cm^2 and dried at room temperature.

For electrochemical measurements, 0.1 M of perchloric acid was used as the electrolyte solution. CV and ADT were performed at room temperature using Solartron 1470 Cell system. The working electrode was GCE coated with the catalyst ink, with platinum and silver-silver chloride (Ag/AgCl) as counter and reference electrodes, respectively. CV measurements were scanned in the potential range of -0.2 V and 1 V (vs. Ag/AgCl) at 50 mV s^{-1}. The linear sweep voltammetry was conducted using CH instrument (PINE Research Instrumentation) between 0.2 V and 1 V (vs. Ag/AgCl). The working electrode, GCE coated with the catalyst ink, was rotated at different rpm (rotations per minute) ranging from 200 rpm to 1600 rpm to study mass transport effects. The ADT was performed by pulsing square wave potential between 0.6 V and 1.2 V vs. Ag/AgCl with a hold time of 10s and 50s at a scan rate of 10 mV s^{-1} for 18 cycles [14,15]. CV was performed before and after ADT at a slower scan rate of 10 mV s^{-1} to quantify the degradation of the catalytic support against corrosion.

3. Results

3.1. Morphological, structural and thermal characterization

The FESEM micrographs of acetylene black (AB), functionalized acetylene black (FAB), and the TEM micrograph of FAB are presented for comparison in figure 1 (a), (b) and (c). Figure 1(b) clearly exhibited a deep functionalization, as evinced by the formation of a disintegrated and spongy surface against the once rigid grain structure, as seen in acetylene black in 1(a). This can be attributed to the oxidation and functionalities introduced through the mineral acid functionalization. Though the intensity of functionalization could not be determined, the acid treatment had resulted in a well networked matrix. The TEM micrograph in figure 1(c) further confirmed the disintegrated and well-dispersed nature due to functionalization [10].

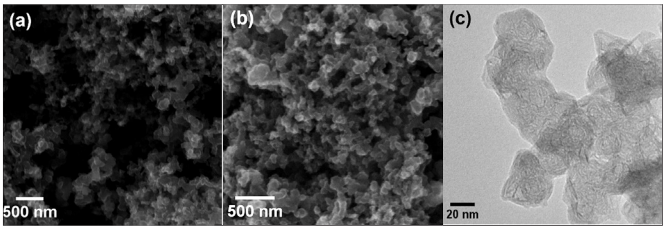

Figure 1. FESEM images of (a) acetylene black (AB), (b) functionalized acetylene black (FAB), and (c) TEM micrograph of FAB

Thermogravimetric analysis was conducted for the catalysts containing FAB in 20% Pt/C - 1wt%, 10wt%, 15wt% respectively. The actual weight content of platinum decreased to 19.8 %, 18 %, and 17 % as the weight percentage of FAB increased. Figure 2(a) revealed that carbon started decomposing above 400 °C and was oxidised completely by 650 °C leaving behind only platinum metal. The calculated weights closely matched the actual values, with an error of 10% from the instrument. The X-Ray diffractogram in figure 2(b) confirmed the presence of graphitic (002) planes at 25.46°of AB and FAB [16]. A slight increase in full width half maximum (FWHM) was observed for the (002) peak of FAB indicating functionalization.

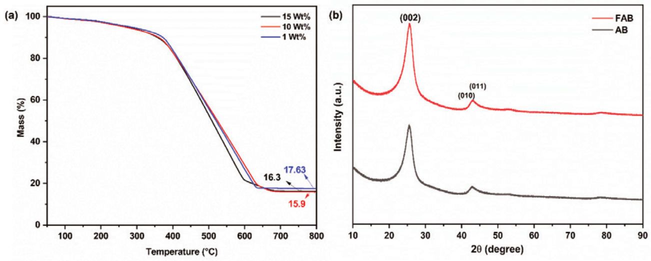

Figure 2. (a) Thermograms for 1, 10, and 15 Wt% of FAB in Pt/C in air atmosphere; (b) - X Ray diffractograms of AB and FAB

3.2. Electrochemical characterization

3.2.1. Cyclic voltammetry studies

Cyclic voltammetry studies for an ORR electrocatalyst has key features like a hydrogen desorption peak in the anodic sweep, from -0.2 V to 0 V vs Ag/AgCl, and a hydrogen evolution region around 1 V. In the reverse sweep, a peak around 0.9 to 0.5 V indicate the ORR region, while the peak region near 0 V to -0.196 V correspond to the hydrogen adsorption region. Several parameters, including onset potential, peak potential for ORR, current density at the ORR peak potential, mass activity at the ORR peak, electrochemically active surface area (ECSA) could be estimated from the CV plot from the figure 3 are tabulated below in Table 1 [14].

The onset potential, signifying the ease of oxygen reduction, initially decreased with FAB addition, reaching a minimum at 5 Wt%. However, further FAB loading resulted in a progressive increase in onset potential, exceeding the commercial catalyst. The ORR peak potential dipped with addition of FAB, but with increase in the addition, a gradual increase was observed reaching a maximum at 15 Wt% with a value of 0.472 V compared to 0.464 V of Pt/C, but only to decrease drastically at 20 Wt% inclusion of FAB.

In case of peak current density, that reflects the maximum achievable ORR activity, highest value was recorded with 15 Wt% FAB addition, exceeding the commercial catalyst by nearly 3%. But further FAB addition resulted in a decrease in current density.

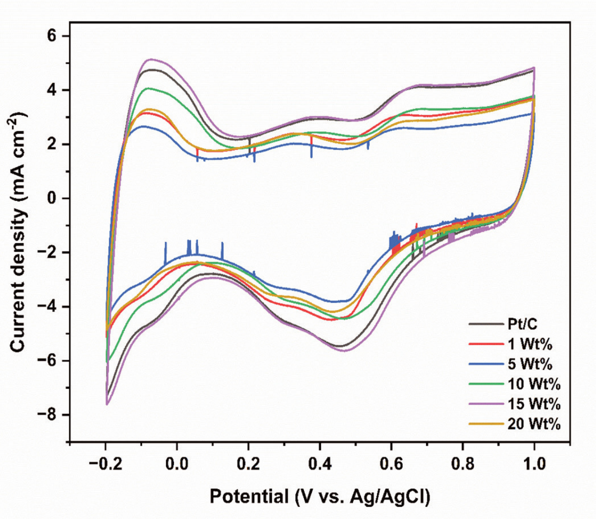

Figure 3. Cyclic Voltammogram for 20% Pt/C and 1, 5, 10, 15, 20 wt % FAB in Pt/C in 0.1 M Perchloric acid, Scan Rate = 50 mV/s

Mass activity, relating current density to catalyst mass, and ECSA, representing the electrochemically active surface area, followed a trend like the ORR peak potential and the peak current density. The mass activity and ECSA for the 1 wt % addition of FAB were less than that of the commercial catalyst and decreased further for 5 wt %. But, as the percentage of FAB addition increased, the mass activity increased, indicating FAB's addition acted as a matrix for dispersion. This was due to the electrochemically active surface area being greater, contributing to enhanced activity. The 15 wt % had the maximum value of MA with a large ECSA value of 32 m^2 g^{-1}, exceeding the commercial catalyst's value of 25.3 m^2 g^{-1}, while further increase in FAB to the catalyst caused a fall in ECSA and the mass activity.

Table 1- Electrochemical parameters of the electrocatalysts calculated from CV in figure 3.

Catalyst (FAB in wt%)	Onset Potential for ORR (V) vs. Ag/AgCl	ORR Peak Potential (V) vs. Ag/AgCl	Current Density at ORR Peak (mA cm^{-2})	Mass Activity (mA mg^{-1})	ECSA (m^2 g^{-1})
Pt/C	0.737	0.464	5.45	18.18	25.242
1 wt%	0.702	0.433	4.48	15.68	17.327
5 wt%	0.696	0.444	3.82	13.92	15.622
10 wt%	0.763	0.466	4.45	17.92	25.141
15 wt%	0.785	0.472	5.63	22.82	32.066
20 wt%	0.741	0.439	4.18	17.92	19.808

3.2.2. Linear sweep voltammetry studies

Linear sweep voltammetry was performed for the best performing catalyst, 15 wt% FAB and Pt/C, in rotating disk electrode setup. It was observed that with an increase in rotation speed of the electrode, the current increased as expected for the electrodes in diffusion-controlled environment; however, the onset was maintained at the same potential. Comparing the limiting current densities obtained through LS voltammograms in figure 4 of the two catalysts, 15 wt% FAB in Pt/C had better current density as compared to the 20% Pt/C. Interestingly, both catalysts exhibited a similar onset potential of 0.6 V vs Ag/AgCl, but the peak potentials for the ORR were shifted for 15 Wt% FAB added Pt/C.

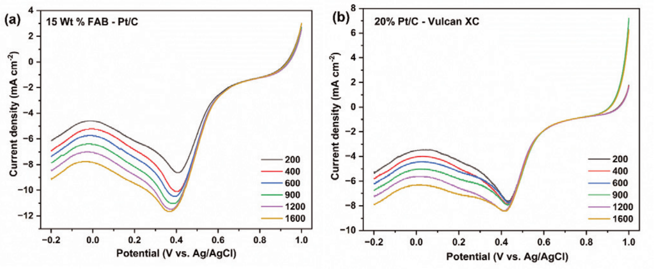

Figure 4. LSV for (a) 15 wt% FAB-Pt/C and (b) 20% Pt/C – Vulcan XC in 0.1 M Perchloric acid, Scan Rate = 50 mV/s for different rpm

3.2.3. Accelerated degradation test

The Accelerated degradation test was conducted to confirm the stability of FAB as catalytic support against corrosion. Cyclic voltametric studies before and after the pulsing of potential were performed to quantify the degradation by calculating the ECSA under the hydrogen desorption peak. It was found that even after the ADT, there was not a major difference in the CV, indicating a stable catalytic support. While 1 wt%, 5 wt%, and 15 wt% - FAB in Pt/C show an increased marginal difference in the active area under the hydrogen desorption peak after the pulsing of potential, 10 wt% and 20 wt % FAB-Pt/C exhibited more degradation.

4. Discussion

4.1. Thermogravimetric analysis

The TGA analysis was conducted to investigate the weight percentage of Platinum in FAB – Vulcan XC-72 and to confirm that there was no detrimental effect in the thermal stability of the catalyst due to the addition of functionalized acetylene black. In figure 2 (a), the carbon forms decompose at a temperature above 400 °C and oxidize completely by 650°C owing to the evaporation of the adsorbed water, the decomposition of oxygen-containing functional groups, and the combustion of carbon skeleton. Thus, at higher temperatures, only platinum was found to be the residual content.

4.2. Electrochemical Analysis - Rationale for efficiency from CV studies

Cyclic voltammetry studies have revealed the following as the order of efficiency for the catalysts

15 wt % > 10 wt % > 20 wt % > 1 wt % > 5 wt %

The rationale behind the above order is hypothesized as; the 1 wt% to 5 Wt% addition of FAB to 20% Pt/C disrupts the existing pristine network of Pt/C, leading to an obstruction in the conductivity and hence decreased current density. Additionally, FAB not being completely dispersed in the matrix does not allow proper transfer of charges, leading to a disturbance in the distribution of charges. With further increase in FAB, a small increase in the electrochemical properties of the catalysts is observed, which could be due to the uniform dispersion of FAB and its inherent properties like absorptivity and conductivity contributing to the matrix in unison. The 15 wt% FAB-Pt/C exhibits the best performance due to optimal FAB dispersion leading to higher ECSA that indicates available sites for catalysis, MA and higher current density. However, when the amount of FAB is increases from 15 wt% to 20 wt%, a detrimental effect is observed, which might be due to the crowding of the functionalized acetylene black around the active sites, potentially blocking the access. These results suggest that an optimal amount of FAB addition can maximise the ORR activity. Figure 5 represents a schematic representation of this hypothesis.

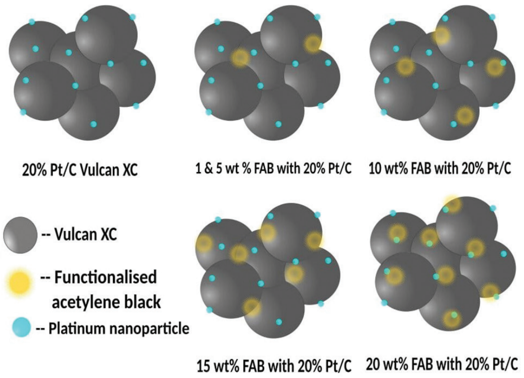

Figure 5. Schematic representing dispersion of FAB in 20% Pt/C Vulcan XC

4.3. Confirmation through Linear Sweep Voltammetry

Linear sweep voltammetry studies confirm the observations from CV studies. 15 wt% FAB-Pt/C exhibits higher limiting current density, indicating an improved ORR activity compared to the commercial 20% Pt/C. Despite the shift in their ORR peak potentials, possibly due to a larger reduction of oxygen species at the electrode, the onset potentials remain similar at 0.6 V vs. Ag/AgCl for both the catalysts. The peak potential shift observed only in the 15 wt% FAB-Pt/C might be due to a stronger interaction between FAB and oxygenated species, leading to more efficient reduction, enhancing the current density and hence mass activity. The mass activity calculated for the 15 wt% FAB in Pt/C (22.82 mA g^{-1}) demonstrates an 18 % increase compared to the unmodified commercial catalyst (18.18 mA g^{-1}), deeming the 15 wt% FAB added commercial catalyst to be a better one. This result aligns with the findings from the cyclic voltammetry test.

4.4. Stability assessment through accelerated degradation test

Corrosion testing, performed using the accelerated degradation test, reveals good stability for most samples. Electrocatalysts with 1 wt %, 5 wt %, and 15 wt % - FAB additions exhibit a slight increase in the ECSA after the ADT, which can be attributed to the activation of (111) plane of Pt within the catalyst. The ECSA difference is negligible in 10 wt% FAB-Pt/C, while 20 Wt% FAB-Pt/C shows a larger reduction in ECSA following the ADT, suggesting degradation due to the amorphous nature in FAB. These observations suggest that there might be an optimal FAB loading that balances improved activity with acceptable durability.

5. Conclusion

The optimized electrocatalyst containing 15 wt% addition of FAB in the commercial 20% Pt/C catalyst exhibits superior performance in terms of mass activity and higher onset potential. This composite not only demonstrates higher catalytic activity, but also maintains stability under pulsating potentials. Long duration stability studies constitute the future scope of this work. In conclusion, these experimental findings confirm that incorporating an optimal amount of functionalized acetylene black does not hinder the ORR activity but rather enhances the ORR kinetics even at lower platinum content, offering a promising strategy for developing Pt-based electrocatalysts.

Acknowledgements: The authors would like to thank the Department of Science and Technology, Government of India for the financial support provided for the project.

References:

[1] J. Zhang, Recent advances in cathode electrocatalysts for PEM fuel cells, Front. Energy 5 (2011) 137–148. https://doi.org/10.1007/s11708-011-0153-y.

[2] W.J. Khudhayer, N.N. Kariuki, X. Wang, D.J. Myers, A.U. Shaikh, T. Karabacak, Oxygen Reduction Reaction Electrocatalytic Activity of Glancing Angle Deposited Platinum Nanorod Arrays, J. Electrochem. Soc. 158 (2011) B1029. https://doi.org/10.1149/1.3599901.

[3] M. Zhang, L. Dai, Carbon nanomaterials as metal-free catalysts in next generation fuel cells, Nano Energy 1 (2012) 514–517. https://doi.org/10.1016/j.nanoen.2012.02.008.

[4] M. Chiwata, K. Kakinuma, M. Wakisaka, M. Uchida, S. Deki, M. Watanabe, H. Uchida, Oxygen reduction reaction activity and durability of Pt catalysts supported on titanium carbide, Catalysts 5 (2015) 966–980. https://doi.org/10.3390/catal5020966.

[5] A.E. Russell, Steady state oxygen reduction and cyclic voltammetry, Faraday Discuss. 140 (2008) 9–10. https://doi.org/10.1039/b814058h.

[6] Y. Wang, K.S. Chen, J. Mishler, S.C. Cho, X.C. Adroher, A review of polymer electrolyte membrane fuel cells: Technology, applications, and needs on fundamental research, Appl. Energy 88 (2011) 981–1007. https://doi.org/10.1016/j.apenergy.2010.09.030.

[7] M.J. Lázaro, L. Calvillo, V. Celorrio, J.I. Pardo, S. Perathoner, R. Moliner, Study and application of carbon black vulcan XC-72R in polymeric electrolyte fuel cells, Carbon Black Prod. Prop. Uses (2011) 41–68.

[8] M. Uchida, Y. Fukuoka, Y. Sugawara, H. Ohara, A. Ohta, Improved Preparation Process of Very-Low-Platinum-Loading Electrodes for Polymer Electrolyte Fuel Cells, J. Electrochem. Soc. 145 (1998) 3708–3713. https://doi.org/10.1149/1.1838863.

[9] Q. Xiang, S. Li, X. Zou, Y. Qiang, B. Hu, Y. Cen, C. Xu, L. Liu, Y. Zhou, C. Chen, Self-assembly porous metal-free electrocatalysts templated from sulfur for efficient oxygen reduction reaction, Appl. Surf. Sci. 462 (2018) 65–72. https://doi.org/10.1016/j.apsusc.2018.08.022.

[10] R. Badam, R. Vedarajan, N. Matsumi, Platinum decorated functionalized defective acetylene black; A promising cathode material for the oxygen reduction reaction, Chem. Commun. 51 (2015) 9841–9844. https://doi.org/10.1039/c5cc02235e.

[11] S. Bukka, R. Badam, R. Vedarajan, N. Matsumi, Photo-generation of ultra-small Pt nanoparticles on carbon-titanium dioxide nanotube composites: A novel strategy for efficient ORR activity with low Pt content, Int. J. Hydrogen Energy 44 (2019) 4745–4753. https://doi.org/10.1016/j.ijhydene.2019.01.004.

[12] U.A. Paulus, A. Wokaun, G.G. Scherer, T.J. Schmidt, V. Stamenkovic, V. Radmilovic, N.M. Markovic, P.N. Ross, Oxygen reduction on carbon-supported Pt-Ni and Pt-Co alloy catalysts, J. Phys. Chem. B 106 (2002) 4181–4191. https://doi.org/10.1021/jp013442l.

[13] T. Toda, H. Igarashi, H. Uchida, M. Watanabe, Enhancement of the Electroreduction of Oxygen on Pt Alloys with Fe, Ni, and Co, J. Electrochem. Soc. 146 (1999) 3750–3756. https://doi.org/10.1149/1.1392544.

[14] J.A. Prithi, R. Vedarajan, G. Ranga Rao, N. Rajalakshmi, Functionalization of carbons for Pt electrocatalyst in PEMFC, Int. J. Hydrogen Energy 46 (2021) 17871–17885. https://doi.org/10.1016/j.ijhydene.2021.02.186.

[15] F. Forouzandeh, X. Li, D.W. Banham, F. Feng, S. Ye, V. Birss, Evaluation of the Corrosion Resistance of Carbons for Use as PEM Fuel Cell Cathode Supports, J. Electrochem. Soc. 162 (2015) F1333–F1341. https://doi.org/10.1149/2.0381512jes.

[16] T. Ungár, J. Gubicza, G. Ribárik, C. Pantea, T.W. Zerda, Microstructure of carbon blacks determined by X-ray diffraction profile analysis, Carbon N. Y. 40 (2002) 929–937. https://doi.org/10.1016/S0008-6223(01)00224-X.

Solid-State Zinc Ion Hybrid Capacitor Using MWCNTs Cathode

*Antima Pandey, Shanu Mishra, Ashish Kumar Mishra**

School of Materials Science and Technology,

Indian Institute of Technology (Banaras Hindu University), Varanasi, India.

Email: akmishra.mst@iitbhu.ac.in

Abstract

In this study, multiwalled carbon nanotubes (MWCNTs) were synthesized using iron nanoparticles as catalyst, derived from green tea. We demonstrated a zinc ion hybrid capacitor cell utilizing MWCNTs as a cathode. The cell achieved a specific capacitance of 221 F g^{-1} at a current density of 1 A g^{-1}, showcasing superior rate capability with 93.7 F g^{-1} at 5 A g^{-1}. Additionally, it exhibited a high energy density of 78.9 W h kg^{-1} and a power density of 800 W kg^{-1} at 1 A g^{-1}. After 8000 charge-discharge cycles, tested at 5 A g^{-1}, the cell retained 89% of its capacitance retention with nearly 100% coulombic efficiency.

Keywords: *Zinc ion hybrid capacitor; Polyvinyl alcohol; Zinc sulphate; Multiwalled carbon nanotube, Specific capacitance.*

1. Introduction

Electrochemical energy storage devices (EES) have garnered significant attention in achieving economic and low-carbon societies due to their high energy/power densities, ease of design, and environmental sustainability [1,2]. These devices encompass various types such as metal-ion batteries (e.g., Li, Na, K, Zn), supercapacitors, and hybrid capacitors [3,4]. Hybrid capacitors, which combine a battery-type electrode and a capacitor-type electrode, offer high energy and power densities along with extended cycle life [5]. Among hybrid capacitors, zinc-ion hybrid capacitors (ZIHCs) are particularly noteworthy [6]. They utilize a battery-type zinc metal anode and a capacitor-type carbon cathode to achieve their performance characteristics. Compared to Li/Na-ion hybrid capacitors, ZIHCs are advantageous due to their lower cost and enhanced safety profiles [7]. ZHCs typically consist of Zinc (Zn) metal anodes, which offer a high theoretical specific capacity of 823 m Ah g^{-1} and operate at a low redox potential (-0.76 V versus standard hydrogen electrode) [8]. The carbon cathode serves as the capacitor-type electrode. Aqueous or polymer-based solid electrolytes containing Zn^{2+} ions, facilitate efficient energy storage [9]. The combination of these components enables ZIHCs to store energy effectively, maintain a wide voltage window, and demonstrate robust performance in various applications. Since, Carbon cathodes are characterized by their high specific surface area, extensive porous structure, and excellent electrical conductivity, which facilitate rapid adsorption and desorption of zinc-containing ions [10]. These properties contribute significantly to achieve high power densities in ZIHCs. However, carbon cathode materials still confront challenges related to their reversible charge storage capacity [11]. This issue predominantly stems from factors such as the energy storage mechanism along with the physical and chemical properties of carbon materials [12]. These factors include mismatched pore sizes with zinc ions, low density, and underutilization of active sites. Therefore, the pivotal strategy to enhance the zinc ion storage capabilities of ZIHCs lies in the design and advancement of novel porous carbon cathode materials [13]. This approach aims to optimize the microstructure and surface properties of carbon materials, thereby maximizing their efficiency in storing and releasing zinc ions during electrochemical processes [14]. Various precursors have been utilized to manufacture high-specific surface area activated carbon as cathode materials for ZIHCs, including biomass such as sugarcane stems, glutinous rice, and bamboo shavings [15–17].

Polymers like polyaniline-co-polypyrrole-derived hollow carbon spheres and polyacrylonitrile-derived carbon have also been employed [18–23]. Solid electrolytes are typically non-flammable and less prone to leakage compared to liquid electrolytes, enhancing the safety of devices such as batteries, they can operate at higher voltages without decomposition or side reactions, which improves the stability and lifespan of the device. Solid electrolytes enable higher energy density designs due to their ability to pack more active materials in a given volume or weight compared to liquid electrolytes. They can function effectively over a wider range of temperatures compared to liquid electrolytes, making them suitable for diverse environmental conditions. Certain solid electrolytes exhibit resistance to dendrite formation, a common issue in batteries that can cause short circuits and reduce lifespan. They can contribute to environmentally friendly devices by reducing the use of flammable and toxic materials typically found in liquid electrolytes. Solid electrolytes are promising for advancing the performance, safety, and environmental impact of energy storage devices such as batteries and capacitors [24–29]. Additionally, some literature described polymer electrolyte-based ZIHCs utilizing carbon materials as a cathode. Wei *et al*. [30] used carbon fiber as a cathode and showed a specific capacity of 47.6 m A h g^{-1} at 0.2 A g^{-1}, maintaining 78% capacitance retention over 5000 cycles. Wang *et al*. [31] demonstrated ZIHCs using bio-carbon-derived porous material as the cathode, showing a good discharge capacitance of 170 F g^{-1} at 0.1 A g^{-1} with high energy density (52.7 W h kg^{-1} at 1725 W kg^{-1} power density). Chen *et al*. [32] synthesized co-polymer-derived hollow carbon spheres as cathode and demonstrated that the flexible solid-state ZIHC shows maximum capacity of 86.8 m A h g^{-1} and an energy density of 59.7 W h kg^{-1} with a power density of 447.8 W kg^{-1}.

There have been few studies on green approach for the synthesis of carbon nanotubes (CNTs). Tripathi *et al*. presented a novel approach and demonstration the growth of bulk carbon nanotubes (CNTs) using green catalysts. The CNTs were synthesized using catalysts derived from plant extracts, specifically garden grass (Cynodon dactylon), rose (Rosa), neem (Azadirachta indica), and walnut (Juglans regia) [33]. Chufa *et al*. highlighted recent advancements in carbon nanotube (CNT) synthesis, with particular emphasis on green synthesis methods [34]. In this study the authors used green tea to synthesize stable iron nanoparticles and employed iron nanoparticles as catalysts to prepare MWCNTs via CVD method through pyrolysis of acetylene. Here, we introduced a safe solid-state zinc ion hybrid supercapacitor (ZIHC) with MWCNTs as cathode, polyvinyl alcohol/zinc sulphate (PVA + $ZnSO_4$) membrane as electrolyte, and zinc sheet as anode. The ion adsorption and desorption kinetics of the cathode is improved due to the high surface area of the MWCNTs and their nanotube structure. The designed solid-state ZIHC shows good specific capacitance and energy density with a high-power density along with a high degree of capacitance retention.

2 Experimental

2.1 Materials

Ferrous sulfate heptahydrate ($FeSO_4 \cdot 7H_2O$) and nitric acid (HNO_3) were purchased from Loba Chemie Pvt. Ltd., India, while the lepton green tea leaves were obtained from a local commercial vendor. The chemical reagents were of analytical grade and were employed without additional purification.

2.2 Synthesis of Multiwalled Carbon Nano Tubes (MWCNTs)

Synthesis of iron nanoparticles using green tea (Lipton green tea) extract and MWCNTs are done as described in our earlier report [35]. Lipton Green Tea consists of Camellia Sinensis leaves that have undergone minimal oxidation during processing to preserve the natural polyphenols and antioxidants present in the leaves. Green tea helps to stabilize the iron nanoparticles which act as catalyst for the growth of CNTs. The stable iron nanoparticles provide greater yield of CNTs using C_2H_2 as precursor. The conventionally synthesized iron nanoparticles get easily oxidized, which reduces their catalytic activity and hence decreases the yield of CNTs. Specifically, 2.5 g of ferrous sulphate was added to 40 mL of prepared green tea extract, and the mixture was continuously stirred for 24 hours. During this period, the green tea extract served as a reducing agent and reduces ferrous sulphate into zero-valent iron nanoparticles. The resulting solution was then centrifuged and subsequently dried. An advantageous aspect of green tea-synthesized iron nanoparticles lies in dual role of green tea extract acting as a dispersant and capping agent. This property prevents nanoparticle agglomeration and enhances their stability, thereby prolonging their reactivity.

The prepared iron nanoparticles as catalyst were placed in quartz boat and positioned in a chemical vapor deposition (CVD) setup. The quartz boat underwent heating to 700 °C at a rate of 5 °C/min under an inert Ar-H_2 atmosphere with flow rate of 100 sccm. Subsequently, acetylene, a carbon source gas, was introduced into the quartz tube at 700 °C with a flow rate of 100 sccm for 30 minutes to facilitate the growth of multi-walled carbon nanotubes (MWCNTs). After the growth period of 30 minutes, the furnace was cooled to room temperature. The as-synthesized nanotubes underwent further treatment by heating at 400 °C for 120 minutes in open air to remove any amorphous carbon impurities. This step was followed by an acid purification process: the carbonized sample was mixed with 40 mL of concentrated nitric acid and stirred on a magnetic stirrer at 80 rpm for 24 hours. The resulting product was washed with deionized water until neutral and collected via centrifugation. Finally, the nanotubes obtained were dried in a vacuum oven at 60 °C.

2.3 Characterization

The synthesized MWCNTs was analyzed using various characterization techniques. X-ray diffraction (XRD) pattern was obtained in the 2θ range of 10–65° using a Rigaku Miniflex-600 with Cu Kα radiation (λ=0.154 nm), employing a step size of 0.02°. Surface morphology was examined using a scanning electron microscope (Nova Nano SEM 450) operating at 20 kV, while high-resolution transmission electron microscopy (TEM Tecnai G20 TWIN) was used for detailed structural analysis. The Raman spectrum of the MWCNTs sample was acquired using a STR-300 micro-Raman spectrometer, with a laser excitation wavelength of 532 nm and a step size of 1.2 cm^{-1} with 1200 grating. FTIR study was done using a ThermoFisher Nicolet summit spectrometer using KBr pellets with a 4 cm^{-1} resolution.

2.4 Preparation of electrodes for electrochemical measurements

A uniform slurry solution of MWCNTs electrocatalyst was prepared by ultrasonically dispersing 10 mg of MWCNTs in 80 μL isopropyl alcohol, supplemented with 5 μL of Nafion as a binder. Conducting carbon paper (procured from Sainergy Fuel Cell India Pvt. Ltd., Chennai, India) sized at 1 cm × 1 cm was coated with the prepared slurry using a brush coating technique. Subsequently, the electrodes were dried overnight in a vacuum oven at 120 °C to minimize the effects of the binder.

For electrochemical measurements, a three-electrode setup was employed with Ag/AgCl (saturated with KCl) and Pt wire serving as reference and counter electrodes, respectively. The working electrode consisted of MWCNTs coated conducting carbon paper with a mass loading of 2 mg. Electrochemical characterization involved cyclic voltammetry (CV) at different scan rates within a voltage range of 0.0 to 0.9 V. All measurements were conducted in a 2 M $ZnSO_4$ aqueous electrolyte using a Corr Test electrochemical workstation instrument. A solid-state zinc ion hybrid capacitor device was tested within a potential range of 0.2 to 1.8 V. Electrochemical impedance spectroscopy (EIS) studies of MWCNTs were performed across frequencies ranging from 0.01 to 10^5 Hz, using a voltage amplitude of 5 mV.

2.5 Preparation of solid electrolyte and solid zinc ion hybrid capacitor cell

To prepare the PVA-$ZnSO_4$ gel membrane, 2 g of PVA was dissolved in 20 mL of deionized water at 90°C with vigorous stirring until the solution turned transparent. Once completely dissolved, 2M $ZnSO_4$ solution was prepared in 5 mL of deionized water was mixed into the PVA solution. The mixture was allowed to cool to room temperature, then poured into the patterned disc and subjected to freeze-drying at - 15°C for 12h to get final membrane.

ZIHC system was assembled using MWCNT-coated carbon paper as cathode and Zinc sheet as anode having dimensions of 2×2 cm^2. A PVA-$ZnSO_4$ solid membrane was placed between the two electrodes, which acts as a separator and electrolyte. The cathode was mounted on one side using a stainless-steel sheet as a current collector.

3 Results and discussion

3.1 Morphology, structural and spectroscopic studies

The scanning electron microscopy (SEM) analysis of purified MWCNTs, depicted in Fig. 1(a), reveals a uniform distribution of numerous curled and loosely entangled nanotubes. The image also verifies the purity of the MWCNTs by showing no presence of amorphous carbon or residual metal catalyst particles. The observed shorter lengths of the nanotubes are attributed to the rigorous acid treatment, which likely also contributed to the opening of hemispherical caps at the ends of the MWCNTs. Additionally, the structural morphology was investigated using transmission electron microscopy (TEM) as shown in Fig. 1(b). This examination confirmed the presence of MWCNTs with varied outer diameters ranging from 60 to 80 nm. The TEM image also revealed entangled and curled nanotubes, along with sidewall defects induced by the strong acid treatment. The crystallinity of purified MWCNTs was assessed through X-ray diffraction (XRD) analysis. The XRD pattern of MWCNTs closely resemble those of graphite due to their intrinsic nature [36]. The XRD pattern of MWCNTs (Fig. 1 c) exhibits characteristic peaks at 25.9° and 42.5°, corresponding to the (002) and (100) diffraction planes, respectively. The sharper peak around 25.9° is attributed to graphitic carbon. Compared to the standard graphite peak at $2\theta = 26.5°$, MWCNTs exhibit a slight shift towards a lower θ value, indicating an increased interlayer spacing of the sp^2 carbon layers [37]. The degree of crystallinity and defects in purified MWCNTs were analyzed using Raman spectroscopy. The Raman spectrum of MWCNTs exhibits two prominent bands: the D band (~1332 cm^{-1}) and the G band (~1602 cm^{-1}), as illustrated in Fig. 1 (d). The D band arises from the out-of-plane vibrations of sp^3-hybridized carbon atoms, indicating disordered graphitic planes and surface defects induced by the acid treatment during purification [38]. On the other hand, the G band corresponds to the in-plane stretching vibration of sp^2 carbon atoms. The intensity ratio (I_D/I_G) of the D and G bands in the Raman spectrum of MWCNTs was approximately 0.89. This indicates that the MWCNTs possess noticeable defects and functional groups resulting from the acid treatment, which likely contribute to reducing charge transfer resistance during the electrochemical processes [39]. The FTIR spectrum, shown in Figure 2(e) for MWCNTs, indicates the presence of various functional groups such as hydroxyl, carboxylic, and carbonyl groups. The FTIR spectrum reveals several distinctive peaks: a prominent O-H stretching vibration at approximately 3437 cm^{-1}, indicating the presence of hydroxyl groups (-OH) in the MWCNTs. Another significant peak appears around 2920 cm^{-1}, corresponding to C-H stretching vibrations, suggesting the existence of carbon-hydrogen (C-H) bonds. Additionally, there is a distinct peak at approximately 1730 cm^{-1}, attributed to the C=O bond stretching vibration, indicating the presence of carbonyl groups (C=O) in MWCNTs. The sharper and stronger C=C peak at around 1650 cm^{-1} in MWCNTs suggests a longer-range order of the sp^2 network. which provides better electrochemical behavior for the MWCNTs.

3.2 Electrochemical study

To investigate the electrocatalytic behavior of the prepared materials, electrochemical active surface area (ECSA) analysis was conducted using the cyclic voltammetry (CV) technique [40]. CV scans were performed at different scan rates (20, 40, 60, 80, and 100 mV s^{-1}) for MWCNTs (Fig. 2 a), in the non-faradaic region between -0.25 and 0.25 V.

To determine the double-layer capacitance (C_{dl}), half of the average difference between the anodic and cathodic charging currents at 0 V was linearly plotted against the scan rates, as shown in Fig.3 (b). The slope of this plot provides the C_{dl} value [35]. The electrochemical-specific surface area was calculated from the following equation (1).

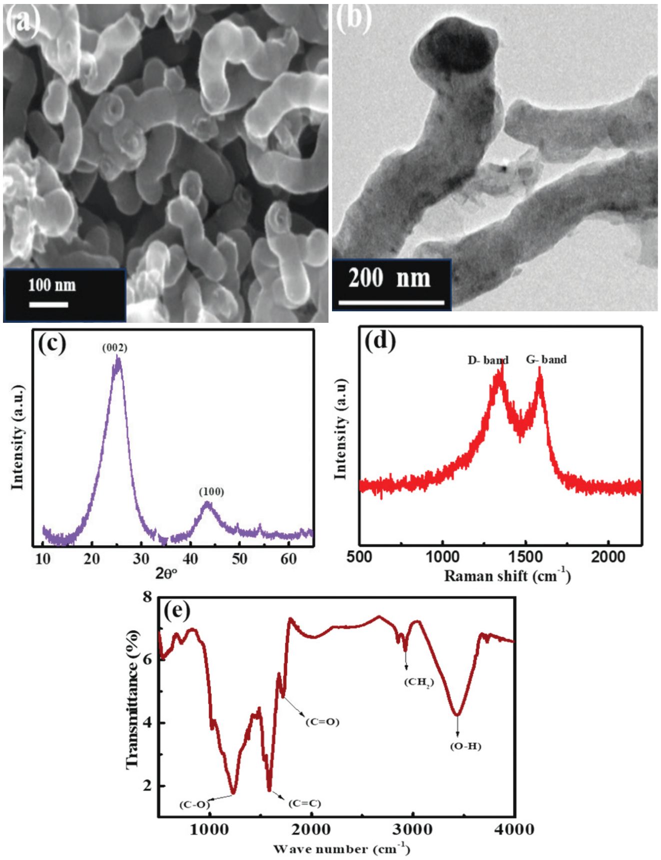

Fig.1 ***(a)*** *SEM image,* ***(b)*** *TEM image* ***(c)*** *XRD pattern,* ***(d)*** *RAMAN spectrum, and (e)FTIR spectrum of MWCNTs.*

$$\mathrm{ECSA} = \frac{C_{dl}}{C_s} \qquad (1)$$

Where C_{dl} represents the double-layer capacitance and C_S is the specific capacitance of the ideal flat surface of the catalyst. Various capacitance values for C_S within the range of 20-80 µF/cm² have been reported, with a commonly cited value being 40 µF/cm² [41]. The MWCNT material's C_{dl} value was investigated at 70.3 mF, and C_s was specified with a specific capacitance value of 40 µF. The estimated effective surface area (ECSA) of the MWCNT nanostructure is ~1757 cm². Given that the total mass of the MWCNT electrode is 2 mg, the available ECSA will be ~878 cm² mg^{-1}, which provides high charge storage in ZIHC.

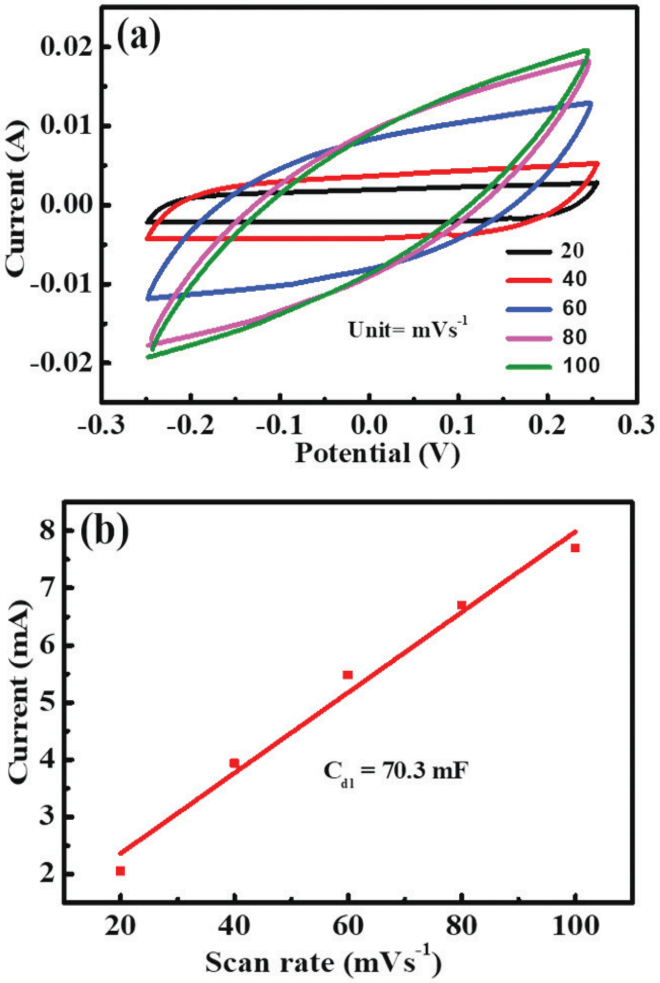

Fig.2 ***(a)*** *Electrochemical active surface Area (ECSA) test***,** ***(b)*** *Half of the difference of anodic and cathodic currents vs voltage scan rate for MWCNTs.*

Cyclic voltammetry (CV), galvanostatic charge-discharge (GCD), and electrochemical impedance spectroscopy (EIS) measurements were conducted using a three-electrode system to explore the capacitive properties of MWCNT-coated carbon paper electrodes. These tests were performed within a potential range of 0 to 0.9 V using a 2 M $ZnSO_4$ aqueous electrolyte. Figure 3 (a) illustrates the schematic representation of the 3-cell measurement setup. The setup includes an Ag/AgCl reference electrode, a Pt wire as the counter electrode, and the working electrode composed of the MWCNTs coated on carbon paper. Fig 3 (b) illustrates the CV curves obtained for the MWCNTs electrodes at various scan rates. The substantial area enclosed by the CV curves indicates the excellent capacitive behavior of the MWCNTs[42]. The specific capacitance of MWCNTs from CV study can be calculated using the following equation (2).

$$\text{Specific capacitance} = \frac{\int \text{Area inclosed in the CV curve}}{\text{m} \times \Delta\text{V} \times \text{S}} \qquad (2)$$

where m is the mass loading of MWCNTs on the electrode, ΔV is the potential window of the CV measurement, and S is the voltage scan rate. This formula allows for determining the specific capacitance based on the experimental data obtained from CV measurements. The maximum specific capacitance of ~151 F g^{-1} was observed for MWCNTs at 5 mV s^{-1}. The quasi-rectangular behavior in the CV curves for MWCNTs indicates the formation of an electrical double layer at the electrode-electrolyte interface. The maximum specific capacitance of 62.7 F g^{-1} was obtained at a high scan rate of 100 mV s^{-1}, suggesting a high degree of sustainability of capacitive performance, as shown in Fig. 3 (c). The capacitive characteristic can also be assessed through constant current charge-discharge cyclic testing, offering a more quantitative perspective on the capacitive performance of electrode material. Equation (3) was employed to calculate the specific capacitance (Cs) using the charge-discharge method.

$$\text{Specific capacitance} = \frac{I}{m} \text{ X } \frac{\Delta t}{\Delta V} \qquad (3)$$

where Δt represents the discharged time, ΔV is the potential window, and m denotes the mass of the electrode material. The quasi-triangular behavior of MWCNTs contributes to their reversible charge-discharge characteristics. Fig. 3 (d) illustrates the galvanostatic charge-discharge curves at current densities ranging from 0.5 to 5 A g^{-1}. A specific capacitance of 132 F g^{-1} was achieved at a discharge current density of 0.5 A g^{-1}. This higher capacitance value can be attributed to the accessible surface area created by the well-separated nanotube structure and functional groups, which enhance the wettability of the electrode for efficient electrolyte transport. Fig. 3 (e) shows the specific capacitances of 92.4, 77, 67, 64, and 55 F g^{-1} at 1, 2, 3, 4, and 5 A g^{-1} current densities, respectively. Fig. 3 (f) shows, the Nyquist plot for the MWCNTs electrode. The Nyquist plot of MWCNTs electrode exhibits a semicircle at higher frequencies and a straight line in the lower frequency region, confirming its capacitive behavior. The internal resistance (Rs) of approximately 1.9 Ω, a semicircle indicating charge transfer resistance (Rct) around 6.9 Ω, and a Warburg resistance attributed to diffusion processes are observed. At low frequencies, the Nyquist plot shows a nearly vertical line parallel to the imaginary axis, indicative of good capacitor behavior.

To evaluate practical performance, we investigated the capacitive properties of a solid-state ZIHC device utilizing MWCNTs nanostructure as cathode material and PVA-$ZnSO_4$ combinedly serving as the separator and solid electrolyte. Fig. 4 (a) displays an image of the designed ZIHC, while Fig. 4 (b) illustrates the CV curves at various scan rates.

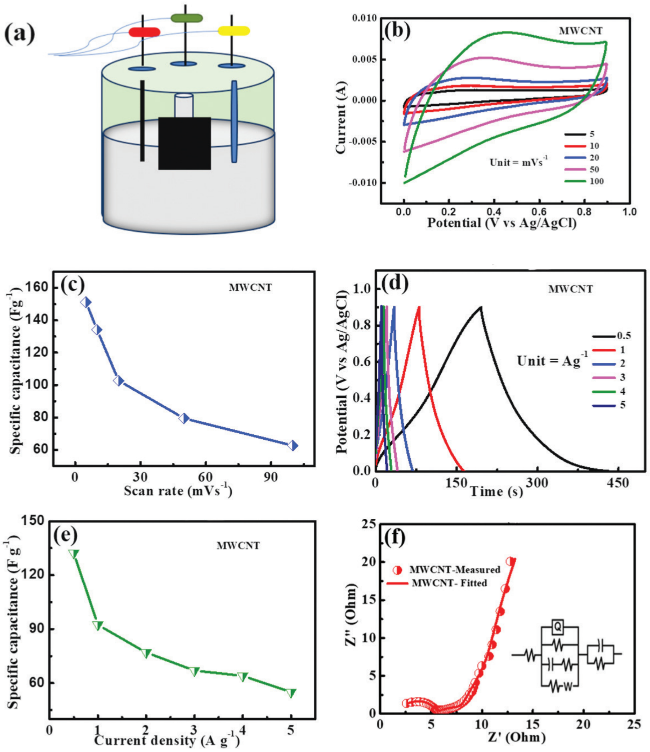

Fig.3(a) *Schematic diagram of 3 cell measurement,* ***(b)*** *CV curves* ***(c)*** *specific capacitance vs scan rate,* ***(d)*** *GCD curves,* ***(e)*** *specific capacitance vs current density, and* ***(f)*** *EIS plot for MWCNTs.*

The CV curves for the MWCNTs-based solid-state ZIHC indicate the formation of an electric double-layer at the electrode-electrolyte interface, consistent across hybrid cell measurements. A small redox peak indicates the pseudo behavior due to the ion adsorption/desorption across electrodes but EDLC behavior still dominates. For the cell configuration, a maximum specific capacitance of 271.4 F g^{-1} was achieved at a scan rate of 5 mV s^{-1}. Also, Fig.5 (c) shows the specific capacitance of 246, 213, 180.3, and 115 Fg^{-1} at different voltage scan rates of 10, 20, 50, and 100 mVs^{-1}, respectively, further confirming that the MWCNT is the high sustainable materials for the ZIHC device. The galvanostatic charge-discharge (GCD) curves are the quantitative measurement of the energy storage of the ZIHCs, exhibiting quasi-triangular behavior (Fig. 4 d) with a specific capacitance of 221 F g^{-1} at a discharge current density of 1 A g^{-1} for the ZIHC device. Fig 4 (e) shows the specific capacitances 191.7, 145, 128, and 93.7 F g^{-1} at 2, 3, 4 and 5 A g^{-1} current density respectively, showing the high-rate capability of ZIHC. Figure 4(f) illustrates the electrochemical impedance spectrum for the MWCNTs-based solid-state ZIHC device. For the ZIHC device, Rs ~3.25 Ω and Rct ~12.7 Ω are observed, facilitating efficient charge transfer across the electrode-electrolyte interface due to good conductivity and high ECSA of MWCNTs.

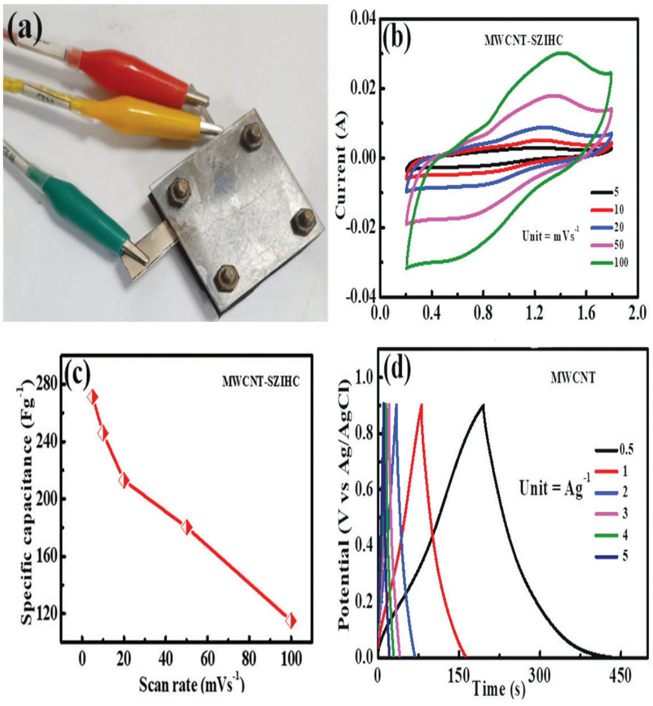

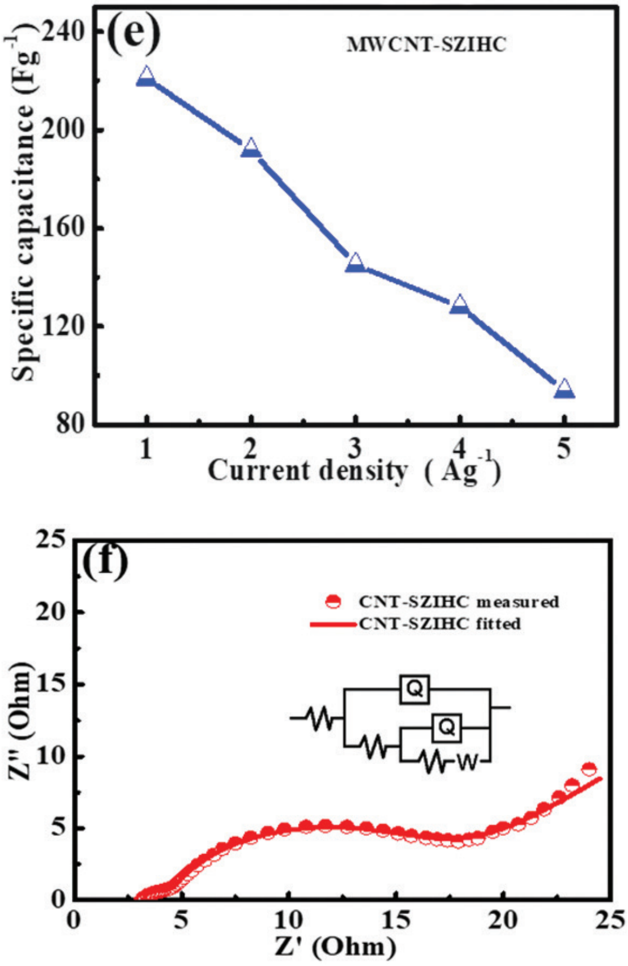

Fig.4 ***(a)*** *Photograph of ZIHC device*, ***(b)*** *CV curves*, ***(c)*** *specific capacitance vs scan rates* ***(d)*** *GCD curves,* ***(e)*** *specific capacitance at different current densities, and* ***(f)*** *EIS plot of MWCNT-based solid-state ZIHC device.*

We know that energy density determines how much energy ZIHC can store, while power density dictates how quickly they can charge and discharge, and cycle stability ensures their reliability over repeated use. These factors collectively define the effectiveness and practical utility of MWCNTs-based solid-state ZIHC in various high-performance applications. Fig. 5(a) depicts the Ragone plot of our device, highlighting its high energy density of 78.9 W h kg^{-1} at a power density of 800 W kg^{-1}. This performance is attributed to the efficient ion transfer between the electrolyte and electrode interfaces. The designed ZIHC device demonstrates high sustainable performance, achieving an excellent power density of 6400 W kg^{-1} alongside an energy density of 19 W h kg^{-1}. Solid electrolytes enable higher energy density designs due to their ability to pack more active materials in a given volume or weight compared to liquid electrolytes. To assess stability, cyclic testing was conducted under a charge-discharge at a current density of 5 Ag^{-1}, revealing an impressive 89% capacitance retention over 8000 cycles (fig.4 b). The coloumbic efficiency of 100 % was also observed for our device. This performance is attributed to the stable nature of PVA-$ZnSO_4$ as electrolyte membrane and MWCNTs as cathode.

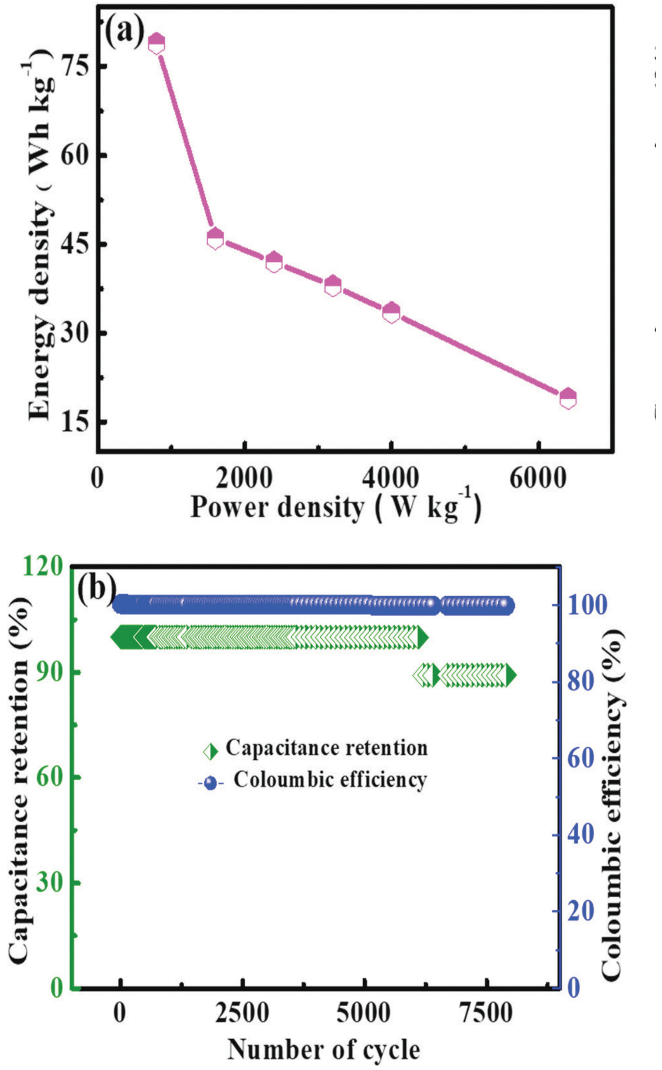

Fig.5 (a) *Ragone plot*, and ***(b)*** *stability performance of MWCNT-ZIHC.*

Conclusions

Here, we successfully synthesized MWCNTs via CVD method, where green tea extracts derived iron nanoparticles served as catalysts. The MWCNTs electrodes showed improved electrochemical performance in ZIHC, achieving a high specific capacitance of 221 F g^{-1} at 1 A g^{-1}, with an excellent energy density of 78.9 W h kg^{-1} at 800 W kg^{-1} power density, making it a promising energy device. Furthermore, the device exhibited 89% capacitance retention and 100% coulombic efficiency, demonstrating stability with the synthesized MWCNTs. This research offers important insights into optimizing the MWCNTs for applications in solid electrolyte zinc-ion hybrid capacitors.

Declaration of competing interest

The authors declare that they have no known competing financial interests or personal relationships that could have appeared to influence the work reported in this paper.

Acknowledgments

The authors acknowledge the support of IIT (BHU) for and its Central Instrument Facility for SEM and TEM study. AKM acknowledges the support of DST, India (grant no. IFA14-MS25). AP acknowledges UGC, India for providing the research fellowship.

Reference

1. J. Yin, W. Zhang, N. A. Alhebshi, N. Salah, and H. N. Alshareef, Adv Energy Mater **11**, 2100201 (2021).
2. A. K. Mishra and S. Ramaprabhu, J Nanosci Nanotechnol **12***,* 6658 (2012).
3. S. Mishra, R. K. Gupta, and A. K. Mishra, Materials Science and Engineering: B **300**, 117129 (2024).
4. C. Singh, S. Nikhil, A. Jana, A. K. Mishra, and A. Paul, Chemical Communications **52**, 12661 (2016).
5. H. Liu, X. Liu, S. Wang, H. K. Liu, and L. Li, Energy Storage Mater **28**, 122 (2020).
6. H. Wang, Z. Wang, P. Bai, S. Hu, Y. Zhang, and R. Wang, Advances in Engineering Software **117**, 1 (2018).

7. S. Mishra, B. P. Majee, P. K. Maurya, and A. K. Mishra, Mater Res Express **6**, 088257 (2019).
8. Z. Li, Y. An, S. Dong, C. Chen, L. Wu, Y. Sun, and X. Zhang, Energy Storage Mater **31**, 252 (2020).
9. J. Liu, Z. Khanam, S. Ahmed, T. Wang, H. Wang, and S. Song, ACS Appl Mater Interfaces **13**, 16454 (2021).
10. A. K. Mishra and S. Ramaprabhu, AIP Adv **2**, 022121 (2012).
11. C. Singh, A. K. Mishra, and A. Paul, J Mater Chem A Mater **3**, 18557 (2015).
12. D. Zhang, L. Li, Y. Gao, Y. Wu, and J. Deng, ChemElectroChem **8**, 1541 (2021).
13. T. Lin, I. W. Chen, F. Liu, C. Yang, H. Bi, F. Xu, and F. Huang, Science (1979) **350**, 1508 (2015).
14. O. Okhay, A. Tkach, M. J. H. Gallo, G. Otero-Irurueta, S. Mikhalev, P. Staiti, and F. Lufrano, J Energy Storage **32**, 101839 (2020).
15. H. Chen, Y. Zheng, X. Zhu, W. Hong, Y. Tong, Y. Lu, G. Pei, Y. Pang, Z. Shen, and C. Guan, Mater Res Bull **139**, 111281 (2021).
16. S. Sarkar, A. Arya, U. K. Gaur, and A. Gaur, Biomass Bioenergy **142**, 105730 (2020).
17. A. Samage, M. Halakarni, H. Yoon, and N. Sanna Kotrappanavar, Carbon **219**, 118789 (2024).
18. K. Tang, L. Fu, R. J. White, L. Yu, M. M. Titirici, M. Antonietti, and J. Maier, Adv Energy Mater **2**, 873 (2012).
19. P. Liu, W. Liu, Y. Huang, P. Li, J. Yan, and K. Liu, Energy Storage Mater **25**, 858 (2020).
20. J. Huang, L. Wang, Z. Peng, M. Peng, L. Li, X. Tang, Y. Xu, L. Tan, K. Yuan, and Y. Chen, J Mater Chem A Mater **9**, 8435 (2021).
21. X. Chu, X. Zhao, Y. Zhou, Y. Wang, X. Han, Y. Zhou, J. Ma, Z. Wang, H. Huang, Z. Xu, C. Yan, H. Zhang, W. Yang, and J. Chen, Nano Energy **76**, 105179 (2020).
22. V. Sahu, R. B. Marichi, G. Singh, and R. K. Sharma, Electrochim Acta **240**, 146 (2017).
23. X. Chu, G. Chen, X. Xiao, Z. Wang, T. Yang, Z. Xu, H. Huang, Y. Wang, C. Yan, N. Chen, H. Zhang, W. Yang, J. Chen, X. Chu, Z. Wang, T. Yang, Z. Xu, H. Huang, Y. Wang, C. Yan, N. Chen, H. Zhang, W. Yang, G. Chen, X. Xiao, and J. Chen, Small **17**, 2100956 (2021).
24. X. Judez, H. Zhang, C. Li, G. G. Eshetu, J. A. González-Marcos, M. Armand, and L. M. Rodriguez-Martinez, J Electrochem Soc **165**, 6008 (2018).
25. W. G. Suci, H. K. Aliwarga, Y. R. Azinuddin, R. B. Setyawati, K. N. R. Stulasti, and A. Purwanto, Open Engineering **12**, 409 (2022).
26. V. Sahu, M. Mishra, G. Gupta, G. Singh, and R. K. Sharma, ACS Sustain Chem Eng **5**, 450 (2017).
27. S. Jung, Y. Myung, G. S. Das, A. Bhatnagar, J. W. Park, K. M. Tripathi, and T. Kim, New J Chem**. 44**, 7369 (2020).
28. B. Zhang, D. Wang, B. Yu, F. Zhou, and W. Liu, RSC Adv **4**, 2586 (2013).
29. D. Mohapatra, S. Badrayyana, and S. Parida, Mater Chem Phys **174**, 112 (2016).
30. B. Wei, M. Wen, Y. Zhao, C. Yang, J. Qiu, and L. Zang, Ionics (Kiel) **29**, 429 (2023).
31. H. Wang, M. Wang, and Y. Tang, Energy Storage Mater **13**, 1 (2018).
32. S. Chen, L. Ma, K. Zhang, M. Kamruzzaman, C. Zhi, and J. A. Zapien, J Mater Chem A Mater **7**, 7784 (2019).
33. N. Tripathi, V. Pavelyev, and S. S. Islam, Appl. Nanosci. **7**, 557 (2017).
34. B. M. Chufa, H. C. A. Murthy, B. A. Gonfa, and T. Y. Anshebo, Green Chem Lett Rev **14**, 640 (2021).
35. S. Mishra, S. S. Jaiswal, and A. K. Mishra, J. Mater. Sci.: Mater. Electron. **33**, 8702 (2022).
36. A. Aqel, K. M. M. A. El-Nour, R. A. A. Ammar, and A. Al-Warthan, Arab. J. Chem. **5**, 1 (2012).

37. M. Flygare and K. Svensson, Mater Today Commun **18**, 39 (2019).
38. E. Picheau, A. Impellizzeri, D. Rybkovskiy, M. Bayle, J. Y. Mevellec, F. Hof, H. Saadaoui, L. Noé, A. C. Torres Dias, J. L. Duvail, M. Monthioux, B. Humbert, P. Puech, C. P. Ewels, and A. Pénicaud, ACS Nano **15**, 596 (2021).
39. A. C. Ferrari and D. M. Basko, Nat. Nanotechnol **8**, 235 (2013).
40. P. K. Maurya and A. K. Mishra, J. Phys. Chem. Lett **15**, 1246 (2024).
41. P. Connor, J. Schuch, B. Kaiser, and W. Jaegermann, Zeitschrift Fur Physikalische Chemie **234**, 979 (2020).
42. S. Mishra, P. K. Maurya, and A. K. Mishra, Mater Chem Phys **255**, 123551 (2020).

The Direct Ammonia Fuel Cell: Revolutionary Applications in the Field of Renewable Energy

Shankab J. Phukan,[1†] Suraj Goswami,[1†] Tarun Yadav,[1] Vishnu Panicker,[2] Mousumi Biswas,[1] Praveen Mourya,[1] Manoj Kumar Sharma,[3] Ranjith Krishna Pai,[3] Manas Roy,[4]* Somenath Garai[1]**

[1] Department of Chemistry, Institute of Science, Banaras Hindu University, Varanasi- 221005.

[2] Mechanical Engineering Division, School of Engineering, Cochin University of Science and Technology, Kochi, Kerala- 682022.

[3] Technology Mission Division, Department of Science and Technology, Government of India, Technology Bhavan, New Mehrauli Road, New Delhi- 110016.

[4] Department of Chemistry, National Institute of Technology Agartala, Agartala, Tripura- 799 046.

Corresponding Authors Email IDs: ranjith.krishnapai@gov.in; mroyiitk@gmail.com; sgarai@bhu.ac.in

[†]The authors contributed equally in preparation of the article

Keywords : *Ammonia Fuel Cell; Hydrogen Energy Carrier; Solid Oxide Fuel Cell; Alkaline Fuel Cell; Alkaline Membrane-based Fuel Cell*

Abstract

Ammonia, being a prospective ancillary hydrogen energy carrier, with traditional storage and distribution associations, discloses as a convenient energy source. The incipient concept of ‘green ammonia, produced *via* greener routes, could unfold futuristics markets and assist decarbonize various fossil fuel-dependent applications. This review outlines a contrastive analysis of direct ammonia fuel cells, operational principles, advantages as well as shortcomings. It emphasizes the contemporary developments and technology’s readiness for future implementations. Current complications regarding the NO_x species formation, selection of materials, constrained power densities, carbon dioxide endurance and long-lasted durability, are also deliberated.

1. Introduction

Over the past few years, the excessive use of carbon-based non-renewable fuels has wreaked havoc both on the wellbeing of the mankind and the environment, prompting the long-lasting search for cleaner alternatives, recognizing the potential of green hydrogen as a superlative renewable energy fuel [1]. However, transitioning to the greener hydrogen fuel requires the advancement of viable production, supply and particularly suitable ambient conditions assisted storage engineering, which are not adequately suitable in the contemporary times, due to its low energy density and safety concerns[2,3]. Ammonia, with its high hydrogen content and existing substructure for distribution, has been utilized periodically in the earlier times as a potential fuel for fuel cells and internal combustion engines (ICEs), as depicted in **Figure 1** [3,4].The ammonia has significantly notable advantages as a transportation fuel, which can be relatively compared with liquid hydrogen. Also, it showcases higher density to tackle the infrastructural and storage problems as compared to hydrogen fuel. Despite its toxicity, ammonia claims various advantages like high-

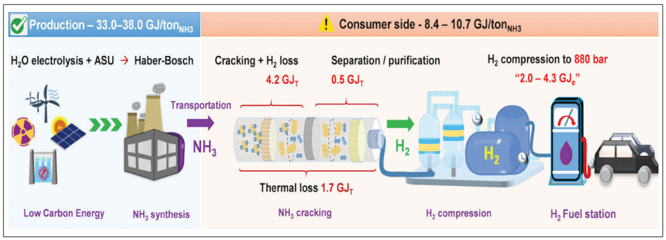

Figure 1: Pictorial depiction of production, supply and utiliztion pathway of NH_3 as a potential green energy vector. Reproduced with permission from *ref*. 3. Copyright 2021 American Chemical Society

octane rating along with facile thermal cracking to produce hydrogen. [5,6] The worldwide distribution system of ammonia is already well-established, and it's also safer than other fuels, due to its unique properties, like rapid degeneracy, low flammability and facile detection process. Furthermore, synthesis of ammonia can be carried out from various sources, such as all kinds of fossil fuels (*e.g.*, natural gas, coal, naphtha, petroleum *etc.*), from other green energy resources (*e.g.*, wind, solar, geothermal, hydro, heat waste, ocean and nuclear *etc.*), *via* employing biomass, water, organic waste (including metropolitan wastes) and air as major power supplies, making it an environmentally friendly alternative[7] . As ammonia decomposes into water and nitrogen, which are abundantly available in the Earth's atmosphere, it can be considered as fully recyclable material. As it is mentioned above, the very technologies for extracting hydrogen from ammonia, like thermal cracking and electrolysis, are already in development, though it remains a challenge to make compact, operational and efficient designs. Since the year 1966, several studies have been developed by the scientific and industrial communities on the latent utilizations of ammonia in fuel cells. Ammonia has already been employed to power the regular fuel cells. Recent advances have led to the development of proton conducting solid oxide membranes that can also function at elevated temperatures[8,10]. These membranes are beneficial in several ways:

i. Facilitation of ammonia molecules to break down into useful components at one part of the fuel cell.

ii. Facile transference of the protons through the membrane from one side of the cell to the other, which eventually generates water releasing energy.

iii. The process exhausts the overall fuel supply, thereby mitigating the necessity for additional procedures.

iv. Upon the completion of the process, the enduring nitrogen can be employed in various operations or safely discharged into the atmosphere.

When the hydrogen gas is being obligated to be extracted from ammonia, there are two main methods: thermochemical processes and electrochemical processes. Alternatively, in fuel cell ammonia can directly be used, without requiring prior decomposition or cracking. The fuel cell technology mainly generates electricity from chemical sources through electrochemical reactions. Generally, depending upon the materials subjected as electrolytes, their future applications, and the conditions under which they operate, fuel cells can be classified in different types. These classes include solid oxide fuel cell (SOFC), proton exchange membrane fuel cell (PEMFC), alkaline membrane fuel cell (AMFC), alkaline fuel cell (AFC) *etc* [11,12].

The extensive utilization of fuel cells in various domains of renewable and sustainable energy production consequently presents distinctive challenges that requires deliberate scientific attentions. One of the major hurdles impeding the development of ammonia fed fuel cells is the lack of efficient and cost-effective technologies associated with production, assembly and distribution[14] . Contemporary methods of ammonia synthesis for fuel cells predominantly encompass the energy-intensive Haber-Bosch process, which profoundly relies on carbon-based fossil fuels which emits significant amounts of greenhouse gases[15]. Furthermore, the marginal infrastructure which is obligatory for the widespread supply of ammonia as a fuel source is still underdeveloped. Without any inclusive clarification to these challenges, the potential advantages of ammonia fuel cells may not be fully comprehended. Therefore, the articulation of the problem resides in the development of innovative and sustainable techniques for ammonia production and storage [15], while simultaneously establishing a robust circulation network to support the incorporation of ammonia fuel cells into the vast domain of renewable energy. As we thoroughly investigate the potentials of ammonia fed fuel cells as a novel sustainable energy source, it is exceedingly crucial to develop distinct research questions that will steer our investigation and analysis. The major questions may concentrate upon the efficiency and effectiveness of ammonia fuel cells in comparison to the pristine fuel sources, the global environmental and economic consequences of ammonia production and utilization, and the scalability of ammonia fed fuel cell technologies for pervasive utilization in numerous sectors. By considering these research questions, we can improve the comprehensive understanding of the viability and real-time practicality of incorporating ammonia fuel cells into the worldwide renewable energy framework. Additionally, estimating the financial inferences and the regulatory infrastructures encompassing the ammonia fuel cells can deliver valuable perceptions into their long-term implacability as novel green energy solution. Through meticulous research and analysis, we can facilitate the ammonia revolution to emerge as a feasible and operative substitution to the conventional energy sources[16].

2. Fundamentals of Ammonia Fuel Cell

The alteration regarding the Renewable Energy Sources (RES) and the imperative necessity to address the prevailing energy crisis have driven the exploration of alternative energy generation methods. Within this landscape, fuel cells have been developed as a fruitful technology for sustainable energy production. Particularly, the development of high-gain DC–DC boost converters has facilitated the integration of fuel cells, such as hydrogen fuel cells, into various applications, including electric vehicles (EVs) and utility grids[17]. Furthermore, as countries worldwide strive to meet their energy demands while adhering to sustainable goals, the focus on H_2-based energy storage infrastructure has intensified, with water electrolysis playing a crucial role in large-scale hydrogen production for fuel cells and other electrochemical applications[18]. This intensive initiative not only establishes the foundation for a greener energy economy but also emphasizes the potential of fuel cells, especially ammonia-fed fuel cells, as a real-time implacable and effective green energy substitution technology with noteworthy economic reimbursements and environmental advantages.

Meticulous investigations associated with various classes of fuel cells are indispensable in advancing the development of renewable energy technologies. The proton exchange membrane fuel cells (PEMFCs) are among the most frequently employed fuel cell technologies, owing to their relatively reduced operating temperatures, high-power density, and rapid starting periods. Meanwhile, solid oxide fuel cells (SOFCs) function at comparatively elevated temperatures and are extremely efficient in fuel-to-electricity conversion, making them apposite for stationary power generation applications. Meanwhile, the alkaline fuel cells (AFCs) represent an established and efficient technology in the operative domain of fuel cell systems, harnessing an alkaline electrolyte to accomplish effective reduction of oxygen and oxidation of hydrogen reactions. Recognizing their abilities to function at diminished temperature conditions and their epoch-making implementation in space exploration, AFCs endure to be a crucial domain of investigation for sustainable and high-efficiency energy solutions. Whereas, the alkaline membrane-based fuel cells (AMFCs) unfold a novel method associated to the fuel cell technology by incorporating a polymer-based membrane enable of conducting hydroxide ions. This advancement augments the holistic performance and endurability of the fuel cell, making AMFCs a promising futuristic substitution for a broad spectrum of applications, from mobile power devices to large industrial-scale energy systems.

The above discussed esteemed classes of direct ammonia fuel cells (DAFCs) have been acquiring considerations for their aptitude to utilize ammonia as a green and renewable fuel source. These various classes of fuel cells provide distinct advantages as well as challenges, providing an assorted landscape of options for the amalgamation of sustainable green energy sources into the contemporary energy systems. By venturing the assets and limitations of each class of fuel cell technology, the scientific community can conclude facile evaluations for the most suitable options with diversified applications in the evolution towards a greener energy future.[16]

Commercially available precious metal based electrocatalysts, such as PtIr/C, Pt/C, and PtRu/C[19], along with ruthenium-based catalysts like Ru/Al_2O_3, Ru/MgO, Ru/CNT, as well as metal alloy based catalysts have been extensively employed as anode materials. However, the high cost and limited availability of Pt, Ru and Ir metals significantly constrain the large-scale application in fuel cells. This limitation underscores the development of non-precious metal catalysts for cost-effective, efficient, and durable alternatives.

Recently, Ni-based catalysts exhibit as a promising alternative due to its affordability and higher intrinsic ammonia oxidation reactivity. Some metal alloy catalysts such as Ni-Fe, Ni-Cu[20], Ni-Mo[21], Co-Ni-P have shown considerable potential. Additionally, transition metal nitrides and carbides *e.g.*, Fe–N–C[22], metal oxide such as TiO nanofibers[23] and Metal-Organic-Frameworks (MOF) derived materials have been extensively explored. Notably, Zhang *et al*. have synthesized a ternary NiCuFe alloy that exhibited remarkable catalytic activity and durability as an electrode in commercial anion exchange membrane (AEM) electrolytes[24]. Jiang *et al*. have deposited $NiCo_2N$ composite on Ni foam, which has demonstrated significant efficacy as an electrode material for electrocatalytic decomposition of ammonia[25].

2.1. Solid Oxide Fuel Cell (SOFC)

SOFCs are often contemplated as the most effective device to generate power by the chemical energy translation into electrical energy and are amongst the frequently investigated category of ammonia-based fuel cells[26]. SOFCs has excellent efficiency regarding energy conversion operations and offers tremendous flexibility in the overall fuel utilization. Ammonia cracking, occurring in these systems, particularly takes place at high temperatures ranging from 500°C and 1000°C. One significant benefit of the applied high temperature conditions is that the breakdown of ammonia and power generating processes can be efficiently merged. Therefore, without the need of pre-processing, ammonia can be employed directly in SOFCs[27,28]. The elevated temperature conditions also[16]. Reduce the requirement and cost of a discrete separate unit to decompose ammonia, and also improves the electrolyte's capability to transfer ions, thus dropping the electrical losses[26]. In 1980, the initial direct ammonia SOFC was pioneered by Vayenas and Farr [29]. Their major objective was to operate nitric oxide as a viable feed material, while electricity being generated concurrently. The fuel cell contained of Pt electrodes along with a ZrO_2 zirconia (YSZ) electrolyte stabilized *via* Y_2O_3[30,31]. Meanwhile, YSZ is the one of the most extensively utilized electrolyte, which is due to the augmented ion mobility, which facilitates the operative movement of oxygen ions throughout the electrolyte, thereby lowering internal resistance. Moreover, similar solid electrolytes exhibit an augmented thermal and chemical stability, which is also critical for high temperature applications[32]. Another conventional anode, Ni/YSZ (Nickel/yttria-stabilized zirconia) for SOFCs efficiently decomposes ammonia at elevated temperatures above 700˚C. However, Ba-modified Ni/YSZ (Ba-Ni/YSZ) anode catalyst decomposes at significantly lower temperature[33]. Ceria-based electrolytes, like samarium-doped ceria (SDC), secured potential scientific attentions, owing to their remarkable ionic conductivity even at low temperature conditions[31].

Owing to the sluggish diffusions of oxygen ions across the employed electrolyte, equation (1) becomes the step that limits the rate of reaction. Meanwhile, the most pertinent question can be "what causes the NO level to approach 60%?". Initially, the prior purpose of the technology was to generate sufficient power to produce nitric oxide, although, the nitric oxide formation is not preferable, when the fuel cell is completely employed to generate electricity[29]. Consequently, the advancement of SOFC has relocated towards producing N_2 as the only nitrogenous compound.

Solid oxide fuel cells are categorized into two types: oxygen-ion-conducting (SOFC-O) and proton-conducting (SOFC-H). For SOFC-O, the anode side reactions resemble with reactions (1) and (2), while the cathode side reaction corresponds to the reaction

(3), which is depicted in **Figure 2**.

Anode reaction : $5O^{2-} + 2NH_3 \rightarrow 2NO + 3H_2O + 10e^-$ (1)
$3NO + 2NH_3 \rightarrow 5/2N_2 + 3H_2O$ (2)
Cathode reaction : $O_2 + 2\,e^- \rightarrow 2\,O^{2-}$ (3)

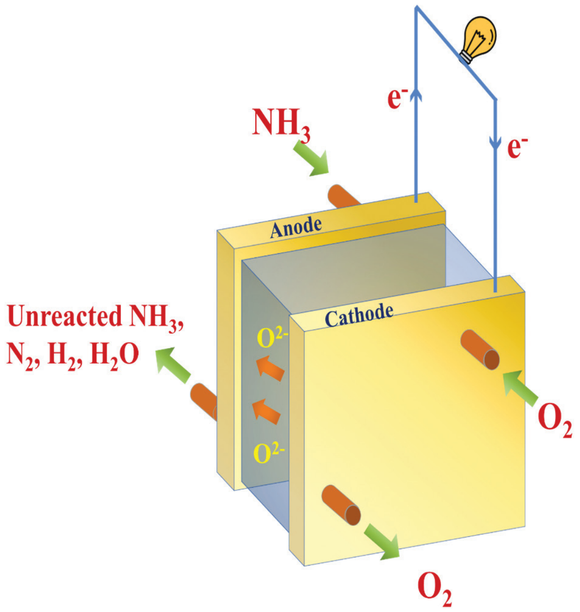

Figure 2: Schematic of the ammonia-fed SOFC-O.

Meanwhile, the working principle is not much different for SOFC-H. The anode side reaction can be represented with reaction (4), where the cathode side reaction resembles with reaction (5), which is depicted in **Figure 3.**

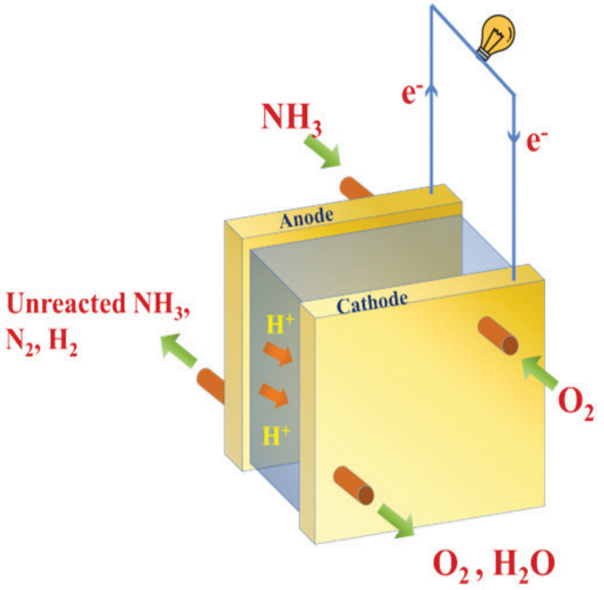

Figure 3: Graphitic design of the ammonia-fed SOFC-H

Anode reaction : $H2 \rightarrow 2H+ + 2e-$ (4)
Cathode reaction : $2H+ + O2 + 2e- \rightarrow H2O$ (5)

Proton mediating electrolytes encompasses a reduced energy barrier for H^+ conduction, which allow SOFC-H to operate potentially at lower temperatures than SOFC-O. Hence, the proton-conducting SOFC inclines to possess advanced energy efficiency[34]. In recent times, several promising electrolytes have been developed which aimed at enhancing the conductivity as well as boosting the power density. Additionally, to reduce nitric oxide formation, doping materials like $BaCeO_3$ and $BaZrO_3$ have been under development, where the employed materials consist of $BaCe_{0.9}Nd_{0.1}O_{3-\delta}$ and $Ce_{0.8}Sm_{0.2}O_{1.9}$[35,36]. Novel lab-scaled ammonia-fed SOFC systems, incorporated with internal combustion engines which are integrated with a stack in a hybrid configuration, were also developed, which achieved a potential efficiency of up to 67.5%[37].

2.2. Alkaline & Alkaline Membrane-Based Fuel Cell

From the initial phases of fuel cell development, alkaline fuel cells (AFCs) are being extensively researched and implemented in real-time feasible systems like transportation vehicles, space applications and energy storage systems *etc*[38-42]. The first generation of ammonia AFC was designed *via* Cairns *et al*[43], in 1960, using a KOH-based electrolyte functioning at temperature ranging from 50 to 200°C[43]. Such systems generate electricity though utilizing an aqueous KOH solution as electrolyte, allowing OH^- species to move throughout the electrolyte for executing the complete circuit and acquiring electrical energy. Subsequent efforts have focused on advancing molten hydroxide electrolytes. According to Hejze *et al*[43]., they reached a power density of order 40 $mW \cdot cm^{-2}$ at 450°C using ammonia fuel and a molten NaOH/KOH electrolyte [44]. A similar system that was capable of achieving a optimum power density of 16 $mW \cdot cm^{-2}$ at 220°C was first investigated by Yang *et al* [45]. In another approach, a direct ammonia-based fuel cell with a molten NaOH/KOH electrolyte established an open circuit voltage of 0.4 V and a highest power density of 0.225 $mW \cdot cm^{-2}$ at 220°C[46]. Although, the main challenge of such fuel cells is the durability performances, as the carbon dioxide present in atmosphere reacts with the OH^- electrolyte to generate carbonate species, like K_2CO_3. These carbonates can form precipitation and potentially impair the cell's performance over time.

Alkaline membrane-based fuel cells (AMFCs) function on parallel principles to that of alkaline fuel cells, where OH^- ions transfer through the electrolyte, as depicted in **Figure 4**. They operate at relatively lower temperatures, typically around 50–120°C[41]. At the cathodic component, significant reaction occurs between oxygen & water to produce hydroxide ions. These hydroxide species then transport through an alkaline-based membrane to the anode producing nitrogen and water, after reacting with ammonia. Upon the utilization of alkaline membrane as the electrolyte, the cathodic and anodic and reactions are given below:

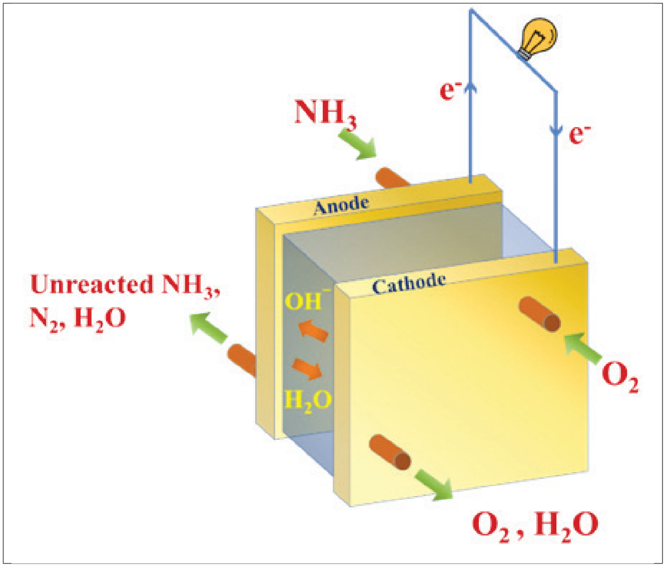

Figure 4: Graphic design of the ammonia-fed AMFC

Anode reaction : $6OH^- + 2NH_3 \rightarrow N_2 + 6H_2O + 6e^-$ (6)
Cathode reaction : $3/2\ O_2 + 3H_2O + 6e^- \rightarrow 6OH^-$ (7)
Overall reaction : $2NH_3 + 3/2\ O_2 \rightarrow N_2 + 3H_2O$ (7)

Since the only products of the ammonia-fed alkaline membrane-based fuel cells are water and nitrogen, this technology is highly recognized for its environmental cleanliness. In contrast to solid oxide fuel cells (SOFCs), where the degradation of ammonia takes place breaking down to the corresponding elements, AMFCs utilize ammonia directly as fuel. This eliminates the requirement for elevated temperatures & ensures that the reaction advances without the need for a decomposition step. [47,48].

To boost the fuel cell power density, hydroxide ions are commonly implemented into the anode to accelerate the reaction described in equation (6). This approach diminishes the dependency of ammonia oxidation on the hydroxide- mass transfer throughout the electrolyte. Therefore, numerous scientific personals examine the impact of both ammonia concentration and OH^- ion concentration on improving performance.

Electrolyte selection for ammonia-fed AMFCs prioritizes augmented ion conductance, elongated chemical durability, and strong mechanical durability. As these particular technologies are also reviewed with the carriage of hydroxide ions, that are generated at the cathodic end and gets utilized at the anodic end, the swelling of electrolyte from water assimilation must also be prevent, which can be considered as a critical consideration for membrane performance[42,49-51]. Unlike conventional AFCs, the susceptibility of the alkaline membranes to reaction with the atmospheric carbon dioxide is high, therefore they do not form precipitates like K_2CO_3 and Na_2CO_3. Instead, the OH^- reacts with the atmospheric carbon dioxide to generate CO_3^{2-} ion.

$$CO_2 + 2OH^- \rightarrow CO_3^{2-} + H_2O \qquad (12)$$

As, such ions possess comparatively reduced specific conductivity, the presence of CO_3^{2-} ions poses challenges like reducing overall membrane conductivity, increasing electrolyte resistance, and resulting in decreased performance. Additionally, carbonate ions reduce the obtainability of hydroxide ions for reacting with ammonia, eventually lowering the regional pH[52]. Therefore, sound chemical durability of a OH^--conducting electrolyte is vital to attain viable endurance of AMFC.

Resembling the SOFCs, the width of the electrolyte in AMFCs is critically important. Thinner membranes decrease ohmic losses by shortening diffusion paths for OH^- ions which improves reactant delivery to the anode. However, maintaining mechanical strength is vital while pursuing thinner membranes. Excessive membrane thinning can lead to fuel permeation, causing fuel crossover and potentially inundating the cathodic end[52]. Recent developments have improved the performance and longevity of membranes in AMFCs by developing anion exchange membranes (AEMs) with boosted mobility and robust mechanical as well as chemical endurance[53]. Significant efforts have been focused towards the development of AEMs that remain stable in alkaline conditions at temperatures of 80°C and above[49,50,54,55]. These membranes are usually integrated with a polymer backbone along with a reinforced ion-conductive component. For example, a poly(aryl piperidinium) membrane that exhibited improved OH^- conductivity with increasing temperature was demonstrated by Wang and team[55]. Similarly, Lee *et al*. observed that OH^- conductivity in a PAP membrane amplified from 54 to 112 $mS \cdot cm^{-1}$ as the temperature rises from 25 to 80°C[49]. At these higher temperature conditions, an enhanced assimilation of water was also observed. These polymer-based membranes show ability for overcoming temperature-related boundaries, which can be observed in conventional AEMs when used in AMFCs.

3. Technological Advancements and Applications of Ammonia Fuel Cell in Renewable Energy

Most of the investigational studies on ammonia-based SOFC anodes have mainly investigated materials based upon nickel. The major issues regarding the utilization of Ni include generation of nitride and particle coarsening throughout the cell operation. Research has mainly emphasized on stabilizing the nickel derived anodes, enhancing the rate of ammonia degradation, and elucidating the impact of supporting materials in the process. Yang *et al*[56]. demonstrated that, although the anodes derived from Ni-YSZ and Ni-SDC revealed similar catalytic activity for ammonia decomposition, the electrochemical activity of the Ni-SDC anode was notably better than the Ni-YSZ anode, in the 500 to 700 °C temperature window. This superior performance is attributed to the superior electrochemical properties of Ni-SDC, which are eminently favourable for the efficient operation of fuel cells. The study emphasizes the importance of material choice in maximizing fuel cell performance and underlines the potential of Ni-SDC as a more efficient anode material in ammonia-fuelled solid oxide fuel cells (SOFCs). The gadolinium-doped ceria (GDC) supports demonstrated better catalytic activity and minimizing activation polarization than yttria-stabilized zirconia (YSZ) supports in Ni-based anode materials, especially at high temperatures up to 800 °C[57]. The improved performance of Ni-GDC can be ascribed to two primary factors: the synergistic interaction prevailing between GDC and Ni, which improves the ammonia degradation characterises, and the improved performance of the Ni-GDC- based anode with H_2 fuel, which further enhances its efficiency with NH_3. The authors reformed the Ni-GDC anode through enlarging the active surface of the GDC, thereby cumulative both the ammonia degradation performance and the electrochemically active three-phase boundary (TPB) region of the anode catalyst. Additionally, bimetallic catalysts show significant potential in assisting NH_3 decomposition. A *d*-block metal with a augmented M-N bond energy, like Mo, Cr or Fe, can be integrated with another metal with a lower bond energy, like Ni. Nickel transmits boosted catalytic characteristic for ammonia degradation, while encouraging the N_2-desorption of from the surface of bimetallic compound[58–62].

The advancements in fuel cell technology, primarily in the naval sector, are transforming the renewable energy sector focusing on sustainability and emissions reduction. Hydrogen, ammonia, and renewable methane assist as clean fuels, with ammonia exhibiting significant potential in Solid Oxide Fuel Cells (SOFCs). Studies reveal impressive electrical efficiency and competitive normalized energy costs, focusing on ammonia's role as a carbon-free energy source. Integrating ammonia fuel cells into existing infrastructure is a significant step towards a financially feasible and environmentally sustainable energy transformation. The transition to sustainable energy is vital for extenuating the environmental influences of fossil fuels. Advanced technologies like high-gain DC-DC boost converters and microbial fuel cells demonstrate potential in enhancing alternative energy sources.[17,63]. By leveraging converter topologies and bioelectric potential from electroactive bacteria, one can augment power generation, mainly with ammonia as a green energy vector. Understanding extremophiles and maximizing microbial fuel cells' bioelectricity conversion capabilities can development the ammonia revolution, auxiliary future energy demands and sustainable practices[63].

To address the challenges of sustainability and environmental impact in the transportation sector, the incorporation of ammonia fuel cells has received substantial focus in the contemporary times. Ammonia has the potential to be a promising energy carrier for marine fuel and renewable energy transport, but its use in road and rail transport is limited due to safety concerns and low energy content.[64]. Ammonia fuel cells offer a sustainable solution in the transportation sector by providing a carbon-free substitute to fossil fuels, remarkably minimizing greenhouse gas emissions. Ammonia produced from renewable sources like solar, wind and hydropower increase its appeal as a clean energy option. By using ammonia fuel cells, vehicles can play a crucial role in achieving eco-friendly transportation systems.[65]. Furthermore, the ammonia based fuel cells are also utilized in the wastewater treatment which is cost effective and energy demanding. Furthermore, microbial fuel cells (MFCs) provide a cost-effective process for converting wastewater into electricity, taking advantage of the energy within the waste[66]. Directly fed ammonia microbial fuel cells (AMFCs) take advantage of high ammonia content without the need for extraction, increasing cost efficiency. Almomani *et al*. demonstrated that electro-oxidation effectively removes more than 96% of the ammonia, making it a viable treatment method[67]. Recent studies show that AMFCs using landfill leachate achieve 96.5% ammonia reduction and produce prominent energy density, showcasing their potential for wastewater applications[68]. The graphical representation of recent and potential progress demonstration of ammonia fuel cell applications as depicted in **Figure 5**.

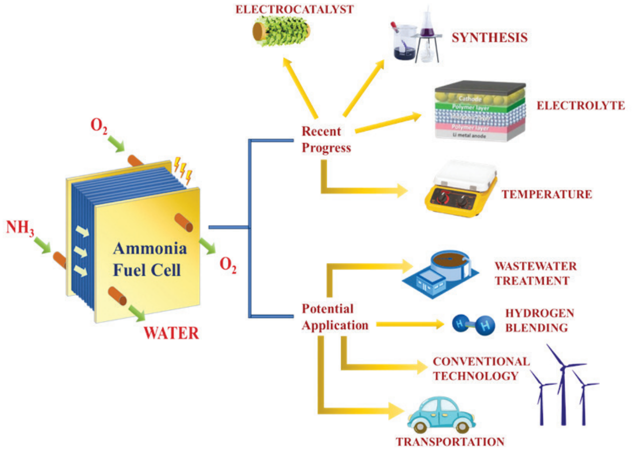

Figure 5: Ammonia fuel cell applications demonstrate sustainable energy solutions in action.

Ammonia fuel cells demonstrate remarkable potential in environmentally friendly energy applications, particularly in SOFCs for marine fuels and wastewater treatment. The advances in stabilizing Ni-based anodes and integrating ammonia fuel cells into current infrastructure show greater potential for efficiency and reduced emissions. Mankind can notably advance renewable energy solutions and address environmental challenges by leveraging ammonia's carbon-free properties and optimizing microbial fuel cells.

4. Environmental and Economic Impacts of Ammonia Fuel Cells

Ammonia fuel cell integration with renewable energy sources has the potential to revolutionize the environment and the economy. Ammonia-based Solid Oxide Fuel Cells (SOFCs) have plenty to offer in terms of environmental benefits. When measured against conventional diesel systems, they reduce greenhouse gas emissions by 92% and NO_x emissions by an incredible 93.4%. The International Maritime Organization's (IMO) progressive goals of lowering greenhouse gas emissions by 50% and CO_2 emissions by 70% by 2050 are ideally aligned with this significant reduction. Adoption of SOFCs operating on ammonia is crucial to the global maritime industry's decarbonization. Diesel and other conventional marine fuels are significant causes of air pollution and greenhouse gas emissions[69,70]. The shipping sector may reduce its environmental effect significantly by switching to ammonia, a fuel that emits no carbon. Particularly interesting are feeder container ships powered by ammonia. These ships mark a revolutionary advancement in the field of zero-carbon maritime transportation. In the maritime industry, feeder ships play a vital role in moving goods from minor ports to larger hubs. These ships can considerably lower the industry's carbon footprint by using ammonia as fuel, improving the environment and the quality of the air. Additionally, SOFCs based on ammonia offer a dependable and effective energy supply. They can use a range of fuels, including renewable ammonia made from green hydrogen, and they run at very high efficiency. This adaptability promotes the incorporation of renewable energy sources into the maritime industry and improves energy security. Ammonia-based SOFCs offer advantages beyond their positive effects on the environment. They provide financial benefits as well. Because ammonia is widely available and has a relatively low cost of manufacture, using it may result in decreased operating expenses. Furthermore, by complying with strict environmental standards, shipping businesses can avoid potential fines and penalties thanks to the lowered emissions[71].

5. Economic Impacts of Ammonia Fuel Cells

Ammonia fuel cells make a strong case for sustainability and cost effectiveness from a financial point of view. Ammonia is a more cost-effective solution for storage and transportation than hydrogen, requiring up to 75% less space in storage. Reductions in production costs to 70% make the ammonia-based SOFC power train, which has a maximum efficiency of 56%, economically feasible. Blue ammonia SOFC systems have an annual levelized cost of energy of only $0.19/kWh and a noteworthy 5.71% reduction in total expenditures. Green ammonia SOFC systems in marine applications support the IMO 2030 target for emission reductions with an amazing cost-effectiveness of $172.92 per tonne of decreased emissions[69]. Transporting ammonia from India to Japan involves a range of expenses. Using a very large gas carrier (VLGC) with a capacity of 55,000 metric tons, which costs US$88 million, the study estimates port charges of $50,000 at Kandla and $60,000 at Tokyo. The round trip of 13,652 nm takes 36 days at 16.5 knots. Fuel consumption is 48 metric tonnes per day at sea and 10 metric tonnes at port, with heavy oil priced at $530 per metric tonne. Total transportation expenses are US$43 per metric ton from Kandla and $36 from Chennai[72]. Table 1 delivers a clear picture of the economic metrics for different types of fuelling systems.

Table 1: Illustration economic feasibility in comparison of price and efficiency parameters of ammonia fuel and other fuels[73–75].

Fuel Type	Physical State	Energy Density	Current International Costing	Fuel Efficiency
Petrol	Liquid	44-46 MJ/kg	$3.59/gallon	22.41 Km/litre (For 1197 cc Engine)
Diesel	Liquid	42-46 MJ/kg	$3.88/gallon	28.4 Km/litre (For 1197 cc Engine)
Compressed Natural Gas (CNG)	Compressed gas (lighter than air)	42-55 MJ/kg	$2.86/GGE (Gallon of Gasoline Equivalent)	31.12 Km/gm (For 1197 cc Engine)
Hydrogen	Compressed gas (lighter than air) or liquid	120-142 MJ/kg	$1.80/GGE (Using Compressed Electrolyses)	148 Km/Litre (Approx.) (For Four Stroke Engine)
Ammonia	Liquid	12.7–15.6 MJ/L	$1.92/GGE	26.67-36.67/Kg NH_3

While large-scale systems have been examined, small-scale systems for distributed power are still less studied. The three proposed systems include: a simple SOFC-engine hybrid, a SOFC with water removal to increase hydrogen concentration, and a SOFC engine with recirculation. Modelling showed that the efficiency of the SOFC-engine hybrid increased by 6.2%, while the efficiency of the recirculation system reached 67.4%. The hybrid recirculation system attained a peak efficiency of

67.5%, showing the unique potential of ammonia-based SOFCs for further development [37]. Wang *et al*. introduced the Ammonia Fuel Cell-Internal Combustion Engine Hybrid Vehicle (AFC-ICE HV), depicted in Figure 6, as a solution to global warming and carbon emissions. This hybrid vehicle presents energy savings, lower grid impact and lower emissions than conventional vehicles. The AFC-ICE HV addresses the limitations of current hybrids by offering lower carbon emissions, higher mileage (1600-2200 km), quick refuelling (3-5 minutes), low operating cost ($0.81-1.12 per 100 km), high energy conversion efficiency (over 80%), and advanced safety features [75].

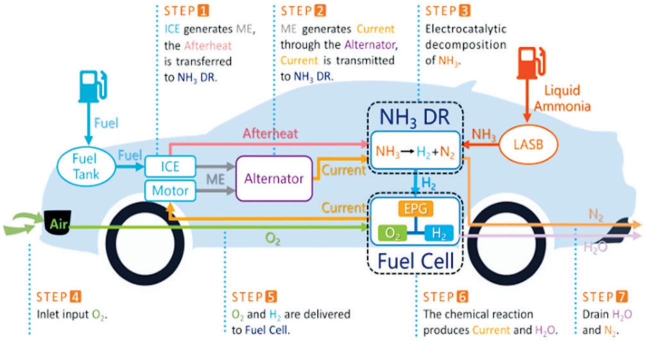

Figure 6: Working Principle of ammonia fuel cell-internal combustion engine hybrid vehicle. Reproduced with permission from ref. 75. Copyright 2023 Elsevier.

The production of green ammonia in India proposes a substantial economic advantage. By expanding its production capacities, India can substantially reduce its import dependence, improve the trade balance and reduce foreign exchange expenditure. [76] Photovoltaic (PV)-based green ammonia production is considered economically viable, with costs expected to be less than 800 €/tonne in many regions, which is competitive compared to conventional methods, especially when integrated with battery storage and other renewable energy sources. India's substantial renewable energy potential, particularly onshore wind and solar power, can meet global ammonia needs, and foster employment growth in the renewable energy sector and related industries.[77] Moving towards green ammonia production also supports India's climate goals by reducing greenhouse gas emissions. A carbon tax of 224 to 335 €/tonne of CO_2 could increase the competitiveness of green ammonia compared to conventional methods, and promote sustainable practices within the industry. Furthermore, committing in NH_3 can diversify India's economy by generating new markets and industries concentrated on sustainable energy solutions, thereby growing economic resilience and motivating technological innovation. The development of green ammonia production facilities and related renewable energy infrastructure will generate a large number of jobs, contribute to the local economy and reduce unemployment. Collectively, these factors ensure a more sustainable and adaptable economy for India[77].

The incorporation of ammonia fuel cells into power plants and transportation vehicles represents an encouraging path toward cost-effectiveness and sustainability, minimizing both operating costs and emissions. As research explores deeper into the economic and environmental impacts of using ammonia fuel cells in energy systems, the potential of these innovative technologies to move forward the ammonia revolution as a green energy alternative becomes more evident.

6. Future Scope & Conclusions

The direct comparison of fuel cell types has become challenging these days due to different testing conditions, which require explicit evaluation to determine the best technology for specific applications based on performance criteria. Ammonia-based solid oxide fuel cells (SOFCs) and ammonia microbial fuel cells (AMFCs) demonstrate encouraging outcomes in hybrid systems, transportation, and wastewater treatment.

Hybrid systems show a viable path towards incorporating ammonia as an energy carrier in the near future, which will aid its acceptance and utilization. By combining SOFCs with gas turbines (GTs) in pressurized environments, achieved remarkable efficiencies of up to 70%, far exceeding conventional SOFC performance. Studies demonstrated that ammonia-fuelled SOFCs exhibit increased power density with atmospheric pressure, highlighting their potential in hybrid

SOFC-GT systems. The integration into combined cooling, heating and power cycles further increases efficiency and takes advantage of the refrigeration properties of ammonia in a cost-effective manner.[78,79].

In transportation, ammonia-fuelled SOFCs are incipient for cleaner applications. Integrated with gas turbines and ammonia-organic Rankine cycles, these systems efficiently recover and utilize waste heat, achieving elevated energy efficiency of up to 79.88%. Such systems are particularly suitable for powering fuel cell vehicles (FCVs) and providing hydrogen for small-scale refuelling stations, ensuring that energy demand can be met sustainably without CO_2 emissions[80–82].

Ammonia-rich wastewater presents undeveloped energy resources for SOFC applications. Technologies such as microbial fuel cells (MFCs) and direct ammonia-based AMFCs provide efficient means for converting sewage directly into electricity, reducing operating costs and environmental impacts. Processes such as struvite decomposition extract ammonia for SOFC fuel, demonstrating noteworthy energy recuperation potential and reduced CO_2 emissions compared to conventional wastewater treatment[83,84]. Studies comparing different feedstocks for SOFCs, including ammonia derived from renewable sources such as wind electrolysis, highlight their potential to significantly reduce the impacts of climate change. Ammonia-based SOFCs generate approximately 0.16 kg CO_2 per kWh of electricity, demonstrating their environmental superiority over natural gas-based alternatives[12].

Ammonia-based fuel cells, particularly SOFCs and AMFCs, represent a prospective improvement in energy technology, poised to meet diverse application needs ranging from hybrid power generation to sustainable transportation and wastewater management. Their integration into hybrid systems enhances efficiency and reliability, supporting a transition towards cleaner energy solutions. Moving forward, continued research and development are essential to optimize performance, expand application possibilities, and ensure the environmental and economic viability of ammonia as a key component in future energy systems.

Acknowledgments

Mr. Phukan, Mr. S. Goswami and Dr. Garai are thankful to DST, MoM, SERB, BHU-IOE-SEED Grant, and ISM TexMin funded Projects for their kind financial help. Dr. M. Biswas and Dr. T. Yadav would like to thank Raja Jwala Prasad Post-Doctoral Fellowship and Chanakya Post-Doctoral Fellowship for the financial support provided to them respectively. The authors are highly thankful to all the eminent scientific persons enlisted in this review for their contributions to this field. Permission received from corresponding editors of the journal for the reproduction of their figures in this review article is gratefully acknowledged. The authors would like to thank the Department of Chemistry, Institute of Science, Banaras Hindu University, Varanasi, Cochin University of Science and Technology, National Institute of Technology Agartala for their encouragement and support.

References:

1. T. N. Veziroğlu and S. Şahi˙n, *Energy Conversion and Management*, **49**, 1820–1831 (2008) https://linkinghub.elsevier.com/retrieve/pii/S0196890407004281.
2. J. O. Jensen, A. P. Vestbø, Q. Li, and N. J. Bjerrum, *Journal of Alloys and Compounds*, **446–447**, 723–728 (2007) https://linkinghub.elsevier.com/retrieve/pii/S092583880700864X.
3. S. Chatterjee, R. K. Parsapur, and K.-W. Huang, *ACS Energy Lett.*, **6**, 4390–4394 (2021) https://pubs.acs.org/doi/10.1021/acsenergylett.1c02189.
4. H. J. Bomelburg, in, vol. PNL-SA-9057; CONF-8110146-1; ON: DE82006163, Pacific Northwest Lab., Richland, WA (USA) https://www.osti.gov/biblio/5718175.
5. P. J. Feibelman and R. Stumpf, (2006).
6. M. Jiang, D. Zhu, and X. Zhao, *Journal of Energy Chemistry*, **23**, 1–8 (2014) https://linkinghub.elsevier.com/retrieve/pii/S2095495614601108.

7. P. G. Grimes, *SAE Transactions*, **74**, 281–326 (1966) https://www.jstor.org/stable/44460523.

8. C. Zamfirescu and I. Dincer, *Fuel Processing Technology*, **90**, 729–737 (2009) https://linkinghub.elsevier.com/retrieve/pii/S0378382009000241.

9. K. Xie et al., *Journal of Power Sources*, **170**, 38–41 (2007) https://linkinghub.elsevier.com/retrieve/pii/S0378775307007033.

10. N. Maffei, L. Pelletier, J. P. Charland, and A. McFarlan, *Fuel Cells*, **7**, 323–328 (2007) https://onlinelibrary.wiley.com/doi/10.1002/fuce.200600038.

11. S. Mekhilef, R. Saidur, and A. Safari, *Renewable and Sustainable Energy Reviews*, **16**, 981–989 (2012) https://linkinghub.elsevier.com/retrieve/pii/S1364032111004709.

12. G. Jeerh, M. Zhang, and S. Tao, *J. Mater. Chem. A*, **9**, 727–752 (2021) https://xlink.rsc.org/?DOI=D0TA08810B.

13. S. Joseph Sekhar, A. Said Ahmed Al-Shahri, G. Glivin, T. Le, and T. Mathimani, *Fuel*, **358**, 130307 (2024) https://linkinghub.elsevier.com/retrieve/pii/S0016236123029216.

14. A. Valera-Medina and R. Banares-Alcantara, *Techno-Economic Challenges of Green Ammonia as an Energy Vector*, p. 340, Academic Press, (2020).

15. H. Ishaq and C. Crawford, *Energy Conversion and Management*, **300**, 117869 (2024) https://linkinghub.elsevier.com/retrieve/pii/S0196890423012153.

16. I. Dincer and O. Siddiqui, *Ammonia Fuel Cells*, p. 266, Elsevier, (2020).

17. J. Veerabhadra and S. Nagaraja Rao, *Energy Harvesting and Systems*, **0** (2023) https://www.degruyter.com/document/doi/10.1515/ehs-2022-0144/html.

18. R. Ramachandran et al., *RSC Adv.*, **12**, 28227–28244 (2022) https://xlink.rsc.org/?DOI=D2RA04853A.

19. R. Chen et al., *International Journal of Hydrogen Energy*, **46**, 27749–27757 (2021) https://linkinghub.elsevier.com/retrieve/pii/S0360319921020942.

20. W. Xu et al., *Applied Catalysis B: Environmental*, **218**, 470–479 (2017) https://linkinghub.elsevier.com/retrieve/pii/S0926337317306458.

21. Y. Chen et al., *Mater. Adv.*, **4**, 2868–2873 (2023) https://xlink.rsc.org/?DOI=D3MA00151B.

22. S. Shen et al., *Journal of Power Sources*, **496**, 229817 (2021) https://linkinghub.elsevier.com/retrieve/pii/S0378775321003578.

23. S. Zhang et al., *International Journal of Hydrogen Energy*, **46**, 39208–39215 (2021) https://linkinghub.elsevier.com/retrieve/pii/S036031992103723X.

24. M. Zhang et al., *J. Mater. Chem. A*, **10**, 18701–18713 (2022) https://xlink.rsc.org/?DOI=D2TA04129D.

25. K. Jiang et al., *Electrochimica Acta*, **403**, 139700 (2022) https://linkinghub.elsevier.com/retrieve/pii/S0013468621019848.

26. M. Ni, M. K. H. Leung, and D. Y. C. Leung, *Int. J. Energy Res.*, **33**, 943–959 (2009) https://onlinelibrary.wiley.com/doi/10.1002/er.1588.

27. N. M. Adli, H. Zhang, S. Mukherjee, and G. Wu, *J. Electrochem. Soc.*, **165**, J3130–J3147 (2018) https://iopscience.iop.org/article/10.1149/2.0191815jes.

28. A. Wojcik, H. Middleton, I. Damopoulos, and J. Van Herle, *Journal of Power Sources*, **118**, 342–348 (2003) https://linkinghub.elsevier.com/retrieve/pii/S0378775303000831.

29. C. G. Vayenas and R. D. Farr, *Science*, **208**, 593–594 (1980) https://www.science.org/doi/10.1126/science.208.4444.593.

30. T. Matsui et al., *J. Electrochem. Soc.*, **168**, 104509 (2021) https://iopscience.iop.org/article/10.1149/1945-7111/ac27dc.

31. G. G. M. Fournier, I. W. Cumming, and K. Hellgardt, *Journal of Power Sources*, **162**, 198–206 (2006) https://linkinghub.elsevier.com/retrieve/pii/S0378775306011554.

32. A. Afif et al., *Renewable and Sustainable Energy Reviews*, **60**, 822–835 (2016) https://linkinghub.elsevier.com/retrieve/pii/S1364032116001611.

33. Y. Wang et al., *J. Electrochem. Soc.*, **167**, 064501 (2020) https://iopscience.iop.org/article/10.1149/1945-7111/ab7b5b.

34. M. Ni, D. Y. C. Leung, and M. K. H. Leung, *Journal of Power Sources*, **183**, 682–686 (2008) https://linkinghub.elsevier.com/retrieve/pii/S0378775308009828.

35. Z. Li et al., *Science and Technology of Advanced Materials*, **8**, 566–570 (2007) http://www.tandfonline.com/doi/full/10.1016/j.stam.2007.08.009.

36. G. Meng, C. Jiang, J. Ma, Q. Ma, and X. Liu, *Journal of Power Sources*, **173**, 189–193 (2007) https://linkinghub.elsevier.com/retrieve/pii/S0378775307009123.

37. T.-Q. Quach, V.-T. Giap, D. Keun Lee, T. Pineda Israel, and K. Young Ahn, *Applied Energy*, **324**, 119718 (2022) https://linkinghub.elsevier.com/retrieve/pii/S0306261922010091.

38. E. Gülzow, *Journal of Power Sources*, **61**, 99–104 (1996) https://linkinghub.elsevier.com/retrieve/pii/S0378775396023440.

39. G. McLean, *International Journal of Hydrogen Energy*, **27**, 507–526 (2002) https://linkinghub.elsevier.com/retrieve/pii/S0360319901001811.

40. M. Wang et al., *ACS Energy Lett.*, **4**, 2104–2110 (2019) https://pubs.acs.org/doi/10.1021/acsenergylett.9b01407.

41. G. Merle, M. Wessling, and K. Nijmeijer, *Journal of Membrane Science*, **377**, 1–35 (2011) https://linkinghub.elsevier.com/retrieve/pii/S0376738811003085.

42. E. J. Park and Y. S. Kim, *J. Mater. Chem. A*, **6**, 15456–15477 (2018) https://xlink.rsc.org/?DOI=C8TA05428B.

43. E. J. Cairns, E. L. Simons, and A. D. Tevebaugh, *Nature*, **217**, 780–781 (1968) https://www.nature.com/articles/217780a0.

44. T. Hejze, J. O. Besenhard, K. Kordesch, M. Cifrain, and R. R. Aronsson, *Journal of Power Sources*, **176**, 490–493 (2008) https://linkinghub.elsevier.com/retrieve/pii/S0378775307016163.

45. J. Yang, H. Muroyama, T. Matsui, and K. Eguchi, *Journal of Power Sources*, **245**, 277–282 (2014) https://linkinghub.elsevier.com/retrieve/pii/S0378775313011506.

46. O. Siddiqui and I. Dincer, *Energy*, **169**, 914–923 (2019) https://linkinghub.elsevier.com/retrieve/pii/S0360544218324629.

47. J. C. Ganley, *Journal of Power Sources*, **178**, 44–47 (2008) https://linkinghub.elsevier.com/retrieve/pii/S0378775307026468.

48. K. Kordesch et al., *Journal of Power Sources*, **86**, 162–165 (2000) https://linkinghub.elsevier.com/retrieve/pii/S0378775399004292.

49. W.-H. Lee et al., *ACS Macro Lett.*, **6**, 566–570 (2017) https://pubs.acs.org/doi/10.1021/acsmacrolett.7b00148.

50. C. Lu, C. Long, Y. Li, Z. Li, and H. Zhu, *Journal of Membrane Science*, **598**, 117797 (2020) https://linkinghub.elsevier.com/retrieve/pii/S0376738819332375.

51. A. L. Ong, S. Saad, R. Lan, R. J. Goodfellow, and S. Tao, *Journal of Power Sources*, **196**, 8272–8279 (2011) https://linkinghub.elsevier.com/retrieve/pii/S037877531101127X.

52. S. Gottesfeld et al., *Journal of Power Sources*, **375**, 170–184 (2018) https://linkinghub.elsevier.com/retrieve/pii/S0378775317310340.

53. R. Abbasi et al., *Current Opinion in Electrochemistry*, **21**, 335–344 (2020) https://linkinghub.elsevier.com/retrieve/pii/S2451910320300764.

54. A. Serov, I. V. Zenyuk, C. G. Arges, and M. Chatenet, *Journal of Power Sources*, **375**, 149–157 (2018) https://linkinghub.elsevier.com/retrieve/pii/S0378775317312958.

55. J. Wang et al., *Nat Energy*, **4**, 392–398 (2019) https://www.nature.com/articles/s41560-019-0372-8.

56. J. Yang et al., *ACS Appl. Mater. Interfaces*, **7**, 28701–28707 (2015) https://pubs.acs.org/doi/10.1021/acsami.5b11122.

57. M. Singh, D. Zappa, and E. Comini, *Mater. Adv.*, **3**, 5922–5929 (2022) https://xlink.rsc.org/?DOI=D2MA00317A.

58. F. Yu et al., *International Journal of Hydrogen Energy*, **46**, 4283–4300 (2021) https://linkinghub.elsevier.com/retrieve/pii/S0360319920341574.

59. D. Papurello, D. Canuto, and M. Santarelli, *International Journal of Hydrogen Energy*, **47**, 6860–6872 (2022) https://linkinghub.elsevier.com/retrieve/pii/S0360319921047145.

60. B. Talbi, *Renewable and Sustainable Energy Reviews*, **69**, 232–238 (2017) https://linkinghub.elsevier.com/retrieve/pii/S1364032116309583.

61. J. O. Abe, A. P. I. Popoola, E. Ajenifuja, and O. M. Popoola, *International Journal of Hydrogen Energy*, **44**, 15072–15086 (2019) https://linkinghub.elsevier.com/retrieve/pii/S036031991931465X.

62. Z. Wan, Y. Tao, J. Shao, Y. Zhang, and H. You, *Energy Conversion and Management*, **228**, 113729 (2021) https://linkinghub.elsevier.com/retrieve/pii/S019689042031253X.

63. M. Kothari, L. G. Kulkarni, D. Gupta, and R. Thombre, in *Advances in Environmental Engineering and Green Technologies*, A. B. Gunjal, R. Thombre, and J. A. Parray, Editors, p. 286–307, IGI Global (2022) http://services.igi-global.com/resolvedoi/resolve.aspx?doi=10.4018/978-1-7998-9144-4.ch014.

64. R. H. Dolan, J. E. Anderson, and T. J. Wallington, *Sustainable Energy Fuels*, **5**, 4830–4841 (2021) https://xlink.rsc.org/?DOI=D1SE00979F.

65. A. Boero, A. Mercier, C. Mounaïm-Rousselle, A. Valera-Medina, and A. D. Ramirez, *Journal of Cleaner Production*, **390**, 136150 (2023) https://linkinghub.elsevier.com/retrieve/pii/S0959652623003086.

66. M. Qin, H. Molitor, B. Brazil, J. T. Novak, and Z. He, *Bioresource Technology*, **200**, 485–492 (2016) https://linkinghub.elsevier.com/retrieve/pii/S0960852415014698.

67. F. Almomani, R. Bhosale, M. Khraisheh, A. Kumar, and M. Tawalbeh, *International Journal of Hydrogen Energy*, **45**, 10398–10408 (2020) https://linkinghub.elsevier.com/retrieve/pii/S0360319919342521.

68. M. Zhang et al., *ACS Sustainable Chem. Eng.*, **8**, 12817–12824 (2020) https://pubs.acs.org/doi/10.1021/acssuschemeng.0c02926.

69. I. S. Seddiek and N. R. Ammar, *Transportation Research Part D: Transport and Environment*, **114**, 103547 (2023) https://linkinghub.elsevier.com/retrieve/pii/S136192092200373X.

70. Y. Zhang et al., *Transportation Research Part D: Transport and Environment*, **119**, 103739 (2023) https://linkinghub.elsevier.com/retrieve/pii/S1361920923001360.

71. P. Louvros, N. L. Trivyza, A. Komianos, and E. Boulougouris, *Transportation Research Procedia*, **72**, 2245–2252 (2023) https://linkinghub.elsevier.com/retrieve/pii/S2352146523010116.

72. T. Otaki and R. Shaw, *Hydrogen*, **4**, 961–974 (2023) https://www.mdpi.com/2673-4141/4/4/56.

73. https://afdc.energy.gov/fuels/prices.html.

74. https://afdc.energy.gov/fuels/properties.

75. G. Wang, C. Chen, B. A. Beshiwork, and B. Lin, *Applications in Energy and Combustion Science*, **16**, 100214 (2023) https://linkinghub.elsevier.com/retrieve/pii/S2666352X23001036.

76. S. Joseph Sekhar, M. S. Samuel, G. Glivin, T. Le, and T. Mathimani, *Fuel*, **360**, 130626 (2024) https://linkinghub.elsevier.com/retrieve/pii/S0016236123032404.

77. N. D. Pawar et al., *International Journal of Hydrogen Energy*, **46**, 27247–27267 (2021) https://linkinghub.elsevier.com/retrieve/pii/S0360319921020826.

78. S. C. Singhal and K. Kendall, *High-temperature Solid Oxide Fuel Cells: Fundamentals, Design and Applications*, p. 423, Elsevier, (2003).

79. Y. T. Hung and S. S. Shy, *International Journal of Hydrogen Energy*, **45**, 27597–27610 (2020) https://linkinghub.elsevier.com/retrieve/pii/S0360319920325982.

80. G. Cinti, L. Barelli, and G. Bidini, in, p. 020048, Erode, India (2019) https://pubs.aip.org/aip/acp/article/1007432.

81. K. H. M. Al-Hamed and I. Dincer, *Energy Conversion and Management*, **205**, 112327 (2020) https://linkinghub.elsevier.com/retrieve/pii/S0196890419313342.

82. B. Achrai et al., *J. Electrochem. Soc.*, **167**, 134518 (2020) https://iopscience.iop.org/article/10.1149/1945-7111/abbdd1.

83. N. Yang, H. Liu, G. Zhan, and D. Li, *Journal of Cleaner Production*, **245**, 118923 (2020) https://linkinghub.elsevier.com/retrieve/pii/S095965261933793X.

84. S. A. Saadabadi, H. Patel, T. Woudstra, and P. V. Aravind, *Fuel Cells*, **20**, 143–157 (2020) https://onlinelibrary.wiley.com/doi/10.1002/fuce.201900143.

Tuning Nitrogen Content in ZIF 67 Derived Porous Carbon for Efficient Room-Temperature Hydrogen Storage

Dhanya A R[1], Sana Fathima T K[1], Sundara Ramaprabhu[1]*

[1]*Alternative Energy Nanotechnology Laboratory (AENL), Department of Physics, Indian Institute of Technology Madras, Chennai 600036, Tamil Nadu, India*

** Corresponding author Email: ramp@iitm.ac.in*

Abstract

Hydrogen is considered a promising alternative to fossil fuels, but its storage challenges impede its widespread adoption. Researchers are exploring various porous materials, including metal-organic frameworks (MOFs), to develop effective hydrogen storage solutions at room temperature and reasonable pressures. Materials derived from MOFs can be tuned for desirable properties like high surface area, permanent porosity, and high thermal and chemical stability, making them excellent hosts for hydrogen molecules. Here, a mixture of ZIF 67 and different compositions of melamine is carbonized at a high temperature (800°C) to obtain ZIF 67 derived Co/NC, Co/NC-0.3, Co/NC-0.5 and Co/NC-1. Phase, morphology, and composition are confirmed through various characterizations. The hydrogen storage studies are conducted within the temperature range of 25-100°C and at pressures 5-18 bar. Co/NC-0.5 is observed to have the hydrogen storage capacity among all the samples at 16 bar, 25°C. The factors that contribute to the enhancement of hydrogen storage capacity in Co/NC-0.5 are the large surface area, defects produced on ZIF-derived structures due to uniform N doping, and the presence of Co nanoparticles (NPs) embedded in the porous support. The main mechanism involved here is the spillover and physisorption for the dissociation of the hydrogen molecules into atoms on Co NPs and its diffusion in the carbon matrix.

Keywords: *hydrogen storage, Co/NC, ZIF 67-derived, porous carbon, spillover mechanism*

1. Introduction

For a considerable amount of time, hydrogen has been considered the best alternative energy carrier that could eventually replace the use of fossil fuels. The absence of a reliable and secure storage mechanism prevents hydrogen from being used as fuel on a large scale [1]. Ongoing research has put efforts into studying hydrogen storage in different porous materials at cryogenic temperatures, whereas the major challenge is to store it at room temperature and under reasonable pressure conditions. Metal-organic frameworks (MOFs) and derived MOFs are some promising candidates that can be utilized to store hydrogen under these conditions [2-6].

By carefully selecting metal clusters and organic ligands, metal-organic frameworks (MOFs) with high specific surface area (SSA), high porosity, high thermal and chemical stability, abundant active sites, and long-range organized crystalline structure can be formed. Because of these characteristics, MOF is a promising host for several functional guest molecules, such as metal oxide or noble metal nanoparticles [3,7-8]. The MOF composites have been studied in applications that include hydrogen adsorption, carbon dioxide (CO_2) sequestration, heterogeneous catalysis, carbon dioxide conversion, etc, wherein properties such as high Specific Surface Area (SSA), dispersion in nanoparticles (NPs) and potential active surface functionalities properties are utilized. It is also reported that MOFs can be used as standard supports for noble metal NP doping in microporous/channel-like structures or MOF metal clusters, improving their heterogeneous catalytic ability [2,9].

Maintaining MOF purity for metal doping in an aqueous environment is difficult because metal NPs may form agglomerations on MOF exterior surfaces. An alternative to noble metal is also required [10,11]. Thus, the idea of pyrolyzing MOFs to produce MOF-derived carbons (MDCs) started to take shape. These MOF-derived carbons are reported to contain metal/metal oxide nanoparticles formed from metal clusters, focusing on their preparation, structure, and applications. The advantage of MOF-derived catalysts is that they preserve the MOF precursor's high porosity, large specific surface area, and highly organized structure [12]. Zeolitic imidazolate framework (ZIF) materials, in particular, are thought to be the most promising precursors for the creation of M-N-C catalysts because they contain enough well-ordered nitrogen and metal atoms in the framework that can be utilized in hydrogen adsorption. Lu et al. observed good hydrogenation catalytic activity due to hydrogen spillover on Pd-Co active sites and nitrogen doping from 2-methylimidazole (2-mIm) ligand in the Pd-Co/ZIF-derived carbon (ZDC) [13]. Co/ZDCs are reportedly used as catalysts for hydrogenation reactions without adding noble metals [14,15].

One of the major mechanisms in hydrogen storage is the spillover mechanism, wherein hydrogen molecules get dissociated into their respective atoms, which then get weakly chemisorbed on the metal nanoparticles decorated carbon support. These dissociated atoms then diffuse towards the support via a secondary spillover effect, enabling effective hydrogenation of the catalyst. This mechanism has been reported for many MOF-based materials; for example, in Pt/NH_2MIL-125(Ti), it has been reported for photocatalytic CO_2 reduction to formate [16]. Both noble and non-noble metal nanoparticles are reportedly used as hydrogen spillover sources. So, from these metal nanoparticle catalysts where the dissociation of H_2 molecules occurs, diffuses within the porous carbon support, and these H atoms occupying the porous carbon sites with a large change in enthalpy of formation is the most desirable for the room temperature hydrogen storage. Li et al. [17] reported hydrogen storage capacity as 1 wt% for Pt on MOFs, the first MOF to be reported for hydrogen storage. Tsao et al. [18] observed that the size of the Pt cluster affects the H diffusion distance within the support, and as the size decreases, it results in a longer spillover, which leads to a larger H diffusion distance.

To deposit N-doped microporous ZDC without noble metals, we pyrolyzed ZIF 67 at higher temperatures for carbonization at a particular ramp rate. Co-aggregation can be prevented by low pyrolytic temperatures, but due to insufficient thermal energy, it will not carbonize ZIF 67. In addition to Co aggregation, porosity is drastically lost at very high ZIF pyrolysis temperatures in inert gas. The fast-ramping process circumvents ZIF decomposition and excessive catalyst size, preventing the spillover mechanism necessary to enhance hydrogen storage [4].

In this work, ZIF 67 is chosen as the material for the hydrogen storage studies. Zeolitic Imidazolate Frameworks (ZIF) is a subclass of Metal-Organic frameworks built by tetrahedral metal cations M (M = Zn or Co) and imidazolate ligands (Im). ZIF-67 (Co $(Hmim)_2$, Hmim = 2-methylimidazole) consists of cobalt ion (Co^{2+}) and 2-methylimidazolate anions and exhibits a cubic crystal symmetry with unit cell parameters of $a = b = c = 16.9589$ Å with a morphology of rhombic dodecahedron. ZIF 67 was synthesized using a slightly modified technique, reported by Fathima et al. [19]. Then, ZIF 67 and the appropriate addition of melamine were carbonized at high temperatures to synthesize Co/NC, Co/NC-0.3, Co/NC-0.5, and Co/NC-1. These samples were then characterized to investigate the phase, morphology, structure, and composition. Hydrogen storage studies were conducted, and the performance was compared for all the samples.

2. Experimental

2.1. Synthesis

A modified synthesis technique, reported by Sana et al. in previous work, was used to prepare ZIF 67. The combination of methanol and 2-methylimidazole solution (45 mmol) was added to another mixture of methanol and cobalt nitrate hexahydrate solution (5.74 mmol) under constant stirring at room temperature. An overnight stirring of the solution was kept at room temperature. It was then filtered, washed twice with methanol, and dried at 60 °C to get a purple powder labeled as ZIF67 [19]. The schematic is shown in Fig 1.

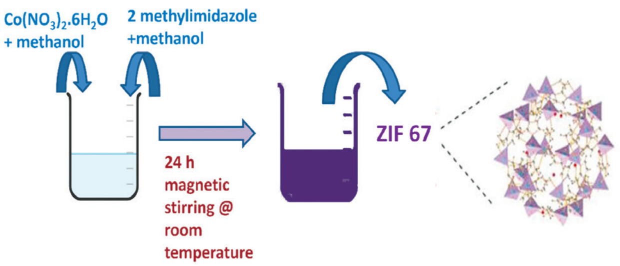

Fig. 1. Schematic of the synthesis of ZIF 67

Co/NC samples were synthesized using the pyrolysis technique. Initially, the as-synthesized ZIF 67 (mentioned in the previous paragraph) was mixed with x amount of melamine (x denotes x mmol of melamine added to 0.8 g of ZIF 67). These samples were labeled ZIF 67+0.3 mmol MEL, ZIF 67+0.5 mmol MEL, and ZIF 67+1 mmol MEL, respectively. These samples were then pyrolyzed at 800°C for 2 hrs in the nitrogen atmosphere. Then, the final samples were denoted as Co/NC-0.3, Co/NC-0.5, and Co/NC-1, respectively, where 0.3, 0.5, and 1 denote the amounts of melamine (in mmol) added to ZIF 67 before carbonization. Pure Co/NC was synthesized without adding melamine and pyrolyzing ZIF 67 at 800°C for 2 hrs in the N_2 atmosphere. A sodalite-type MOF-based structure where Co^{2+} and 2-MIM are regularly arranged is obtained in the powder form [6]. The schematic of the synthesis of derived carbon from ZIF 67 is as shown in Fig 2.

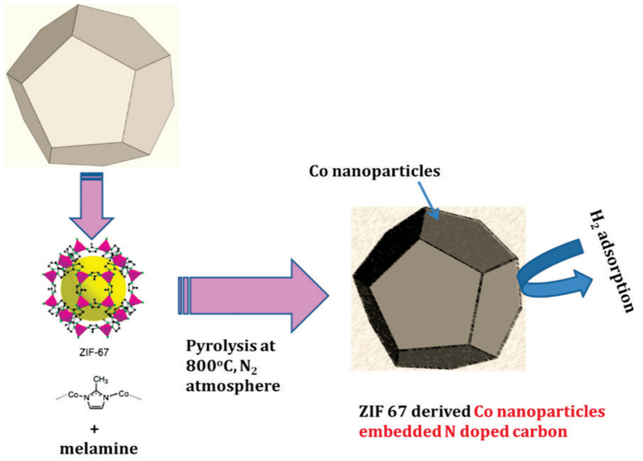

Fig. 2. Schematic of the synthesis of Co/NC, Co/NC-0.3, Co/NC-0.5, and Co/NC-1

2.2. Characterization Techniques

For X-ray diffraction (XRD) studies, a Rigaku Smartlab Diffractometer with Cu Kα radiation and nickel filter (λ=0.154nm, 40 kV, and 100mA) was used. Using TA equipment, the SDT-Q600, thermogravimetric analysis (TGA) was performed at 20°C per minute in an air atmosphere. FTIR spectra were obtained using the Agilent Technologies Cary 630 FTIR. Horiba XPLORA-MV2000 Raman spectrometer with 488 nm laser wavelength was employed to obtain the Raman spectra. Energy Dispersive X-ray Spectra (EDAX) and Field Emission Scanning Electron Microscopy (FESEM) images were measured using the Inspect F Scanning Electron Microscope (SEM). Using the Micromeritics ASAP 2020 surface area and porosity analyzer, the specific surface area (SSA), pore volume, and pore size distribution data of all the ZIF 67 derived samples were extracted. The nitrogen adsorption/desorption isotherms at 77K were used to analyze the data using the Brunauer-Emmett-Teller (BET) and Barrett-Joyner-Halanda (BJH) theories.

2.3. Hydrogen Storage Measurements

A high-pressure Sieverts apparatus was used to test the hydrogen storage capacity of the Co/NC-based samples using the volumetric technique of analysis. The number of moles of hydrogen adsorbed by the sample was determined using van der Waal equations for the real gas. Before volume calibration and degassing, a leak check procedure was performed on the system. Degassing is done at a high vacuum (10^{-6} mbar) for two hours at a temperature of roughly 200 °C following the volume calibration. After the system's temperature is adjusted to a desired level, hydrogen is then let to enter the system. For the purpose of calculating the number of moles of hydrogen interacting with the sample, the initial and equilibrium pressures are recorded. To prevent any errors in the pressure readings that can be caused by changes in the ambient temperature conditions, room temperature is maintained at 24±1°C values throughout the experiment.

3. Results and Discussions

The XRD pattern of as-synthesized ZIF 67 particles, as shown in Fig 3 (a), matches well with the reported XRD pattern of ZIF 67.[20] In Fig 1(b), the patterns of Co/NC, Co/NC-0.3, Co/NC-0.5, and Co/NC-1 samples, which are derived from different compositions of melamine along with ZIF 67, match the pattern of Co that has an fcc phase. The XRD peaks of all the samples in Fig 1(b) at 44.3°, 51.6°, and 75.9° correspond to (111), (200), and (220) of the Co nanoparticles embedded within the ZIF 67-derived nitrogen-doped porous carbon [14]. The very low intensity of the Co peaks and no obvious peaks of graphitized carbon are observed, which indicates low crystallization of Co_3O_4 and amorphous carbon. The formation of Co_3O_4 is reported at high pyrolysis temperature of ZIF 67-based material (800˚C and above) due to the crystallization of amorphous Co_3O_4. Here, since we do not observe the peaks of Co_3O_4 in all the samples pyrolyzed at 800˚C, this indicates a low crystallization of amorphous Co_3O_4 that leads to the formation of Co nanoparticles within the carbon matrix.

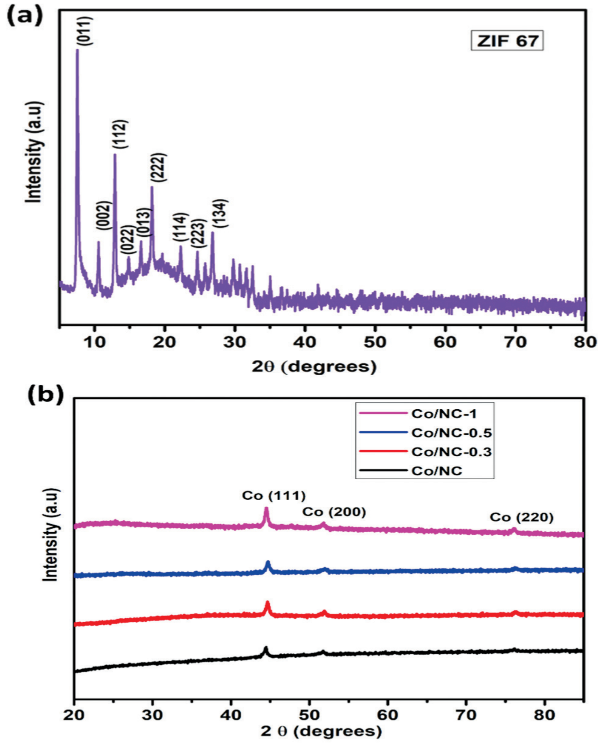

Fig. 3. XRD of (a) ZIF 67 before pyrolysis (b) ZIF 67 and melamine derived Co/NC, Co/NC-0.3, Co/NC-0.5, and Co/NC-1

In the Raman spectra, as shown in Fig 4, Co/NC, Co/NC-0.3, Co/NC-0.5, and Co/NC-1 exhibited two well-defined peaks approximately at 1327-1350 cm^{-1} and 1580-1600 cm^{-1} that belongs to the D and G bands of the graphitic carbon. This confirms the presence of carbon in all the ZIF 67-derived Co/NC samples. The ratio of I_D to I_G shows the degree of structural disorder in carbon-based nanocomposites. The higher the I_D/I_G value, the lower the graphitization of the sample and the higher the presence of the defects [21]. As seen from Fig 4, the I_D/I_G value is higher for Co/NC-0.5 when compared with other samples; thus, it has more structural defects. Adding melamine to the ZIF 67 creates more defects at higher annealing temperatures (800˚C). The defects come from the N atoms within the sample, which are contributed by the decomposition of melamine. Although a higher amount of melamine is used to prepare the Co/NC-1 sample, Co/NC-0.5 shows the optimum number of defects necessary to disperse a higher number of Co nanoparticles within the carbon matrix without the loss of dodecahedron structure of ZIF 67-based material. For Co/NC-1, we observe the distortion of the sodalite cage structure of ZIF 67 particles (as seen from the SEM images), although more N atoms are present, which can lead to the agglomeration of these Co nanoparticles and reduced surface area of the carbon support.

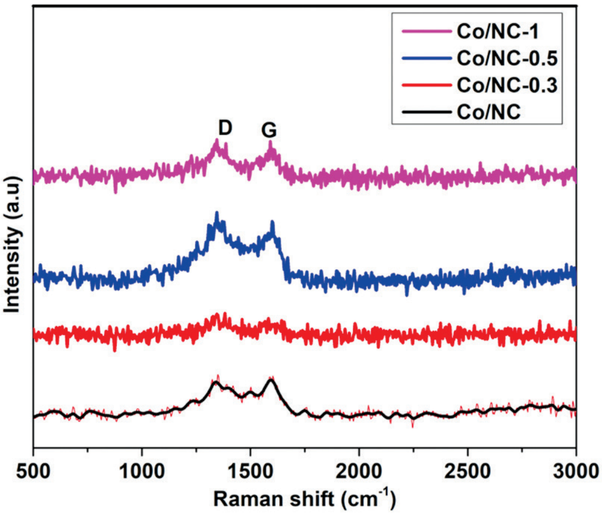

Fig. 4. Raman spectra of Co/NC, Co/NC-0.3, Co/NC-0.5 and Co/NC-1

ZIF 67 before pyrolysis, along with different compositions of melamine, has many IR peaks within the range 600-1700 cm^{-1}, as shown in Fig 5 (a). These peaks indicate the presence of ZIF 67, and the presence of melamine is also indicated by the C-N bond peaks, as seen in Fig 5(a). The absorption peaks at 1500-600 cm^{-1} are the characteristic peaks of the imidazole ring and the peak at 1578 cm^{-1} is ascribed to the stretching mode of C-N in imidazole. The IR peaks at 3100 cm^{-1} and 2900 cm^{-1} indicate the C-H stretching vibrations in the methyl group and imidazole ring [22]. The peaks that indicate the stretching vibration and out-of-plane bending modes of the C-N bond are present only in the ZIF 67 samples containing melamine at ~1600 cm^{-1} and 800 cm^{-1} [23]. When ZIF 67 is pyrolyzed at 800 °C, all the characteristic peaks of ZIF 67 disappear in all the samples. The ZIF 67 derived Co/NC, Co/NC-0.3, Co/NC-0.5, and Co/NC-1 exhibit IR peaks at 1600 cm^{-1}, which is attributed to the vibration of the graphitic carbon, as seen in Fig 5(b). The peaks observed at 1900 cm^{-1}, 2000 cm^{-1} and 2200 cm^{-1} belong to -C≡C-, as seen in Fig 5(b) are originating from the diamond crystal used in the FTIR instrument [24].

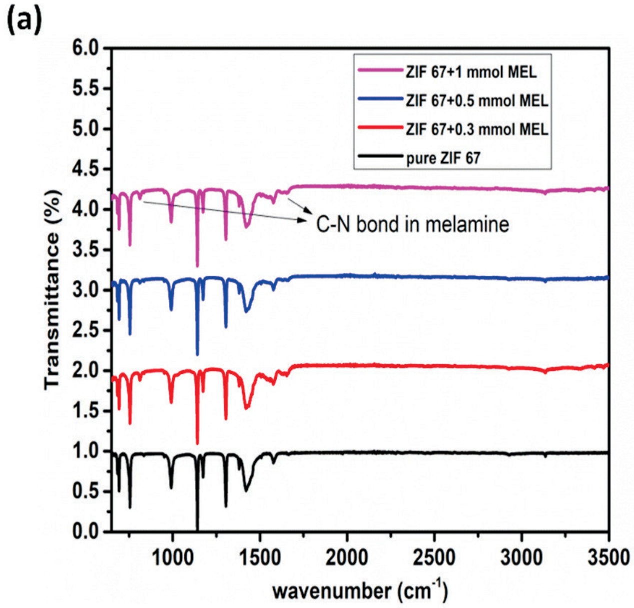

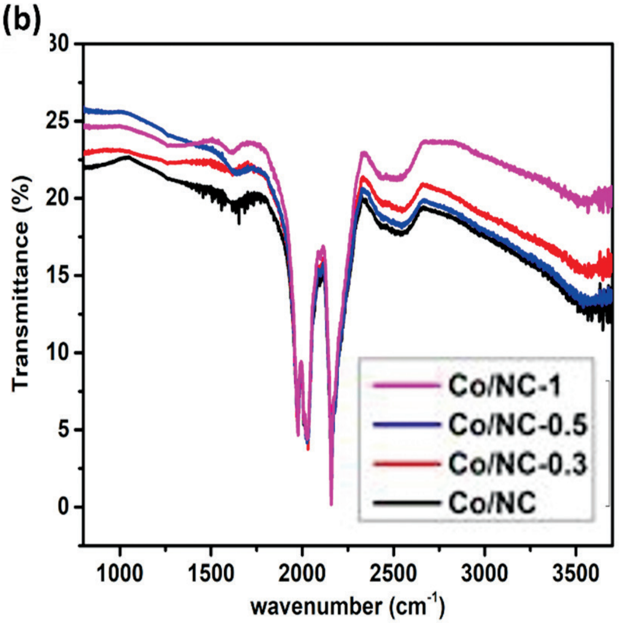

Fig. 5. FTIR of (a) ZIF 67, ZIF67+0.3 mmol MEL, ZIF67+0.5 mmol MEL and ZIF67+1 mmol MEL (b) Co/NC, Co/NC-0.3, Co/NC-0.5 and Co/NC-1

Thermogravimetric analysis was performed for ZIF 67, ZIF 67+0.3 mmol MEL, ZIF 67+0.5 mmol MEL, and ZIF67+1 mmol MEL in a nitrogen atmosphere from room temperature to 1000°C at a rate of 20°C/min, as shown in Fig 6. The graph shows two peaks that indicate weight loss, one between 200°C and 400°C and the other between 400°C and 600°C. The adsorption of the water molecules on the surface causes weight loss, which is observed at 250-300°C for melamine-added ZIF 67 samples. The decomposition of melamine starts at 300°C and is decomposed completely above 400°C [6]. The decomposition temperature of the samples reduces with the presence of melamine, indicating that adding melamine to ZIF 67 could accelerate the decomposition of ZIF 67 [4,6]. The weight loss of ZIF 67+0.5 mmol MEL and ZIF 67 is lower than that of ZIF 67+0.3 mmol MEL and ZIF 67+1 mmol MEL, indicating that the interaction between melamine and ZIF 67 is more in ZIF 67+0.5 mmol MEL. The weight percent of Co is observed to be the highest for ZIF 67+0.5 mmol MEL (~27 wt%).

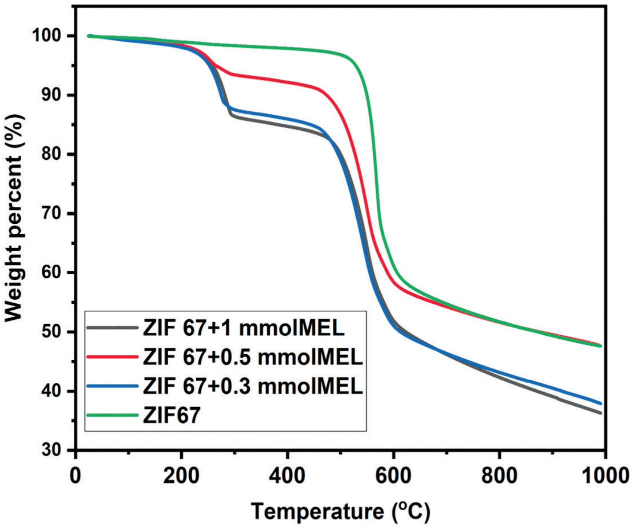

Fig. 6. TGA of ZIF 67, ZIF 67+0.3 mmol MEL, ZIF 67+0.5 mmol MEL, and ZIF 67+1 mmol MEL

It is observed from Fig 7 that after pyrolysis of ZIF 67 to 800°C, in SEM images, the ZIF particles with sodalite cage pore structure or rhombic-dodecahedron structure are distorted, and the surfaces are rough**.** For the samples Co/NC-0.3 and Co/NC-0.5, the growth of small carbon nanotubes is observed at the distorted edges of the particles. When melamine is 1mmol, more round particles can be seen embedded in the matrix where the surface has become rougher, and there is a complete distortion of the sodalite cage structure of ZIF 67 particles at the same annealing temperature in the Co/NC-1 sample [25]. Table [S1-S4] shows the EDAX spectra and elemental composition of Co/NC, Co/NC-0.3, Co/NC-0.5, and Co/NC-1. The lowest nitrogen content and the highest Co content are observed for the Co/NC-0.5 sample, as seen in Table S4. This confirms that the interaction between melamine and ZIF 67 is greater in ZIF 67+0.5 mmol MEL, as indicated by the TGA results since the content of Co is highest in this sample. Co/NC-0.5 also shows less distortion of the edges of the structure (Fig 7(c)) and thus maximizes the uniform distribution of Co nanoparticles within it.

The presence of amorphous carbon is seen in SEM images (Fig 7 [a-d]) for all the Co/NC samples but the amount is less due to less amount of melamine taken in comparison with the ZIF 67. For all the ZIF 67 derived samples, we observe a quite large surface area, as seen from BET isotherm graphs (Fig 8 (a)). The largest surface area is observed for Co/NC-0.5, which indicates that it can accommodate more hydrogen atoms that get diffused within the carbon after the dissociation of hydrogen molecules due to its interaction with the Co nanoparticles via the spillover effect.

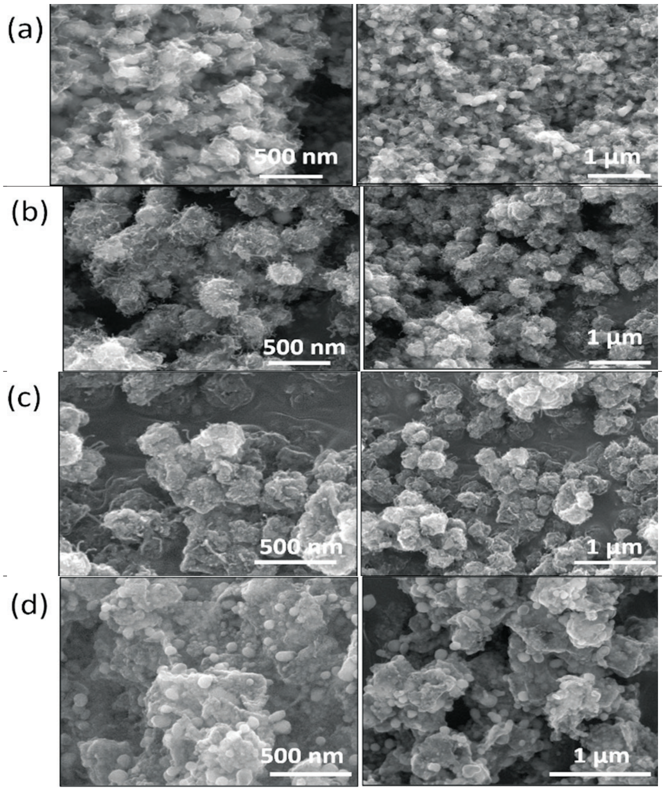

Fig .7. SEM of (a) ZIF 67 (b) Co/NC-0.3 (c) Co/NC-0.5 (d) Co/NC-1

The BET isotherms and pore size distribution plots for the samples Co/NC, Co/NC-0.3, Co/NC-0.5, and Co/NC-1 are shown in Fig 8 (a) and (b). Type IV isotherm is observed for all the samples, as seen in Fig 8 (a), which is characteristic of mesopores. The highest specific surface area (372.6900 m^2/g) and pore volume (0.4290 cm^3/g) are observed for Co/NC-0.5. In the pore size distribution plots, as shown in Fig 8 (b), the pore diameter peak is observed at less than 5 nm for Co/NC, Co/NC-0.3, and Co/NC-0.5, but above 2 nm, which indicates the presence of mesopores within the carbon matrix in these samples [26]. For Co/NC-1, it is observed that the pore diameter is the highest among all, indicating the presence of macropores and mesopores. Co/NC has the highest SSA and pore volume and the lowest pore width/diameter, so the presence of active sites for the physisorption of hydrogen molecules will be the highest among all samples. Table 1 shows all the BET parameters that show SSA, pore volume, and pore diameter of all samples.

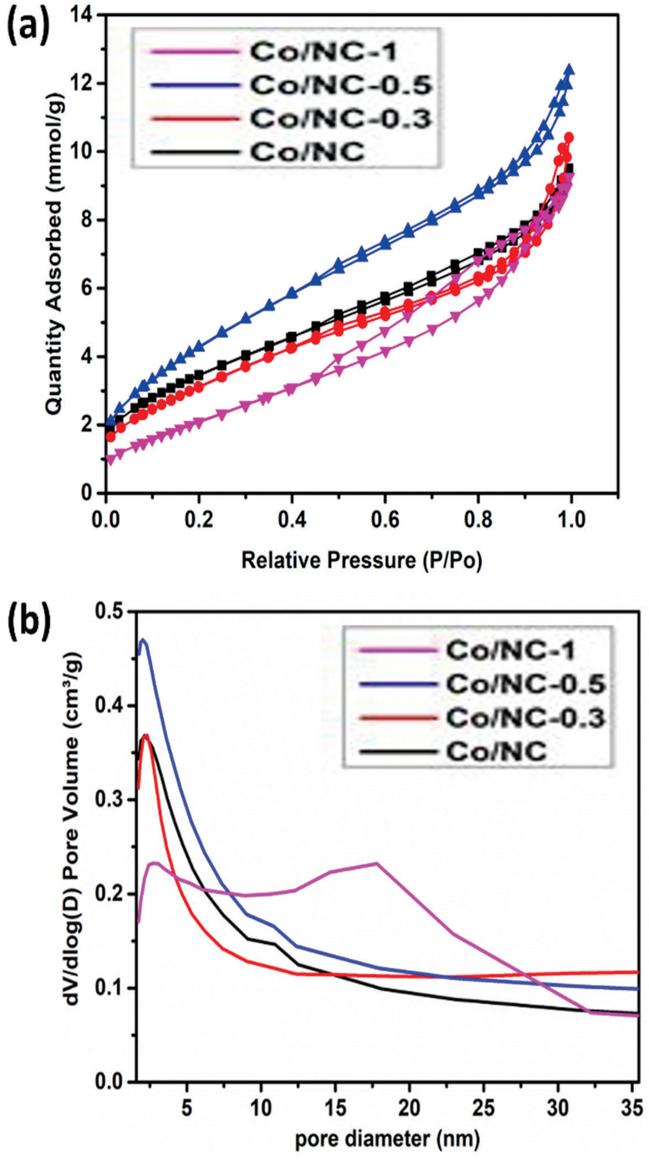

Fig. 8 (a) BET isotherms and (b) pore size distribution plot of Co/NC, Co/NC-0.3, Co/NC-0.5, and Co/NC-1

Table 1 BET parameters SSA, pore volume, and pore diameter of Co/NC, Co/NC-0.3, Co/NC-0.5, and Co/NC-1

S N	Sample	SSA (m^2/g)	Pore volume (cm^3/g)	Pore diameter (nm)
1.	Co/NC	289.0686	0.329866	4.56453
2.	Co/NC-0.3	268.9454	0.360945	5.36830
3.	Co/NC-0.5	372.6900	0.429009	4.60446
4.	Co/NC-1	191.3495	0.320949	6.70918

The hydrogen adsorption properties of Co/NC, Co/NC-0.3, Co/NC-0.5, and Co/NC-1 were performed using a high-pressure Sievert's apparatus.[27]. The temperature and pressure ranges for the measurements were from 25–100°C and 5–18 bar, respectively. The pressure-composition (PC) isotherm plots for all the samples are shown in Fig 9 [a-d]. From these plots, it is depicted that the hydrogen storage capacities of Co/NC, Co/NC-0.3, Co/NC-0.5, and Co/NC-1 are 2 wt%, 0.8 wt%, 2.4wt%, and 1.3 wt% at 16 bar and 25°C, respectively. The hydrogen adsorption capacity linearly increases with the pressure at a particular temperature. This is indicative of the physisorption occurring within the carbon matrix. The maximum physisorption occurs for the material having a large surface area, which is the highest for Co/NC-0.5, according to the BET results. The interaction between melamine and ZIF 67 is more in Co/NC-0.5, according to TGA of ZIF 67+0.5 mmol MEL and EDAX of Co/NC-0.5, which results in the maximum coordination between N and C. This makes the distribution of Co nanoparticles in Co/NC-0.5 more uniform throughout the material. This enhances the hydrogen spill-over effect over these Co nanoparticles embedded within the nitrogen-doped carbon matrix. According to TGA, the weight percent of Co is high in Co/NC-0.5, which indicates that the hydrogen molecules interact with more Co nanoparticles in this case. This leads to the improvement in the storage capacity of ZIF 67-derived Co/NC-0.5. The carbon matrix alone would exhibit limited hydrogen storage capacity due to weak van der Waal's forces between hydrogen molecules and carbon atoms [28]. To augment this, various heteroatoms such as nitrogen, boron, sulfur, and phosphorous can be introduced into the carbon structure via doping [29]. Here, nitrogen doping is achieved through the mixing of melamine along with ZIF 67 before carbonization. This process alters the local electronic structure of the derived carbon matrix, potentially enhancing its hydrogen storage capabilities. The nitrogen doping in the carbon matrix causes a change in the local electronic structure of the carbon support in the Co/NC, Co/NC-0.3, Co/NC-0.5, and Co/NC-1 samples. The charge transfer between the modified electronic structure of the porous carbon matrix after the nitrogen doping and the embedded Co nanoparticles strengthens the interaction between these nanoparticles and the carbon support. This prevents the agglomeration of these Co nanoparticles over the porous carbon support and leads to uniform dispersion of nanoparticles due to the presence of nitrogen atoms. This could enhance the effective interaction of hydrogen molecules over these nanoparticles and thus improve the hydrogen storage capacity. The introduction of nitrogen atoms into carbon networks promotes charge transfer between adjacent carbon atoms, leading to improved hydrogen adsorption in porous ZIF 67-derived carbon matrix. This effect is further amplified by embedding Co metal nanoparticles, which enhances hydrogen uptake through the spillover mechanism [4, 30] Additionally, the structural defects created by nitrogen doping facilitate a more uniform distribution of Co nanoparticles within the porous carbon structure. The hydrogen storage capacity decreases in the following trend: Co/NC-0.5>Co/NC>Co/NC-1>Co/NC-0.3. The storage capacity for Co/NC-1 is reduced since there is a distortion of the sodalite cage structure of the ZIF -67 derived carbon, and there are much fewer Co nanoparticles embedded within such a support material. So, fewer hydrogen molecules will be involved in the spill-over mechanism, which leads to the degradation of the hydrogen adsorption performance. It is observed that Co/NC-0.3 also has less storage capacity compared to Co/NC, and this could be due to less coverage of nitrogen atoms within the porous sodalite cage structure of carbon matrix that is much necessary for anchoring of Co nanoparticles towards it. Co/NC-0.5 has the optimum amount of nitrogen distributed throughout the carbon surface, which is necessary for bonding Co nanoparticles on the carbon surface.

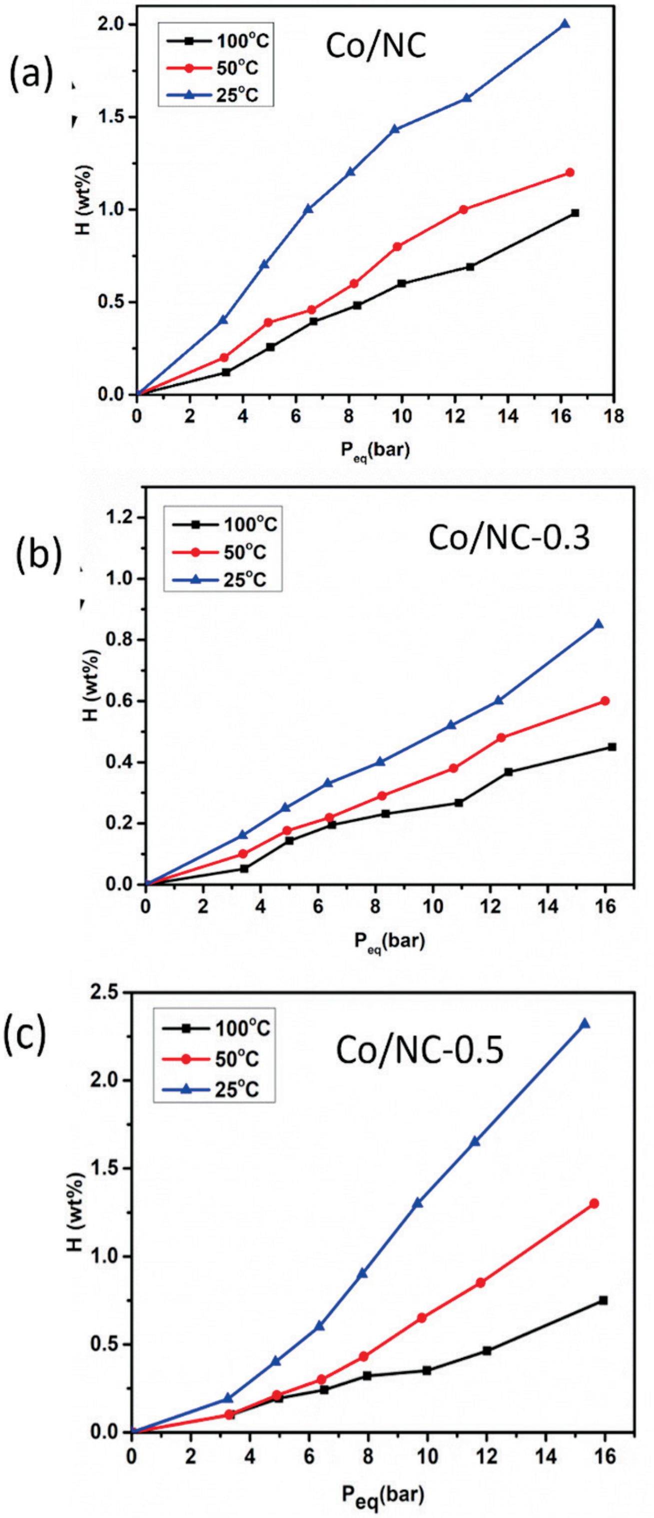

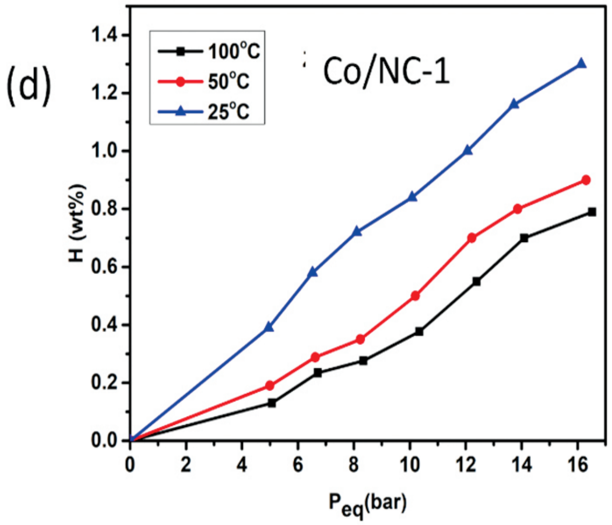

Fig. 9. PC isotherm plots of (a) Co/NC (b) Co/NC-0.3 (c) Co/NC-0.5 (d) Co/NC-1

A comparison with the other ZIF-derived carbon materials from the literature survey is shown in Table 2. A comparison of hydrogen storage performance with the other MOF-derived carbon materials

Samples	References	Pressure (bar)	Hydrogen uptake (wt%) (at 25^{o}C)
ZIF67-derived carbon-500	[4]	~16	0.6
Pt/AC + Cu-TDPAT (MOF)	[31]	~1	0.044
MOF-derived carbon	[32]	~100	0.94
Pt@ZIF-8/GO	[33]	~10	0.841 (~77K)
MOF-5_b	[34]	~16	0.15 (~15 ^{o}C)
Co/NC-0.5 (ZIF 67 derived)	**This work**	~16	2.4

The isosteric heat of adsorption (Q_{st}) is obtained from the absolute heat of enthalpy, ΔH, which is acquired from the slope of the Van't Hoff plot. This plot is drawn between ln P (P in Pa) vs 1/T (K^{-1}) and its slope gives ΔH, at a fixed hydrogen storage capacity (in wt%) of the material. The Clausius-Clapeyron equation is used to quantify the strength of the contact between the hydrogen atoms and the sample's surface atoms [35] as follows:

Where R is the ideal gas constant, P is the H_2 equilibrium pressure, T is the temperature at which the amount of hydrogen stored (in wt %) is measured.

The isosteric heat of adsorption (Q_{st}) is calculated from the above equation after obtaining the slope from the Van't Hoff plots of Co/NC, Co/NC-0.3, Co/NC-0.5, and Co/NC-1, as shown in Fig 10 (a-d). Q_{st} values for Co/NC, Co/NC-0.3, Co/NC-0.5, and Co/NC-1, at different adsorption values 0.2 wt%, 0.4 wt%, 0.6 wt%, and 0.8 wt% are shown in Table 3 below.

Any carbon-based adsorbent is said to have an enthalpy of adsorption of 4-6 kJmol^{-1}, which is extremely low to meet the requirements for hydrogen storage material at room temperature [36]. Enthalpy of adsorption equivalent to or less than 15 kJmol^{-1} is desired in materials to achieve the DOE requirement for an effective hydrogen storage material [37]. This is closely achieved by Co/NC-0.5, which shows an isosteric heat of adsorption value of 11.21 kJmol^{-1}, as seen in Table 3.

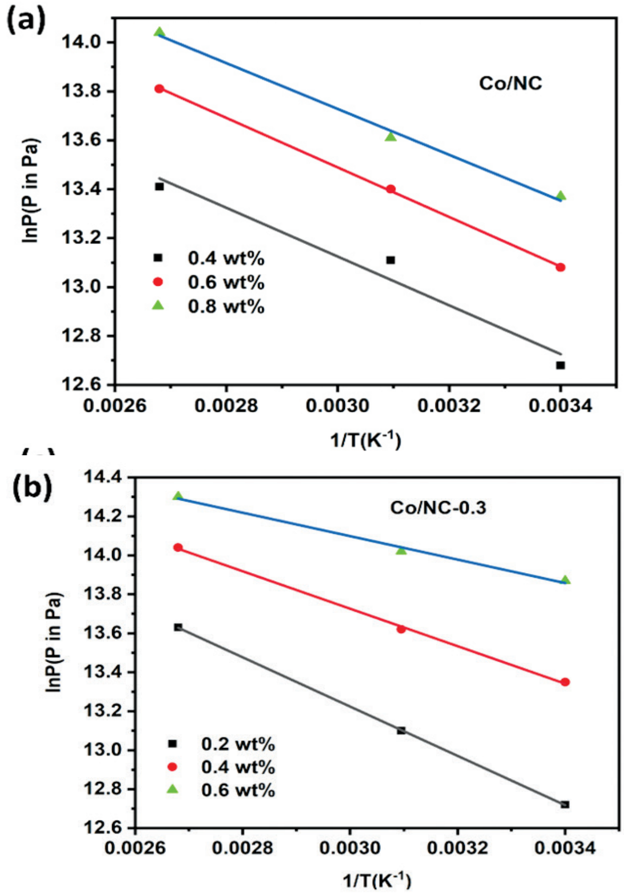

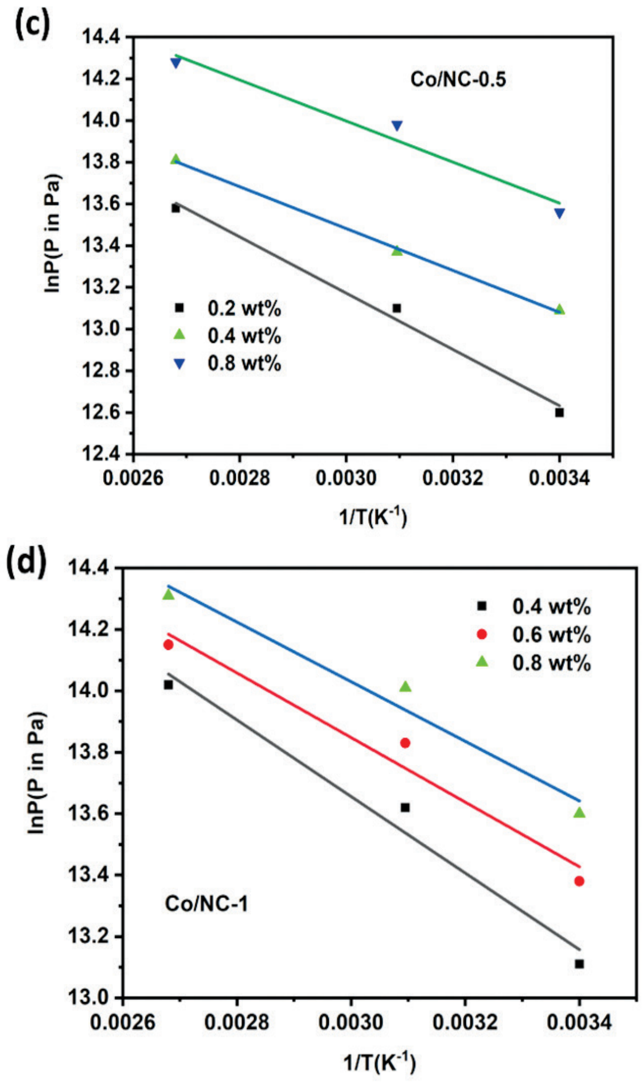

Fig 10 Van't Hoff plots of (a) Co/NC (b) Co/NC-0.3 (c) Co/NC-0.5 (d) Co/NC-1

Table -3. Comparison of Q_{st} values of Co/NC, Co/NC-0.3, Co/NC-0.5 and Co/NC-1

Sample	Q_{st} at 0.2 wt% ($kJmol^{-1}$)	Q_{st} at 0.4 wt% ($kJmol^{-1}$)	Q_{st} at 0.6 wt% ($kJmol^{-1}$)	Q_{st} at 0.8 wt% ($kJmol^{-1}$)
Co/NC	-	8.2	8.4	7.7
Co/NC-0.3	10	7.9	5	-
Co/NC-0.5	11.2	8.5	-	8.1
Co/NC-1	-	9	8.5	8

4. Conclusions

ZIF 67 was used as the source of Co/NC, Co/NC-0.3, Co/NC-0.5, and Co/NC-1, which were synthesized utilizing a straightforward, cost-effective pyrolysis synthesis method employing varying amounts of melamine. XRD was used to confirm the phases of the embedded Co nanoparticles within the nitrogen-doped porous carbon, while SEM and EDAX measurements were used to establish the structure and elemental composition. BET measurement is performed to determine each sample's specific surface area (SSA) and pore size distribution. Compared to Co/NC, Co/NC-0.3, and Co/NC-1, the hydrogen adsorption capacity of Co/NC-0.5 is higher. This is because of the complementary effects of the right concentration of nitrogen and metal embedment, which increase the number of active sites available for the H atom's adsorption through the spillover process. For effective hydrogen adsorption, the addition of 0.5 mmol of melamine results in a homogeneous dispersion of metal nanoparticles in the carbon matrix and strengthens the metal-nitrogen-carbon link. Every sample's ability to store hydrogen follows this general pattern: Co/NC-0.5>Co/NC>Co/NC-1>Co/NC-0.3 in the 25–100°C temperature range and 5–16 bar pressure range. This paper reports the maximum hydrogen storage capacity for Co/NC-0.5 at room temperature and at an H_2 equilibrium pressure of around 16 bar, which is 2.45 wt%. Additionally, Co/NC-0.5 exhibits the greatest Qst value (11.2 $kJmol^{-1}$), which is quite near to the targeted DOE value of 15 $kJmol^{-1}$. Out of all the several kinds of ZIF-derived carbon, this has the largest hydrogen storage capacity at room temperature. The significant increase in modified porous carbon's storage capacity, while still far short of the US DOE target of 6wt% hydrogen storage capacity, opens the door for the development of hydrogen storage adsorption systems, ideally at ambient conditions.

Acknowledgments

The authors wish to thank MHRD, Govt. of India, Department of Science and Technology (DST) for the financial support.

References

[1] L. Schlapbach et A. Züttel, Hydrogen-storage materials for mobile applications, vol. 414, 2001, [En ligne]. Disponible à: www.nature.com

[2] S. J. Yang *et al.*, MOF-derived hierarchically porous carbon with exceptional porosity and hydrogen storage capacity, *Chemistry of Materials*, vol. 24, nº 3, p. 464-470, févr. 2012, doi: 10.1021/cm202554j.

[3] H. Furukawa, K. E. Cordova, M. O'Keeffe, et O. M. Yaghi, « The chemistry and applications of metal-organic frameworks, *Science*, vol. 341, nº 6149. American Association for the Advancement of Science, 2013. doi: 10.1126/science.1230444.

[4] P. Sen Tseng *et al.*, ZIF-67 derived Co nanoparticles on ZIF-Derived carbon for hydrogen spillover and storage, *Appl Surf Sci*, vol. 638, nov. 2023, doi: 10.1016/j.apsusc.2023.158097.

[5] H. Reardon, J. M. Hanlon, R. W. Hughes, A. Godula-Jopek, T. K. Mandal, et D. H. Gregory, Emerging concepts in solid-state hydrogen storage: The role of nanomaterials design, *Energy and Environmental Science*, vol. 5, nº 3. p. 5951-5979, mars 2012. doi: 10.1039/c2ee03138h.

[6] Q. Wang *et al.*, Highly active cobalt- and nitrogen-doped carbon derived from ZIF-67@melamine towards oxygen reduction reaction, *Journal of Electroanalytical Chemistry*, vol. 894, août 2021, doi: 10.1016/j.jelechem.2021.115397.

[7] B. Liu, H. Shioyama, T. Akita, et Q. Xu, Metal-organic framework as a template for porous carbon synthesis, *J Am Chem Soc*, vol. 130, nº 16, p. 5390-5391, avr. 2008, doi: 10.1021/ja7106146.

[8] M. Kim *et al.*, MOF-derived nanoporous carbons with diverse tunable nanoarchitectures, *Nat Protoc*, vol. 17, nº 12, p. 2990-3027, déc. 2022, doi: 10.1038/s41596-022-00718-2.

[9] A. Nuhnen et C. Janiak, A practical guide to calculate the isosteric heat/enthalpy of adsorption: Via adsorption isotherms in metal-organic frameworks, MOFs, *Dalton Transactions*, vol. 49, nº 30. Royal Society of Chemistry, p. 10295-10307, 14 août 2020. doi: 10.1039/d0dt01784a.

[10] V. F. Yusuf, N. I. Malek, et S. K. Kailasa, Review on Metal-Organic Framework Classification, Synthetic Approaches, and Influencing Factors: Applications in Energy, Drug Delivery, and Wastewater Treatment, *ACS Omega*, vol. 7, nº 49. American Chemical Society, p. 44507-44531, 13 décembre 2022. doi: 10.1021/acsomega.2c05310.

[11] F. Zheng *et al.*, Review: Synthesis and Catalytic Application of MOF Complexes Containing Noble Metals, *Energy and Fuels*. American Chemical Society, 2024. doi: 10.1021/acs.energyfuels.4c01963.

[12] H. Konnerth, B. M. Matsagar, S. S. Chen, M. H. G. Prechtl, F. K. Shieh, et K. C. W. Wu, Metal-organic framework (MOF)-derived catalysts for fine chemical production, *Coordination Chemistry Reviews*, vol. 416. Elsevier B.V., 1 août 2020. doi: 10.1016/j.ccr.2020.213319.

[13] S. Lu *et al.*, Hydrogenation of furfural over Pd@ZIF-67 derived catalysts: direct hydrogenation and transfer hydrogenation, *New Journal of Chemistry*, vol. 46, nº 28, p. 13715-13724, juin 2022, doi: 10.1039/d2nj01565j.

[14] K. Murugesan *et al.*, Cobalt-based nanoparticles prepared from MOF-carbon templates as efficient hydrogenation catalysts, *Chem Sci*, vol. 9, nº 45, p. 8553-8560, 2018, doi: 10.1039/c8sc02807a.

[15] S. Yang *et al.*, MOF-Derived Cobalt Phosphide/Carbon Nanocubes for Selective Hydrogenation of Nitroarenes to Anilines, *Chemistry - A European Journal*, vol. 24, nº 17, p. 4234-4238, mars 2018, doi: 10.1002/chem.201705400.

[16] Q. Su, Q. Guo, H. Wang, M. Liu, et C. Zuo, Research progress of MOF-based materials in the photocatalytic CO2 reduction, *Carbon Resources Conversion*, vol. 7, nº 1. KeAi Publishing Communications Ltd., 1 mars 2024. doi: 10.1016/j.crcon.2023.100211.

[17] A. Li, R. F. Lu, Y. Wang, X. Wang, K. L. Han, et W. Q. Deng, Lithium-doped conjugated microporous polymers for reversible hydrogen storage, *Angewandte Chemie - International Edition*, vol. 49, nº 19, p. 3330-3333, avr. 2010, doi: 10.1002/anie.200906936.

[18] C. S. Tsao *et al.*, « Hydrogen spillover effect of pt-doped activated carbon studied by inelastic neutron scattering », *Journal of Physical Chemistry Letters*, vol. 2, nº 18, p. 2322-2325, sept. 2011, doi: 10.1021/jz2010368.

[19] S. Fathima T.K., A. Ghosh, et S. Ramaprabhu, ZIF67-derived Co–CoO@C nanocomposites as highly efficient and selective oxygen evolution reaction (OER) catalysts for seawater electrolysis, *Int J Hydrogen Energy*, vol. 49, p. 780-793, janv. 2024, doi: 10.1016/j.ijhydene.2023.09.122.

[20] J. Qian, F. Sun, et L. Qin, Hydrothermal synthesis of zeolitic imidazolate framework-67 (ZIF-67) nanocrystals, *Mater Lett*, vol. 82, p. 220-223, sept. 2012, doi: 10.1016/j.matlet.2012.05.077.

[21] B. Weng *et al.*, Metal-Organic Framework-Derived CoWP@C Composite Nanowire Electrocatalyst for Efficient Water Splitting, *ACS Energy Lett*, vol. 3, nº 6, p. 1434-1442, juin 2018, doi: 10.1021/acsenergylett.8b00584.

[22] M. Afkhami-Ardekani, M. R. Naimi-Jamal, S. Doaee, et S. Rostamnia, Solvent-Free Mechanochemical Preparation of Metal-Organic Framework ZIF-67 Impregnated by Pt Nanoparticles for Water Purification, *Catalysts*, vol. 13, nº 1, janv. 2023, doi: 10.3390/catal13010009.

[23] Y. Xu *et al.*, (Co, Ni)-NC/CNT Composite as a Cathode for Li-S Batteries, *ACS Appl Nano Mater*, vol. 7, nº 9, p. 10520-10531, mai 2024, doi: 10.1021/acsanm.4c00955.

[24] A. R. Dhanya, P. Haridoss, et R. Sundara, EDA/PANI derived FeNxC with Fe-Nx active sites as room temperature hydrogen storage material, *J Alloys Compd*, vol. 970, janv. 2024, doi: 10.1016/j.jallcom.2023.172596.

[25] R. Das, P. Pachfule, R. Banerjee, et P. Poddar, Metal and metal oxide nanoparticle synthesis from metal organic frameworks (MOFs): Finding the border of metal and metal oxides, *Nanoscale*, vol. 4, nº 2, p. 591-599, janv. 2012, doi: 10.1039/c1nr10944h.

[26] A. R. Dhanya, N. Ranjan, et S. Ramaprabhu, Hydrogen storage studies of Co, Fe, Fe3C nanoparticles encapsulated nitrogen doped carbon nanotubes, *Energy Storage*, vol. 5, nº 4, juin 2023, doi: 10.1002/est2.421.

[27] S. S. Samantaray, V. Sangeetha, S. Abinaya, et S. Ramaprabhu, Diatom frustule-graphene based nanomaterial for room temperature hydrogen storage, *Int J Hydrogen Energy*, vol. 45, nº 1, p. 764-773, janv. 2020, doi: 10.1016/j.ijhydene.2019.10.155.

[28] A. Gupta *et al.*, Hydrogen Clathrates: Next Generation Hydrogen Storage Materials, *Energy Storage Materials*, vol. 41. Elsevier B.V., p. 69-107, 1 octobre 2021. doi: 10.1016/j.ensm.2021.05.044.

[29] Y. Xia, G. S. Walker, D. M. Grant, et R. Mokaya, Hydrogen storage in high surface area carbons: Experimental demonstration of the effects of nitrogen doping, *J Am Chem Soc*, vol. 131, nº 45, p. 16493-16499, 2009, doi: 10.1021/ja9054838.

[30] A. P. Pandey, M. A. Shaz, V. Sekkar, et R. S. Tiwari, Synergistic effect of CNT bridge formation and spillover mechanism on enhanced hydrogen storage by iron doped carbon aerogel, *Int J Hydrogen Energy*, vol. 48, nº 56, p. 21395-21403, juill. 2023, doi: 10.1016/j.ijhydene.2022.02.076.

[31] C. Y. Wang *et al.*, Hydrogen storage with spectroscopic identification of chemisorption sites in Cu-TDPAT via spillover from a Pt/activated carbon catalyst, *Journal of Physical Chemistry C*, vol. 118, nº 46, p. 26750-26763, nov. 2014, doi: 10.1021/jp507395p.

[32] S. J. Yang *et al.*, MOF-derived hierarchically porous carbon with exceptional porosity and hydrogen storage capacity, *Chemistry of Materials*, vol. 24, n° 3, p. 464-470, févr. 2012, doi: 10.1021/cm202554j.

[33] H. Zhou, J. Zhang, D. Ji, A. Yuan, et X. Shen, Effect of catalyst loading on hydrogen storage capacity of ZIF-8/graphene oxide doped with Pt or Pd via spillover, *Microporous and Mesoporous Materials*, vol. 229, p. 68-75, juill. 2016, doi: 10.1016/j.micromeso.2016.04.007.

[34] S. M. Luzan et A. V. Talyzin, Hydrogen adsorption in Pt catalyst/MOF-5 materials, *Microporous and Mesoporous Materials*, vol. 135, n° 1-3, p. 201-205, 2010, doi: 10.1016/j.micromeso.2010.07.018.

[35] Q. R. Zheng, S. Gao, et C. J, Determination of the isosteric heat of adsorption of hydrogen on the Multi-Walled Carbon Nanotubes, dans *Advanced Materials Research*, 2012, p. 1484-1491. doi: 10.4028/www.scientific.net/AMR.512-515.1484.

[36] E. W. Knight *et al.*, Determination of the Enthalpy of Adsorption of Hydrogen in Activated Carbon at Room Temperature, 2020. [En ligne]. Disponible à: https://www.elsevier.com/open-access/userlicense/1.0/

[37] S. S. Samantaray, V. Sangeetha, S. Abinaya, et S. Ramaprabhu, Enhanced hydrogen storage performance in Pd3Co decorated nitrogen/boron doped graphene composites, *Int J Hydrogen Energy*, vol. 43, n° 16, p. 8018-8025, avr. 2018, doi: 10.1016/j.ijhydene.2018.03.078.

Evolution of Secondary Marigold Flower Waste as Electrode for Zinc-Based Hybrid Supercapacitor

[a] Sayli Pradhan, [b]Umer Khan, [b]Jyotsna T. Waghmare, [*a] Neetu Jha
nan19.sr.pradhan@pg.ictmumbai.edu.in
nr.jha@ictmumbai.edu.in
[*a] Department of Physics, Institute of Chemical Technology, Mumbai 400019, India
[b] Department of Oils, Oleochemicals and Surfactants, Institute of Chemical Technology, Mumbai, 400019, India

Abstract:

In this study, secondary marigold flowers waste (SMW) was successfully converted into porous carbons through hydrothermal carbonization (HTC) followed by pyrolysis. The high-temperature pyrolysis led to the complete removal of functional groups due to dehydration and decarboxylation processes. The resulting hierarchical porous carbon material (HPCM), when employed as the positive electrode in a zinc-ion hybrid supercapacitor (ZBHSC), exhibited a specific capacity of 157.44 mAh g^{-1} at a current density of 0.3 A g^{-1}. The ZBHSC incorporating HPCM as the positive electrode maintained a capacity retention of 71.57% and a coulombic efficiency of 90.17% over 200 cycles. The developed ZBHSC achieved an impressive balance between energy and power, with a peak energy density of 56 Wh kg^{-1} at 106 W kg^{-1} and a high-power density of 1.07 kW kg^{-1} at 4.18 Wh kg^{-1}. These results underscore the potential of HPCM derived from SMW as a versatile material for advanced energy storage applications.

Keywords: *Marigold flower, secondary waste material, hydrothermal carbonization, Zinc based hybrid supercapacitor, hydrothermally carbonized Marigold, and hydro-pyro-carbonization of Marigold.*

---

1. Introduction

Fossil fuel consumption causes air pollution and contributes to global warming. Fossil fuel distribution and extraction also have an impact on the environment and add to the cost of protecting a country against local fossil fuel shortages[1]. Modern electric vehicle technology and large-scale grid energy storage, among other things, have made the need for sophisticated energy storage systems that are highly effective, affordable, and environmentally benign more pressing [2-4]. Batteries and supercapacitors, which are now used for commercial energy storage, can't accommodate all of the needs for energy storage in the future. Applications for lithium-ion batteries (LIBs) are hampered by their low power density, scarcity of lithium resource materials, poor cycling stability, and safety [5]. Moreover, the low energy density of supercapacitors prevents their use in many applications [6] . The development of new electrochemical hybrid supercapacitors, which combine the benefits of batteries and supercapacitors, has drawn significant interest and become an important research topic in the field of energy storage [6-11].

Several metal-ion hybrid supercapacitors, including Li, Na, and Zn, have drawn a lot of attention in recent years. Zinc based hybrid supercapacitors (ZBHSC), which consist of one electrode that is similar to a battery (Zn) and one electrode that is similar to a capacitor (carbon based). In aqueous system, the Zn metal can easily strip or plate charge-carrying cations when used as an anode[12]. In fact, the development of improved metal-ion hybrid supercapacitors depends heavily on this design approach[13]. In mild neutral electrolytes as $ZnSO_4$, the Zn-ion hybrid supercapacitor exhibits a number of noteworthy benefits, including good safety, an ample Zn resource, low cost, and a chemically inert, low toxicity [14,15]. The zinc anode has a higher theoretical capacity (5854 mA h cm^{-3} and 820 mA h g^{-1}) than the market-leading lead-acid batteries and a comparatively low redox potential (-0.76 V vs standard hydrogen electrode) [16-19]. For real-time application, the development of electrochemically efficient, low-cost, high surface area, and highly stable positive electrode is desired for ZBHSC application.

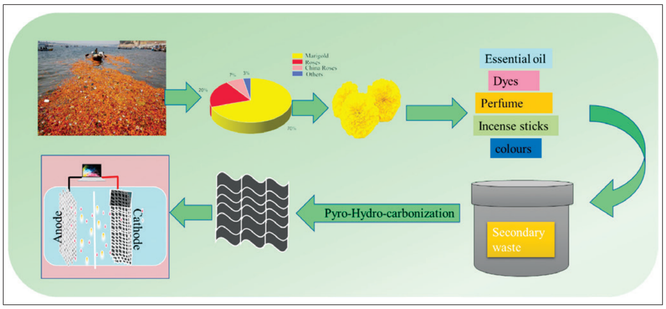

Fig. 1:Evolution of secondary Marigold waste

Marigold flowers are utilised in religious places, where they are offered to deities and used for decoration before being abandoned and becoming garbage [20]. After offering the florals to the deities, the flowers serve their purpose of worship but lose their value and are then treated as rubbish, collected with other waste before being deposited in water bodies or with other waste, polluting the environment. Marigold floral waste (MFW) has a low pH and is high in micronutrients (Fe, Mn, Zn, Cu, and so on) as well as macronutrients (N, P, K, and Ca) [21]. The nutrient richness of MFW causes eutrophication of water bodies, resulting in the extinction of aquatic fauna. This primary floral waste can be used to make a variety of small-scale goods like perfumes, essential oils, dyes, incense sticks, and colours, etc. [22]. This can be referred to as primary waste recycling. The primary recycling industries or laboratories generates residual waste after processing primary waste which termed as secondary Marigold waste (SMW). It is essential to address SMW as degrading flower releases toxic gases such as methane (CH_4), carbon dioxide (CO_2), ammonia (NH_3), and others, which generate a terrible odour when dumped in the open [23]. To grow flower, a variety of chemical fertilisers are utilised, so leachate from decomposing waste can seep the ground and contaminate groundwater. As a result, improper management of secondary waste material (SMW) from industries or laboratories may leads to air, water, and soil pollution [24].

Hence, after investigated whether it was possible to use these SMW and turn them into something with more worth. It is found that chemically cellulose, hemicellulose, and lignin make up the majority of SMW [25]. Plant biomass' lignocellulosic structure is widely known as a significant carbon source for the creation of porous carbon composites[26-28]. Recently, attention has been drawn to porous carbon as an intriguing material for a variety of uses, such as electrode material in electrochemical devices[28], [29]. Due to the ongoing decline in the supply of fossil fuels, the use of carbon compounds obtained from waste or biomass has recently become exciting for a variety of applications, notably for energy storage[30].

Numerous researchers have reported that high surface area activated carbon with excellent energy storage capabilities can be made from a variety of sources, including lotus pollen[31], sunflower seeds [32], silk protein [33], watermelon [34], hemp [35], cow dung [36], oil palm[37], yoghurt [38], eggshell membrane [39], coffee beans [40], human hairs [41], and others. The majority of these materials are unusual and tricky to locate. It would therefore be beneficial and more useful if activated carbon could be made from inexpensive, abundant, but discarded materials like SWM. Plant biomass can be transformed into products with a high carbon content using the thermochemical process known as hydrothermal carbonization (HTC)[42-44].

Here, the recycling of most ignored secondary waste is carried out to derive porous carbon for energy storage application without any residual waste. The evolution of Marigold flower to porous carbon can be seen in fig. 1. The HTC and pyrolysis techniques were employed to synthesize porous carbons using SMW as a precursor. Both temperature and time used in HTC strongly affect physical and chemical properties as well as porous structure. The carbon produced has an amorphous phase. The prospect of using microporous carbons made from discarded SMW as positive electrode materials in ZBHSC is investigated using various characterization techniques.

2. Experimental Section

2.1. Synthesis of material

The Secondary marigold floral waste was collected from the oils and dye laboratory where marigold waste was used for extracting oils and dye. The secondary waste is washed with DI water and dried in a hot oven at 80 °C for 30 h. Later, for hydrothermal carbonization (HTC), 20 g of dried secondary marigold material with 100 ml of DI water loaded in a Teflon-lined stainless-steel autoclave and HTC was performed at 190 °C for 24 h. The obtained hydrochar was washed and dried. The collected product designated as hydrothermally carbonized Marigold (HCM). Then following pyrolysis process was carried out in a tube furnace at 800 °C for 1 h with a heating rate of 10 °C/min under Argon (Ar) gas flow (0.3 L/min). The resultant product was crushed into a fine powder using a mortar and pestle. The obtained product named as hydro-pyro-carbonized Marigold (HPCM) to be implied as positive electrode for hybrid supercapacitor.

2.2. Electrochemical characterization

To understand electrochemical behaviour of HPCM material as cathode in hybrid supercapacitor system, a suspension of 10 mg of HPCM in DI water (10 ml) was sonicated for 1 hour in a bath sonicator. The HPCM slurry was then spin coated on carbon paper and dried for 12 hours in a furnace at 80°C. Glass fibre membrane was used as a separator, zinc foil (0.25 mm thickness) was used as an anode, and 2M $ZnSO_4$ was used as the electrolyte for ZIBs to examine the electrochemical properties of HPCM as a cathode for ZIBs. With a NOVA (Metrohm AUTOLAB) potentiostat galvanostat on a Metrohm (PGSTAT 204) electrochemical impedance spectroscopy (EIS), galvanostatic charge-discharge (GCD), and cyclic voltammetry (CV) measurements were studied.

1.3. Material characterization

The structure of HPCM was investigated using X-ray Diffraction (Bruker D8 Advance, Bruker, Germany) with Cu K-α radiation (k =1.54 Å) and a scanning range of 10-80˚ is maintained. Raman spectrum analysis was performed using an argon ion to excite a confocal LabRAM HR800 spectrometer (Horiba Jobin-Yvon, France.) with an excitation wavelength of 532 nm and a wavenumber range of 500-2500 cm^{-1} for HPCM. The surface area measurements were carried out using Brunauer–Emmett–Teller (BET) (BELSORP-miniX, Microtrac, Japan). The field emission scanning electron microscopy (FESEM) and energy dispersive X-ray analysis (EDX) (Supra 55, Carl Zeiss, Germany) were performed for HCM and HPCM.

3. Results and discussion

3.1 Material characterization

The X-ray diffraction pattern (XRD) of HCM and HPCM is shown in Fig.2(a), Two broad peaks in the XRD can be seen for hydrocarbonized secondary marigold waste before and after pyrolysis at 25.63° and 43.41°, which are reflections from planes (002) and (101), respectively. These peaks suggest material has hexagonal graphitic structure [45], [46]. Remarkably, there are small yet important differences in the intensity of the major peak around 25.63°. With pyrolysis, a sharper peak is apparent in the XRD for HPCM sample synthesized in this study. Raman spectra (Fig. 2(b)) reveal details on molecular vibrations and the composition of the material. It is commonly used to describe carbonaceous materials' structural characteristics. The peaks at 1347 and 1591 cm^{-1} denote D and G bands of carbon, respectively. The G band relates to the vibration of sp^2 linked atoms in a two-dimensional hexagonal lattice, while the D band is attributed to defects. The degree of graphitization is calculated using the peak intensity ratios of the D and G band, represented as I_D/I_G. The I_D/I_G ratio is 0.33 for HCM while after annealing at 800˚ C, the I_D/I_G ratio is 1.06 for HPCM material, which suggests the presence of a disordered carbon matrix.

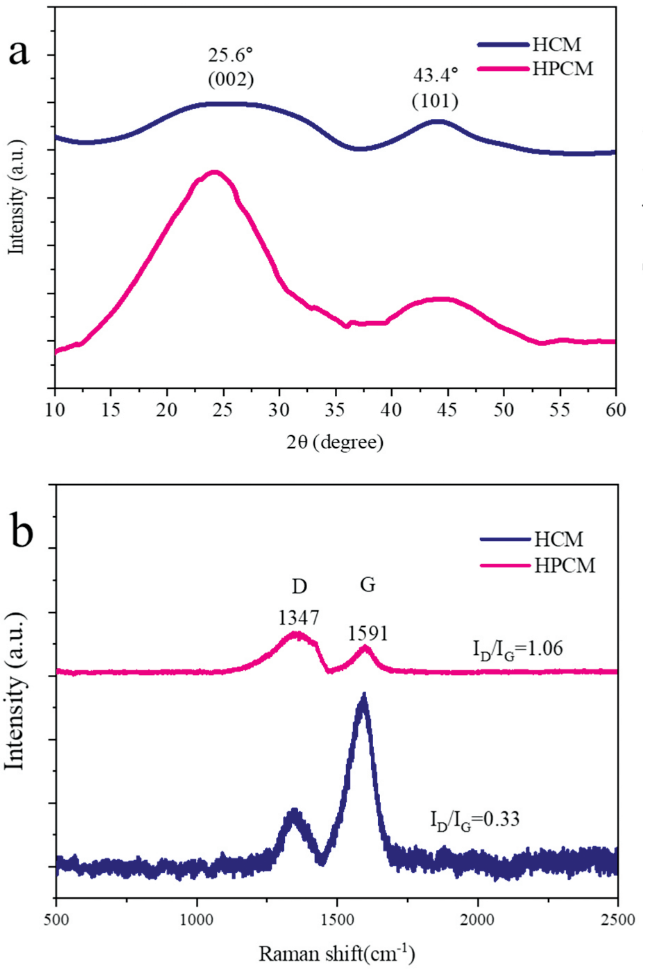

Fig. 2a) XRD pattern and b) Raman spectras for HCM and HPCM

The BET analysis is a crucial characterization technique used to evaluate the specific surface area and porosity of materials, which are essential properties influencing their performance in various applications, including catalysis, adsorption, and energy storage. In this study, BET adsorption and desorption measurements were conducted using nitrogen (N_2) as the adsorbate to investigate the surface characteristics of materials HCM and HPCM shown fig. 3(a). HPCM exhibits a significantly higher BET surface area of 258 m^2/g, nearly 175 times greater than that of HCM (1.47 m^2/g). Fig. 3(b) shows the pore size distribution for HCM and HPCM. It can be noted that extensive surface area of HPCM is complemented by an optimal average pore size of 2.3 nm, which, along with the diverse range of pores, enhances its ability to accommodate Zn ions and electrolyte. In comparison, material HCM, with an average pore size of 2.9 nm, offers a slightly larger pore structure but with a considerably lower surface area. While the larger pores in HCM material may benefit applications requiring more straightforward diffusion pathways, its limited surface area reduces the number of active sites available for surface interactions. This makes HCM less effective in applications where high surface area and optimal pore size distribution are critical. The varied pore sizes in HPCM facilitate efficient ion diffusion and storage, making it particularly suitable for energy storage applications such as batteries and supercapacitors. Therefore, due to its combination of high surface area and a more favourable pore size distribution, HPCM material is more suitable for energy storage applications.

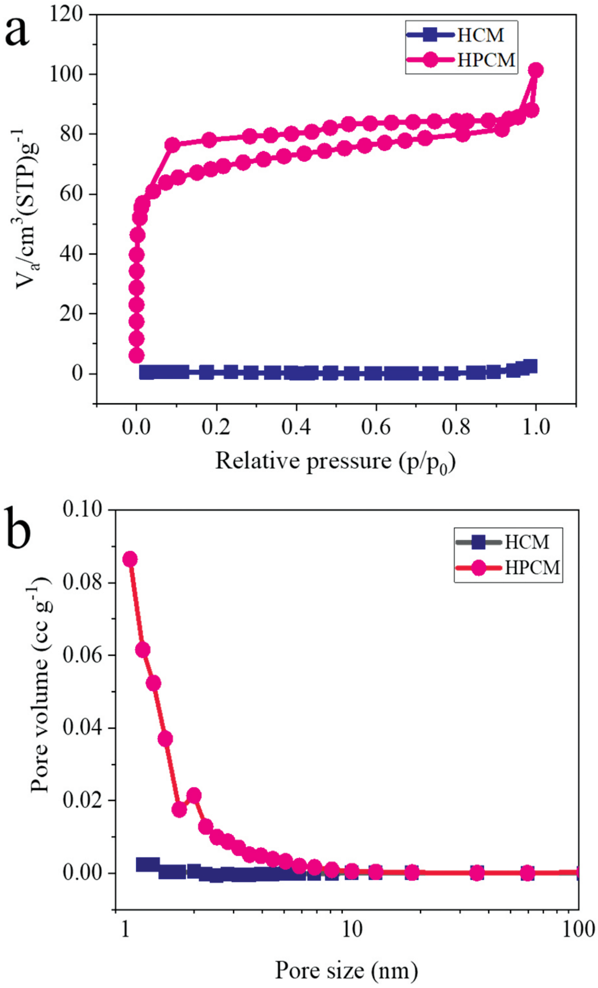

Fig. 3.a) BET surface area adsorption-desorption isotherm of CF with all prepared ratios in N^2 atmosphere at 77 k. a) Pore size distribution

The FESEM was conducted to investigate the surface morphology and structural characteristics of HCM and HPCM materials. The FESEM images reveal distinct differences between the two samples, particularly in their surface textures and pore structures. In fig. 4(a), HCM exhibits a relatively smooth surface with few visible pores, indicating a more compact and less porous structure. The surface morphology suggests that HCM may have a lower surface area, consistent with the BET analysis, which showed a smaller specific surface area. The uniformity in the surface structure of HCM indicates fewer surface defects, which could influence its performance in applications requiring minimal surface reactivity. In contrast, HPCM displays a much more complex and heterogeneous surface morphology. The FESEM images fig 4(b) show that HPCM has undergone carbonization, possesses a network of pores of varying sizes distributed across its surface. This porous structure is characteristic of carbonized lignocellulose, suggesting that HPCM retains the fibrous and hierarchical structure of its precursor material. The carbonization process appears to have enhanced the surface roughness and created a diverse pore structure, contributing to the higher surface area observed in the BET analysis. The presence of different sizes of pores indicates that HPCM can offer superior performance in applications requiring high surface interactions, such as energy storage or catalysis, where a well-developed porous network is advantageous.

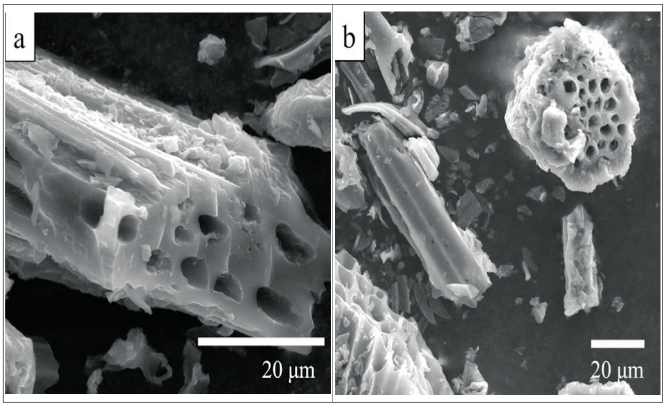

Fig. 4.FESEM images at 20 μm scale a) HCM and b) HPCM

3.2 Electrochemical characterization

In order to analyse the entire electrochemical response of the electrode material, including the charge holding capacity and charge storage behaviour, electrochemical analysis is crucial. To study the electrochemical response of zinc-based hybrid supercapacitor (ZBHSC) using HPCM as positive electrode, zinc foil as negative electrode and 2M $ZnSO_4$ as electrolyte in Swagelok cell was used. Fig. 5 shows the illustration of reaction mechanism for hybrid supercapacitor. Reversible ion adsorption/desorption on HPCM cathode and Zn (Zn^{2+}) deposition/stripping on Zn anode enable the ZBHSC to repeatedly store/deliver electrical energy.

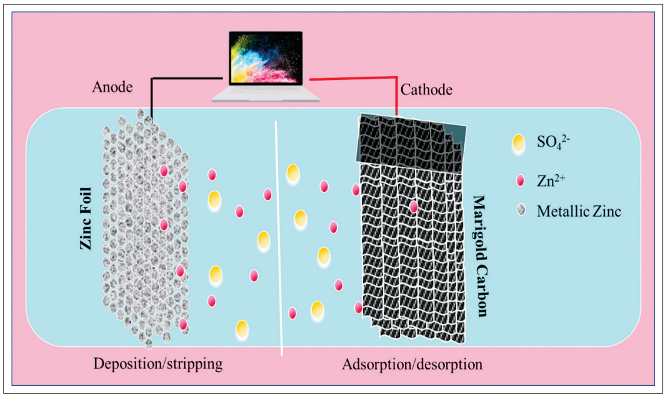

Fig. 5. The illustration of Zn/HMPC hybrid supercapacitor

Fig. 6(a) shows the cyclic voltammogram obtained (CV) at various scan rates ranging from 1 to 350 mV s^{-1} in the potential window of 0.2-1.8 V. The quasi- rectangular shape of the CV curve suggests the combined contribution of both capacitive and diffusion storage mechanism. The relation between the current and the scan rate was described by using equation, $i = av^b$, where i is the current, v is the scan rate, a and b are the adjustable parameters[47]. The value of b ranges from 0-1. Fig. 6(b) show the log i (current) versus log v (scan rate) plot for HPCM sample at oxidation and reduction peaks which is resulted from CV. The obtained values for b_o (oxidation process) and b_r (reduction process) for HPCM are 0.71 and 0.72, respectively. According to the previous studies, b=0.5 stands for diffusion (intercalation) controlled process, while b=1 shows capacitive process. Hence, it confirms that our study indicates that the catalyst exhibits capacitive as well as diffusion process which plays an important role in the storing capacity. Fig. 6(c) shows EIS study,

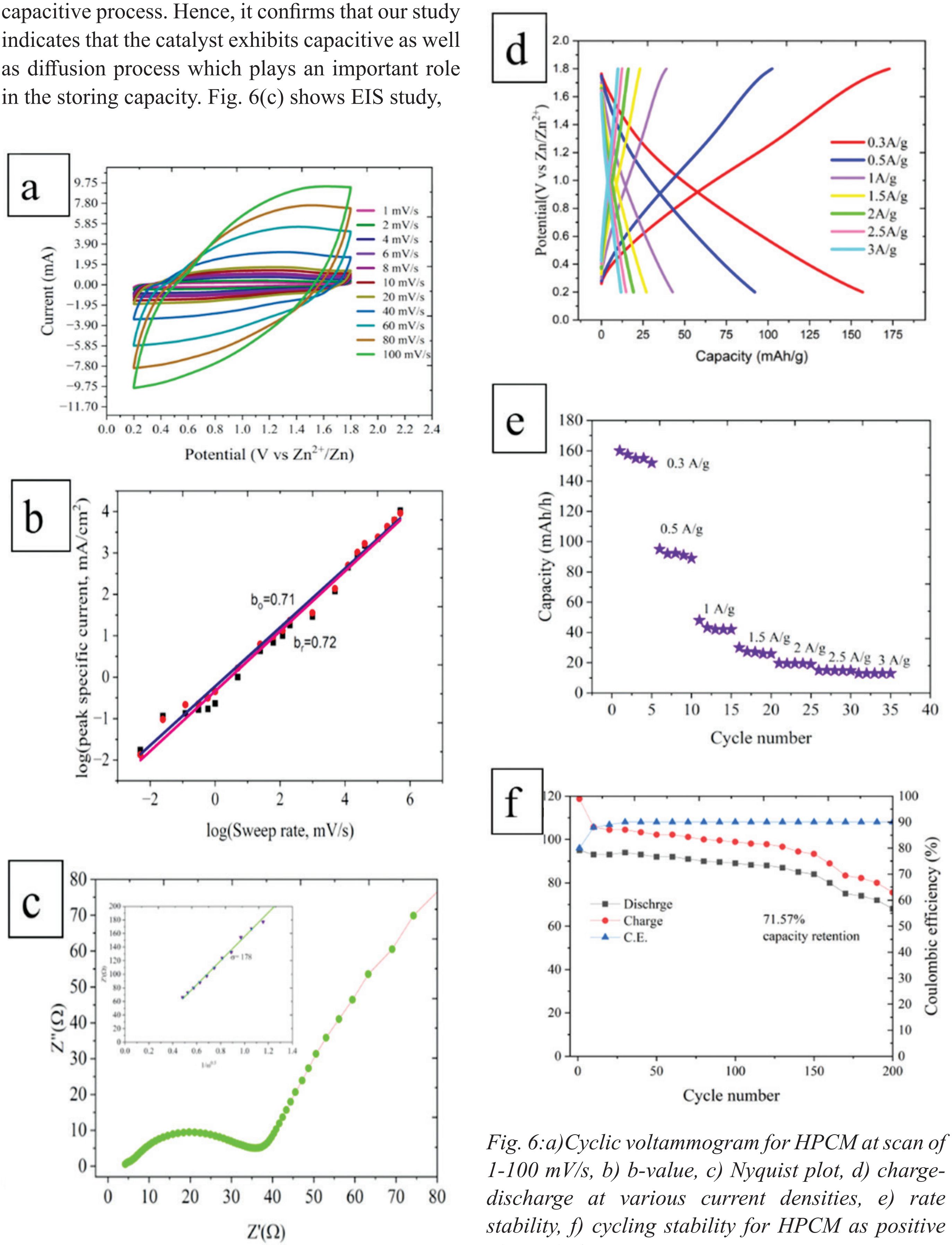

Fig. 6:a)Cyclic voltammogram for HPCM at scan of 1-100 mV/s, b) b-value, c) Nyquist plot, d) charge-discharge at various current densities, e) rate stability, f) cycling stability for HPCM as positive electrode for ZBHSC.

R_s represents the solution resistance, Rct indicates the charge-transfer resistance at the interfaces, and Z_w denotes the Warburg impedance associated to the diffusion of Zn^{2+} ions in equivalent circuit diagram. The Rct value for the HPCM is 26.32 Ω, Rs value is 3.68 Ω, and Z_w value is 178.

Fig. 6(d), display the charge/discharge curves of the HPCM based ZBHSC for the range of current densities from 0.3 to 3 A g^{-1} over the potential window of 0.2-1.8 V. The specific capacity obtained from charge-discharge curve are displayed at different current densities (0.3 to 3 A g^{-1}) are shown in fig. 6(e). At lower current density like 0.3 A g^{-1}, HPCM electrodes exhibit discharge capacity of 157.44 mAh g^{-1}, as current density increases, capacity decreases to 92.13, 42.92, 27.34, 18.85, 15.03,11.76 mAh g^{-1} for current densities of 0.3, 0.4, 0.5, 1, 1.5, 2, 2.5, and 3 A/g, respectively. Further, in order to demonstrate stability HPCM electrodes were charge/discharge at 0.5 A/g for 200 cycles. HPLC shows the capacity retention of 71.57 % and coulombic efficiency of 90.17% (Fig. 6(f)) which confirms the electrochemical stability of HPLC as cathode for ZBHSC. The cell exhibits a peak energy density of 56 Wh/kg at a power density of 106 W/kg, indicating its capability to store substantial energy while delivering moderate power. Additionally, it achieves an exceptional power density of 1.07 kW/kg at an energy density of 4.18 Wh/kg, highlighting its ability to deliver high power output under conditions of lower energy storage. This combination of performance metrics underscores the zinc ion hybrid supercapacitor versatility in applications requiring both high energy storage and rapid energy delivery. The future work includes working on improving specific capacity, cycling stability and capacity retention. This can be achieved by activating carbon and incorporating additional functional group to enhance electrochemical performance of secondary waste derived Marigold carbon which would be used in future green and cost-effective electrochemical device for large-scale production.

4. Conclusions

Secondary marigold flowers waste was effectively transformed into porous carbons by HTC and pyrolysis processes. Due to dehydration and decarboxylation at a high pyrolysis temperature, all functional groups were eliminated after the reaction. After treatment SMW converted to HPCM used as positive electrode showed attractive capacity of 157.44 mAh g^{-1} at 0.3 A g^{-1}. The ZBSC designed using HPCM as positive electrode displayed attractive the capacity retention of 71.57 % and coulombic efficiency of 90.17% over 200 cycles. The developed ZBHSC demonstrates a remarkable balance between energy and power capabilities, achieving a peak energy density of 56 Wh/kg at 106 W/kg and an outstanding power density of 1.07 kW/kg at 4.18 Wh/kg, making it highly versatile for diverse energy storage applications.

Acknowledgments

The authors are thankful to the CSIR (SRF/RA- 2023), AICTE-ADF 2019. We would also like to thank SAIF IIT, Bombay for Material Characterization.

References

[1] J. B. Goodenough, “Electrochemical energy storage in a sustainable modern society,” 2014. doi: 10.1039/c3ee42613k.

[2] Q. Liu, H. Wang, C. Jiang, and Y. Tang, “Multi-ion strategies towards emerging rechargeable batteries with high performance,” 2019. doi: 10.1016/j.ensm.2019.03.028.

[3] M. Armand and J. M. Tarascon, “Building better batteries,” 2008. doi: 10.1038/451652a.

[4] B. Dunn, H. Kamath, and J. M. Tarascon, “Electrical energy storage for the grid: A battery of choices,” 2011. doi: 10.1126/science.1212741.

[5] D. Pakulski *et al.*, “Novel Keplerate type polyoxometalate-surfactant-graphene hybrids as advanced electrode materials for supercapacitors,” *Energy Storage Mater*, vol. 17, 2019, doi: 10.1016/j.ensm.2018.11.012.

[6] G. Zhang, X. Ou, C. Cui, J. Ma, J. Yang, and Y. Tang, "High-Performance Cathode Based on Self-Templated 3D Porous Microcrystalline Carbon with Improved Anion Adsorption and Intercalation," *Adv Funct Mater*, vol. 29, no. 2, 2019, doi: 10.1002/adfm.201806722.

[7] C. Jiang *et al.*, "A Multi-Ion Strategy towards Rechargeable Sodium-Ion Full Batteries with High Working Voltage and Rate Capability," *Angewandte Chemie - International Edition*, vol. 57, no. 50, 2018, doi: 10.1002/anie.201810575.

[8] J. Li, F. Hong, R. Xie, and P. Cheng, "Pore scale simulation of evaporation in a porous wick of a loop heat pipe flat evaporator using Lattice Boltzmann method," *International Communications in Heat and Mass Transfer*, vol. 102, 2019, doi: 10.1016/j.icheatmasstransfer.2019.01.008.

[9] B. Li *et al.*, "Nitrogen-doped activated carbon for a high energy hybrid supercapacitor," *Energy Environ Sci*, vol. 9, no. 1, 2016, doi: 10.1039/c5ee03149d.

[10] V. Aravindan, J. Gnanaraj, Y. S. Lee, and S. Madhavi, "Insertion-type electrodes for nonaqueous Li-ion capacitors," 2014. doi: 10.1021/cr5000915.

[11] S. Fleischmann *et al.*, "High voltage asymmetric hybrid supercapacitors using lithium- and sodium-containing ionic liquids," *Energy Storage Mater*, vol. 16, 2019, doi: 10.1016/j.ensm.2018.06.011.

[12] F. Wang *et al.*, "Highly reversible zinc metal anode for aqueous batteries," *Nat Mater*, 2018, doi: 10.1038/s41563-018-0063-z.

[13] R. J. Gummow, G. Vamvounis, M. B. Kannan, and Y. He, "Calcium-Ion Batteries: Current State-of-the-Art and Future Perspectives," 2018. doi: 10.1002/adma.201801702.

[14] H. Wang, Z. Wang, P. Bai, S. Hu, Y. Zhang, and R. Wang, "Optimized segmented heat source for the numerical simulation of welding-induced deformation in large structures," *Advances in Engineering Software*, vol. 117, 2018, doi: 10.1016/j.advengsoft.2017.12.005.

[15] L. Dong *et al.*, "Extremely safe, high-rate and ultralong-life zinc-ion hybrid supercapacitors," *Energy Storage Mater*, vol. 13, 2018, doi: 10.1016/j.ensm.2018.01.003.

[16] J. Hao *et al.*, "Toward High-Performance Hybrid Zn-Based Batteries via Deeply Understanding Their Mechanism and Using Electrolyte Additive," *Adv Funct Mater*, vol. 29, no. 34, 2019, doi: 10.1002/adfm.201903605.

[17] X. Dai, F. Wan, L. Zhang, H. Cao, and Z. Niu, "Freestanding graphene/VO2 composite films for highly stable aqueous Zn-ion batteries with superior rate performance," *Energy Storage Mater*, vol. 17, 2019, doi: 10.1016/j.ensm.2018.07.022.

[18] G. G. Yadav *et al.*, "Understanding the Effect of Zinc and Achieving Long Cycle Life in Cu-Intercalated Bi-Birnessite/Zinc Batteries," *ECS Meeting Abstracts*, vol. MA2017-02, no. 2, 2017, doi: 10.1149/ma2017-02/2/171.

[19] X. Zeng, J. Hao, Z. Wang, J. Mao, and Z. Guo, "Recent progress and perspectives on aqueous Zn-based rechargeable batteries with mild aqueous electrolytes," 2019. doi: 10.1016/j.ensm.2019.04.022.

[20] . S. and S. Choudhary, "REVIEW PAPER ON -ECOFRIENDLY PRACTICE IN TEMPLE TO MAKE SUSTAINABLE APPROACH TOWARD SOCIAL AND ENVIRONMENT," *International Journal of Technical Research & Science*, vol. 6, no. VI, 2021, doi: 10.30780/ijtrs.v06.i06.002.

[21] A. Sharma *et al.*, "Insights into rapid composting of paddy straw augmented with efficient microorganism consortium," *International Journal of Recycling of Organic Waste in Agriculture*, vol. 3, no. 2, 2014, doi: 10.1007/s40093-014-0054-2.

[22] M. S. Waghmode, A. B. Gunjal, N. N. Nawani, and N. N. Patil, "Management of Floral Waste by Conversion to Value-Added Products and Their Other Applications," 2018. doi: 10.1007/s12649-016-9763-2.

[23] M. B. Kulkarni and P. M. Ghanegaonkar, "Methane enrichment of biogas produced from floral waste: A potential energy source for rural India," *Energy Sources, Part A: Recovery, Utilization and Environmental Effects*, vol. 41, no. 22, 2019, doi: 10.1080/15567036.2019.1571126.

[24] S. Kumari, R. Kothari, V. Kumar, P. Kumar, and V. v. Tyagi, "Kinetic assessment of aerobic composting of flower waste generated from temple in Jammu, India: a lab-scale experimental study," *Environmental Sustainability*, vol. 4, no. 2, 2021, doi: 10.1007/s42398-021-00179-5.

[25] F. H. Isikgor and C. R. Becer, "Lignocellulosic biomass: a sustainable platform for the production of bio-based chemicals and polymers," *Polym Chem*, vol. 6, no. 25, 2015, doi: 10.1039/c5py00263j.

[26] N. Mohamad Nor, L. C. Lau, K. T. Lee, and A. R. Mohamed, "Synthesis of activated carbon from lignocellulosic biomass and its applications in air pollution control - A review," 2013. doi: 10.1016/j.jece.2013.09.017.

[27] J. Wang *et al.*, "Biomass derived carbon for energy storage devices," 2017. doi: 10.1039/c6ta08742f.

[28] L. Wang and X. Hu, "Recent Advances in Porous Carbon Materials for Electrochemical Energy Storage," 2018. doi: 10.1002/asia.201800553.

[29] Z. Yang *et al.*, "Recent Advancement of Nanostructured Carbon for Energy Applications," 2015. doi: 10.1021/cr5006217.

[30] A. M. Abioye and F. N. Ani, "Recent development in the production of activated carbon electrodes from agricultural waste biomass for supercapacitors: A review," 2015. doi: 10.1016/j.rser.2015.07.129.

[31] Y. Jin, K. Tian, L. Wei, X. Zhang, and X. Guo, "Hierarchical porous microspheres of activated carbon with a high surface area from spores for electrochemical double-layer capacitors," *J Mater Chem A Mater*, vol. 4, no. 41, 2016, doi: 10.1039/c6ta05872h.

[32] W. Xing *et al.*, "Superior CO2 uptake of N-doped activated carbon through hydrogen-bonding interaction," *Energy Environ Sci*, vol. 5, no. 6, 2012, doi: 10.1039/c2ee21653a.

[33] Y. S. Yun *et al.*, "Microporous carbon nanoplates from regenerated silk proteins for supercapacitors," *Advanced Materials*, 2013, doi: 10.1002/adma.201204692.

[34] R. J. Mo *et al.*, "Activated carbon from nitrogen rich watermelon rind for high-performance supercapacitors," *RSC Adv*, 2016, doi: 10.1039/c6ra10719b.

[35] H. Wang *et al.*, "Interconnected carbon nanosheets derived from hemp for ultrafast supercapacitors with high energy," *ACS Nano*, 2013, doi: 10.1021/nn400731g.

[36] D. Bhattacharjya and J. S. Yu, "Activated carbon made from cow dung as electrode material for electrochemical double layer capacitor," *J Power Sources*, vol. 262, 2014, doi: 10.1016/j.jpowsour.2014.03.143.

[37] A. M. Abioye, Z. A. Noorden, and F. N. Ani, "Synthesis and Characterizations of Electroless Oil Palm Shell Based-Activated Carbon/Nickel Oxide Nanocomposite Electrodes for Supercapacitor Applications," *Electrochim Acta*, 2017, doi: 10.1016/j.electacta.2016.12.101.

[38] M. Wahid, G. Parte, D. Phase, and S. Ogale, "Yogurt: A novel precursor for heavily nitrogen doped supercapacitor carbon," *J Mater Chem A Mater*, 2015, doi: 10.1039/c4ta06068g.

[39] Z. Li *et al.*, "Carbonized chicken eggshell membranes with 3D architectures as high-performance electrode materials for supercapacitors," *Adv Energy Mater*, 2012, doi: 10.1002/aenm.201100548.

[40] T. E. Rufford, D. Hulicova-Jurcakova, Z. Zhu, and G. Q. Lu, “Nanoporous carbon electrode from waste coffee beans for high performance supercapacitors,” *Electrochem commun*, 2008, doi: 10.1016/j.elecom.2008.08.022.

[41] W. Qian *et al.*, “Human hair-derived carbon flakes for electrochemical supercapacitors,” *Energy Environ Sci*, 2014, doi: 10.1039/c3ee43111h.

[42] B. Hu, K. Wang, L. Wu, S. H. Yu, M. Antonietti, and M. M. Titirici, “Engineering carbon materials from the hydrothermal carbonization process of biomass,” 2010. doi: 10.1002/adma.200902812.

[43] S. K. Hoekman, A. Broch, and C. Robbins, “Hydrothermal carbonization (HTC) of lignocellulosic biomass,” *Energy and Fuels*, vol. 25, no. 4, 2011, doi: 10.1021/ef101745n.

[44] N. Chaiammart, S. Wongcharoen, A. Eiad-Ua, T. Ishizaki, and G. Panomsuwan, “Transformation of waste marigold flowers into porous carbons via hydrothermal carbonization,” in *Key Engineering Materials*, 2019. doi: 10.4028/www.scientific.net/KEM.824.23.

[45] Z. Xie, W. Guan, F. Ji, Z. Song, and Y. Zhao, “Production of biologically activated carbon from orange peel and landfill leachate subsequent treatment technology,” *J Chem*, vol. 2014, 2014, doi: 10.1155/2014/491912.

[46] S. Sonal, P. Prakash, B. K. Mishra, and G. C. Nayak, “Synthesis, characterization and sorption studies of a zirconium(IV) impregnated highly functionalized mesoporous actIVated carbonsb,” *RSC Adv*, vol. 10, no. 23, 2020, doi: 10.1039/c9ra10103a.

[47] S. Khamsanga, R. Pornprasertsuk, T. Yonezawa, A. A. Mohamad, and S. Kheawhom, “δ-MnO2 nanoflower/graphite cathode for rechargeable aqueous zinc ion batteries,” *Sci Rep*, vol. 9, no. 1, pp. 1–9, 2019, doi: 10.1038/s41598-019-44915-8.

A Three-Dimensional Numerical Simulation of CO_2 Gas Bubble Transport at Anode in PEM Based Electrochemical Methanol Reformer

Yasodhar Surabattula , R. Balaji *, K.Ramya,

Centre for Fuel Cell Technology,
International Advanced Research Centre for Powder Metallurgy and New Materials (ARCI), IITM Research Park, Chennai, 600113, India
*Corresponding author Email: rbalaji@arci.res.in (R. Balaji).

Abstract

The accumulation of generated carbon dioxide(CO_2) gas bubbles at the anode flow channels during the operation of PEM based Electrochemical Methanol Reformer (ECMR) may influence the diffusion of reactants to reach its electrocatalytic sites and its performance. Hence, it is imperative to understand the gas-liquid interaction at the anode side of the ECMR. For the first time in the literature, we are reporting a 3D, unsteady, turbulent VOF model on aqueous methanol electrolyzer. In this study, numerical simulation of two-phase flow in the PEM based ECMR is studied to understand the CO_2 gas transportation at the flow channels using volume of fluid (VOF) method. We have considered two conventional flow channel types, namely parallel flow channel (PFC) and serpentine flow channel (SFC). Results show that serpentine flow channels are better in terms of effective gas removal at different operating current densities. The simulation results obtained in this study are compared with the experimental results available in the literature, and they are in good agreement with each other. The influence of liquid feed rate and contact angle on the serpentine flow channel are also studied. The simulation results show that the VOF method, along with the modelling strategy employed in this study, can be used to simulate the gas-liquid interactions even under turbulent conditions for different flow channels of the ECMR cell.

Keywords: *Hydrogen, Electrolyzer, Computational fluid dynamics (CFD), lectro Chemical Methanol reformer, Volume of fluids (VOF)*

---

1. Introduction

Hydrogen is considered as a clean energy carrier, which can be produced from various methods like steam reforming of natural gas, biogas fermentation, and water electrolysis. A significant portion of the hydrogen in the globe is produced by steam reformation of hydrocarbons and gasification of coal[1,2]. The 'cleanest way' to produce on-site hydrogen is electrolysis of water, if coupled with the electricity derived from renewable sources like solar energy, wind energy. Proton exchange membrane (PEM) based electrolysis is one of the advanced technologies which can offer pure hydrogen production with modular designs and high efficiency. It is well known that the practical PEM water electrolysis consumes about more than 5.0 kWhr of energy to produce per cubic meter of hydrogen, which makes this process economically unattractive except in niche areas.

PEM based Electrochemical Methanol Reformation (ECMR) is a method that combines aspects of both the processes of electrolysis and reformation. If the required electrical potential is supplied across two electrodes separated by a solid electrolyte, high pure hydrogen can be produced. The energy required to harvest the same amount of hydrogen is less than the PEM based water electrolysis [3–5]. The hydrogen produced from this process is free from carbon dioxide and carbon monoxide. This method comes with the advantage of the elimination of the external purification system, usually employed in the reformation process.

Figure1 describes the components and function of PEM based ECMR cell. During DC power is supplied, aqueous methanol is circulated at the anode side of the cell, and it produces CO_2 at the anode, and hydrogen gas is evolved at the cathode. The electrochemical reactions at electrodes can be expressed as

Anodic reaction : $CH_3OH + H_2O \rightarrow CO_2 + 6H^+ + 6e-$ (1)
Cathodic reaction : $6H^+ + 6e- \rightarrow 3H_2$ (2)
Overall reaction : $CH_3OH + H_20 \rightarrow CO_2 + 3H_2$ (3)

The anodic reaction taking place at ECMR is similar to that of the anodic reaction of the Direct Methanol Fuel cell (DMFC). The performance of ECMR also depends on the effective removal of produced CO_2 bubbles from the anode outlet. Otherwise, it could choke the flow channel of aqueous methanol and increase the fuel concentration gradient along the flow channel and may hinder the electrochemical reaction. Hence, studying the interaction between aqueous methanol and carbon dioxide is very important while designing of the electrolyzer flow field plate pattern in a way to minimize the mass transport issues on the anode side of the ECMR cell.

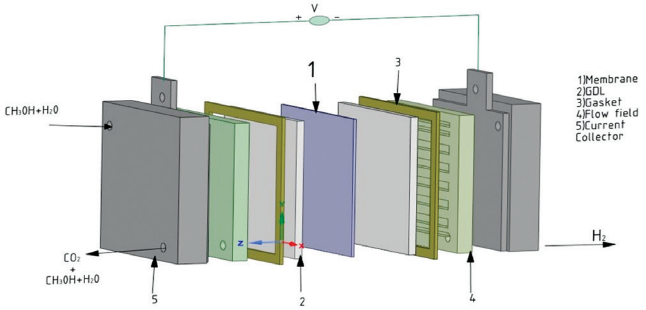

Fig. 1. Schematic of methanol-water solution electrolysis

In the literature, various studies have been carried out to understand the liquid and gas interaction in PEM based fuel cell system using advanced techniques like X-ray radiography, Particle image velocimetry (PIV) [6–9]. Yang et al. studied the influence of different flow field designs on the DMFC performance using a transparent cell setup. They observed that the DMFCs designed with the single serpentine flow fields (SSFF) resulted in improved performance than those with the Parallel flow fields (PFF). They also reported the channel blockages by produced CO_2 gas bubbles in the PFFs, at high currents and low liquid feed rate; however, this phenomenon was not observed in the SSFF [10]. T. Hutzenlaub et al. reported the influence of wetting properties on the bubble dynamics of DMFC. They compared hydrophobic and hydrophilic flow channels; they found a low-pressure drop in the case of hydrophilic flow channels. The critical fuel velocity to detach the bubble depends on the bubble length [11]. Yuan.W et al. experimentally examined the behavior of two-phase flow dynamics with temperature on the anode side of DMFC using a transparent cell. Further, in the case of PEM based water electrolyzer, the two-phase flow phenomena were studied in the literature using above similar techniques like optical characterization, X-ray radiography, neutron tomography [12–17].

Furthermore, the various computational techniques have also been employed to study the water-gas dynamics in PEM based system. To illustrate the interface dynamics and bubble visualization, techniques such as the pore - network (PN), the level set (LS) and the Volume of fluids (VOF) methods are used. In this, The VOF method is widely used in PEM fuel cells/water electrolyzer to study liquid-gas interaction [16-21]. Kang et al. [20] successfully simulated bubble generation in a 'T' junction channel using VOF methods and found that, high liquid viscosities resulted in the small bubble slugs along the channel, this could be due to the stronger shear force from the fluid. They have also validated with experimental results. Kang et al. [21] also employed the VOF method to track, the gas-liquid interface in parallel channels of DMFC considering flow type as laminar with the limited active area of 96 sq.mm. Shu yuan et.al studied the bubble evolution and transport processes as well as the mechanisms of how bubbles impact the PEMWE Performance [22]. The micro Gas bubble dynamics and two-phase flow are visualised by in-situ high-speed camera coupled with a specific design in PEM based water electrolyser [23].

The above literture study shows the significance of flow field designs and interaction of gas and liquid within the cell on the performance of PEM based fuel cell/electrolyzer. However, in the case of the PEM based ECMR cell, the electrodes are porous in nature and flow type, which occurs within the cell would be turbulence in nature. Hence, this methodology should be validated for larger active areas and un-study turbulent flows that develop at the outlet. In the present study, we have adopted a similar methodology as proposed by Kang et al. [21], to study the bubble generation in ECMR for a larger area of 900 sq.mm with two different flow channels (parallel and serpentine design) using 3D unsteady, and turbulent flow conditions. Simulation results are compared with experimental results from literature published by Yuan et al [24].

2. Numerical model description

2.1. Volume of Fluid (VOF) method

VOF is proposed by Hirt C.W [25], which is suitable for simulation of immiscible fluids and provides the information between the interface of the mixture's phases, for example, the fraction of gas as shown in Fig.2. In the present study, it has been employed to track the gas-liquid interface at anode side of ECMR cell and investigate the bubble behavior within the flow channel.

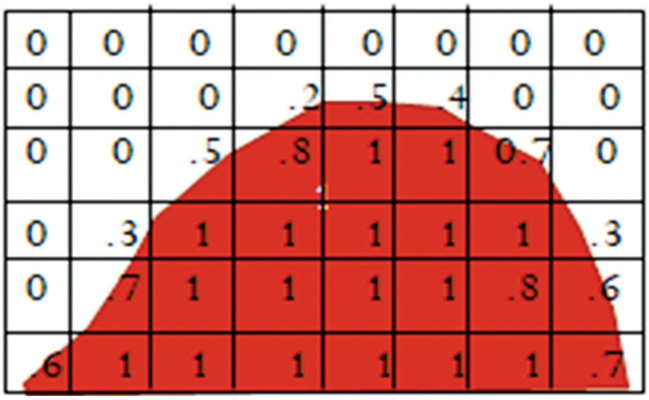

0	0	0	0	0	0	0	0
0	0	0	.2	.5	.4	0	0
0	0	.5	.8	1	1	0.7	0
0	.3	1	1	1	1	1	.3
0	.7	1	1	1	1	.8	.6
.6	1	1	1	1	1	1	.7

Fig. 2. Fraction of volume of the fluid

2.2. Multiphase flows in ECMR

Similar to the other PEM based systems, understanding of multiphase flow phenomena in ECMR is crucial for better design of the cell to improve performance and efficiency. Initially, an attempt has been made to study the interaction between supplied aqueous methanol (liquid) and generated carbon dioxide (gas) and its removal efficiency under various feed rate of reactant. In ECMR cell, aqueous methanol is supplied through the flow channels and diffuses into the gas diffusion layer (GDL) and reaches the electrocatalyst layer (CL). The evolved carbon dioxide at the electrocatalyst layer diffuses back into the flow channel through the GDL, flowing against the fresh feed aqueous methanol. This gas-liquid interaction causes a two-phase flow scenario in the ECMR. The VOF method is employed in this study to simulate the bubble generation inside the flow channels of the reactant distribution plate.

2.3. Computational domain description

The ECMR anode is consisted by flow field channels and a porous electrode layer. In this uniform porous electrode layer contains 0.1mm thick catalyst layer (CL) on top of the 0.3mm gas diffusion layer (GDL), which is directly linked with the flow channel, as shown in Figure 3.

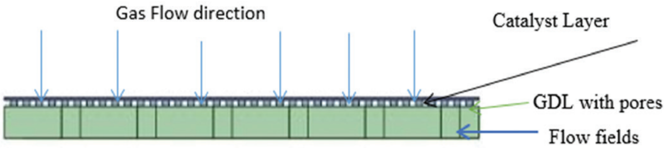

Fig. 3. A schematic describing different parts of the domain

The entire GDL consist of square holes (0.4mm × 0.4mm) and its spacing between adjacent holes is maintained as 1 mm from its middle point. Figure 4 shows the domains of the serpentine and parallel flow channel used in this study. There are thirteen serpentine flow channels in the entire active area of 900 sq.mm, which has 1.2 mm width and 1.5mm depth per channel, rib width, and other geometric details of flow channels are listed in Table 1.

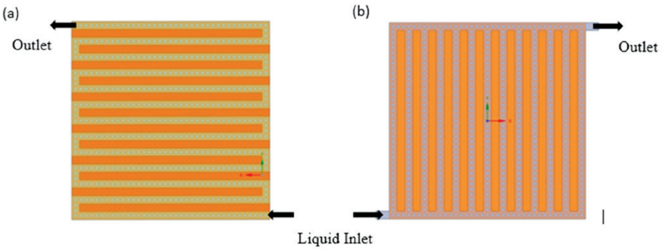

Fig. 4. (a) Serpentine flow channel (b) Parallel flow channel flow domains used in study

Table 1: Geometric parameters of two flow field patterns

Parameters	Serpentine	Parallel	Units
Effective area	900	900	mm^2
Channel width	1.2	1.2	mm
Channel depth	1.5	1.5	mm
Channel length	39	3	mm
Rib width (mm)	1.2	1.2	mm

3. Mathematical Model

In the present study, FLUENT 19.1 is used to simulate the two-phase, unsteady and three-dimensional flows with the VOF method. The VOF tracks interface between gas and liquid by solving the continuity equation for the volume fraction in individual cells for one of the phase q. and its equation can be expressed as follow:

$$\frac{\partial(\alpha_q \rho_q)}{\partial t} + \nabla \cdot (\alpha_q \rho_q \vec{v}_q) = 0 \tag{4}$$

Here α_q is the volume fraction of the fluid q in a cell. The pressure jump is considered across the interface; the velocity field is considered as continuous. The equation for conservation of mass eq.5 and momentum eq.6 are expressed as follow:

$$\frac{\partial \rho}{\partial t} + \nabla \cdot \rho\vec{v} = 0 \tag{5}$$

$$\frac{\partial\ (\rho\vec{v})}{\partial t} + \nabla \cdot (\rho\vec{v}\vec{v}) = \nabla p + \nabla \cdot [\mu(\nabla\vec{v} + \nabla\vec{v}^{T})] + \rho\vec{g} + \vec{F} \tag{6}$$

Here ρ is density, $\vec{v}$ is velocity and, p is static pressure, and μ is dynamic viscosity.

The density and viscosity in the above equations are calculated by using the following equations for two fluids with densities (ρ_1, ρ_2) and viscosities (μ_1,μ_2)

$$\rho = \alpha_2\, \rho_2 + (1-\alpha_2)\rho_1 \tag{7}$$

$$\mu = \alpha_2\, \mu_2 + (1-\alpha_2)\mu_1 \tag{8}$$

Turbulence: we have considered Menter's Shear Stress Transport (SST) [26] to account the flow turbulence which develops at the outlet,

$$\nabla \cdot \left(\rho\vec{v}k - \left(\mu + \frac{\mu_t}{\sigma_k}\right)\nabla k\right) = P_k - \beta^{*}\rho k\omega + P_{kb} \tag{9}$$

$$\nabla \cdot \left(\rho\vec{v}\omega - \left(\mu + \frac{\mu_t}{\sigma_t}\right)\nabla \omega\right) = \alpha\frac{\omega}{k}P_k - \beta\rho k\omega^2 + P_{\omega b} \tag{10}$$

The more details of the above equations can be found in [19,26].

3.1. Boundary conditions and initial conditions

In the present two-phase simulation, 2.0 M methanol solution is considered as liquid and carbon dioxide is considered as a gas with its properties as listed in Table 2 from the literature [13].

Table 2: Properties of the primary and secondary fluids

Phase	Density(kg/m^3)	Viscosity (Pa s)
Primary phase(liquid)	988	0.001212
Secondary phase(gas)	1.7878	1.37e^{-5}

Multiphase model, surface tension model, formulation, and other parameters are listed in Table 3. Table 4 and Table 5 describes the boundary conditions in different cases. The production rate of carbon dioxide gas is proportional to the operating current density of the electrolyzer. The operating current density is of ECMR is converted into gas inlet velocity at the electrode according the faradays law. The molar flow rate is calculated using the equation 11 and then converted into gas-velocity.

$$\frac{dN}{dt} = \frac{i}{nF} \tag{11}$$

Where i is current density and n is number of electrons and F is the Faraday constant (96,485 C per mole of electron)

Assumptions

In order to reduce the complexity involved during solving governing equations, the following few assumptions are considered. Since the complete 3D numerical modelling of electrolyzer are a highly time consuming and computationally very expensive process.

- Transient flows at isothermal conditions (Room Temperature) are considered, without any electrochemical reactions.
- Crossover of methanol solution from anode to the cathode through the membrane is neglected.
- The generation of CO_2 gas on the surface of the catalyst layer is assumed to be uniform.
- Produced CO_2 gas diffuses through the porous gas diffusion layer and enters into the flow channel.

- The concentration of aqueous methanol is considered uniform across the flow channels.
- Fluids are considered as incompressible and ideal.

3.2. Numerical setup

Table 3 contains the numerical schemes used in this study. The time step size(s) is set at $1x10^{-4}$ S, whereas the total number of time steps is taken as 5000, the simulation time in each case equals to 0.5 seconds. The contact angle between the flow field plate substrate and reactant is set at 120°.

Table 3 List of Models and parameters employed in this study

Parameter	Model/Value
Multiphase model	VOF
Volume of fraction cut-off	1e-06
Interface modelling type	Sharp
Flow type	Turbulent
Surface tension model	Continuum surface force
Formulation	Implicit
Pressure-Velocity coupling scheme	PISO
Wall adhesion	Enabled
Contact angle	120^o

Initially, the influence of cell operating current density on gas bubble behaviour was studied with the flow field plate having serpentine and parallel flow channels at the condition listed in Table 4. Further, the influence of the liquid feed rate and contact angle was also studied with the serpentine flow channel at different conditions, as listed in Table 5. To validate the results, the Isosurfaces of gas volume fraction (0.001) at time 0.5 s are compared with the results obtained from experimental visualization studies in the literature [24].

Table 4 Boundary and initial conditions for cases 1, 2 and 3

Case No	Liquid feed rate (ml min^{-1})	Liquid-inlet velocity (m s^{-1})	Current density (mA cm^{-2})	Gas inlet velocity (m s^{-1})
1	1	$9.259x10^{-3}$	20	$1.25x10^{-5}$
2	1	$9.259x10^{-3}$	60	$3.75x10^{-5}$
3	1	$9.259x10^{-3}$	100	$6.25x10^{-5}$

Table 5: Boundary conditions and initial conditions for cases A, B, C and D

Case No.	Liquid feed rate (ml min^{-1})	Liquid-inlet velocity (m s^{-1})	Current density (mA cm^{-2})	Gas inlet velocity (m s^{-1})
A	0.1	$9.259x10^{-4}$	80	$5x10^{-5}$
B	0.3	$2.777x10^{-3}$	80	$5x10^{-5}$
C	0.6	$5.555x10^{-3}$	80	$5x10^{-5}$
D	0.8	$7.407x10^{-3}$	80	$5x10^{-5}$

4. Results and discussions

4.1. Effect of Current density on gas bubble behaviour

The influence of applied current density on the flow of gas bubbles distribution in serpentine flow channels is studied. From the figure 5, it can be observed that fewer gas bubbles are formed at a lower current density of 20 mA/cm^2 and a further increase in current density to 60 mA/cm^2, the generated CO_2 gas bubbles are travels through porous electrode layer to reach its flow channel. At some places, it is also observed the smaller gas bubbles are merged and forming larger bubbles, especially towards at the outlet of the flow channel. At the higher current density operation (100 mA/cm^2), large size gas bubbles are observed in the channels. The coalesce of small bubbles turned into big gas slug towards the outlet of the channel, which may result in poor supply for fresh reactant. The above-observed results are in decent pact with experimental visualization results obtained by Wei Yuan et al. for DMFC[24].

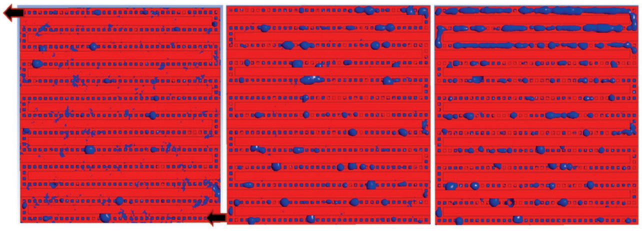

(a) 20 mA/cm-2 (b) 60 mA/cm-2 (c) 100mA/cm-2

Fig.5. Simulation results on Gas bubble behaviour in serpentine flow channel

Figure 6. Shows the gas bubbles distribution pattern observed at different current density with a serpentine flow channel. The above similar gas bubble distribution pattern was observed up to 60 mA/cm^2 forming smaller gas slugs in the

channels. It is increased drastically while operating at 100mA/cm^2, which is comparatively higher than the distribution behaviour observed with the parallel flow channel. Further, it is also observed that the distribution of gas slugs is higher only at last two channels in the case of the serpentine flow channel, but in the parallel flow channel, the slugs are distributed almost at entire flow channels area, which leads blocking effect of reactant resulting lower performance of the electrolyzer.

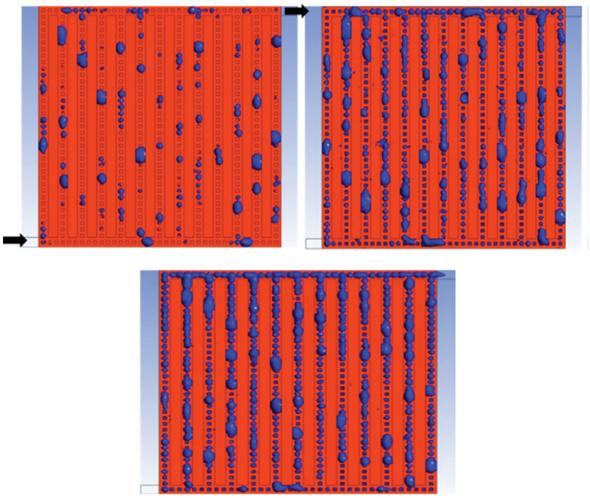

Fig. 6. Simulation results on gas bubble behaviour in parallel flow channel

(a) 20 mA/cm^2 (b) 60 mA/cm^2 (c) 100mA/cm^2

The pressure drop characteristics of the flow field pattern were studied and results are presented in figure 7. The higher-pressure drop is observed for serpentine flow channel pattern when compared to parallel flow channel pattern and it may be attributed to the right angel corner nature of the serpentine pattern. The increase in current density results in large gas slugs on the channel, which are responsible for the increase in flow resistance creating a high pressure drop in each case. Hence further study on the influence of flow rate of reactant and contact angle on gas bubble distribution was confined only with the serpentine flow channel pattern.

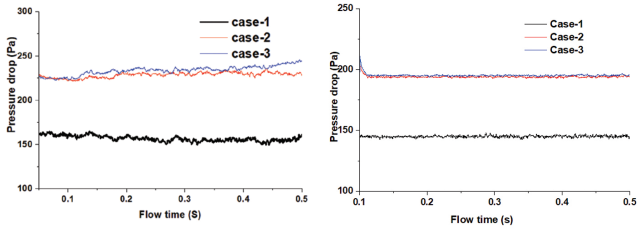

Fig. 7. Pressure difference between the outlet and the inlet of (a) Serpentine and (b) parallel flow channel for various cases.

4.2. Effect of reactant feed rate on gas bubble behaviour

The influence of reactant feed rate on gas bubbles distribution behaviour at the current density of 80 mA/cm^2 was studied and the results are shown in figure 8. The feed rate was varied up to 0.8 ml/min to ascertain its effect on gas bubble growth and evolvement precisely. The smaller gas bubbles are formed and attached to the walls of the flow channel at 0.1 ml/min. Further increase in flow rate at 0.3 ml/min the shape of the CO_2 gas bubbles is changed and moves away from the wall surface due to an increase in force created by the liquid flow. Upon further increase in liquid feed rate to 0.8 ml/min, it helps in effective removal of gas by forming a gas slug resulting in more areas can be exposed for methanol transportation for electrochemical reaction. It will increase the mass transfer efficiency while operating electrolyzer.

The pressure drops observed at different reactant feed rates (shown in fig 9) in different cases, as listed in table 5. The pressure drops increases with increasing feed rate and it may be attributed to the increase in flow velocity at higher feed rate resulting in the formation of gas slug.

In the Case-A, the flow rate is very less and low-pressure drop is observed, when the flow rate is increased the increase in flow velocity causes the gas bubbles to form a gas slug, the formation of slug results in higher pressure drop.

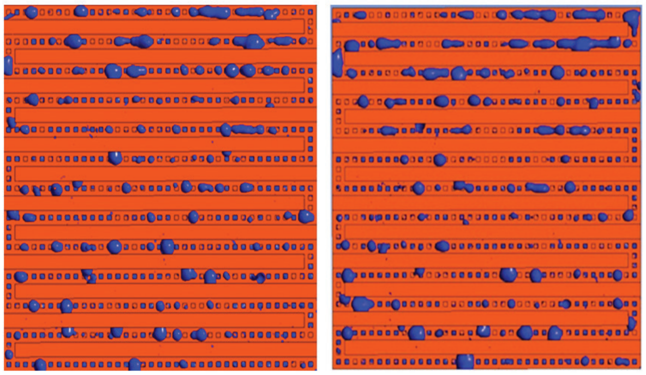

0.1 ml/min 0.3 ml/min

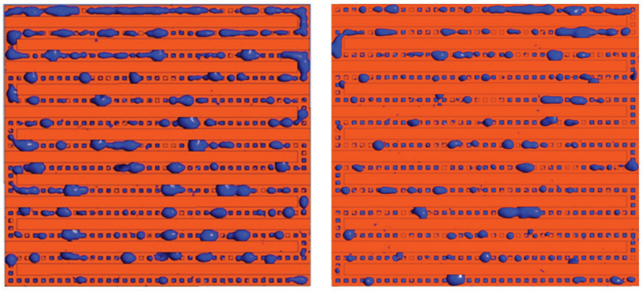
0.6 ml/min 0.8 ml/min

Fig.8 Gas bubble behaviour in serpentine flow channel at various flow rates

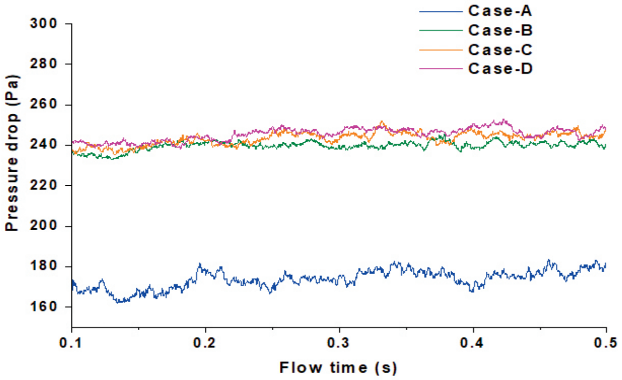

Fig. 9. Pressure drop in the Serpentine flow channel for various cases, as listed in Table 5.

4.3. Influence of contact angle on gas bubble behaviour

It is very essential to study the influence of the bipolar plate surface's nature on the performance of the electrolyzer. Bipolar plates can be made up of different materials; the contact angles of these bipolar plates may fall between the hydrophobic and hydrophilic regions. To understand the effect of contact angle on the gas-dynamics, three different contact angles, 70°, 90°, and 120°, are considered for the studies with the serpentine flow channel. The applied current density and reactant feed rate were considered as 100 mA cm^{-2} and 1 ml/min, respectively. Figure.10 shows that the increase in contact angle results in a more sluggish flow of gas bubbles. The bubble formation process can be identified into three distinct stages termed (1) nucleation stage, (2) growth stage, and (3) detachment stage The influence of contact angle on each stage of bubble formation are important by analysing the evolution of interface equilibrium and force balance conditions [27]. The bubble size increases with increasing contact angle and the nucleation stage becomes negligible compared to the other two stages. That's because with the contact angle increasing, the growth stage is more dominant compared to the nucleation stage inducing the smaller gas bubbles to coalesce and form gas slugs near the outlet of the serpentine flow channel, as shown in the Fig.10(C). Further, it also increases the pressure drop on the more hydrophobic surface, as seen in Figure 11.

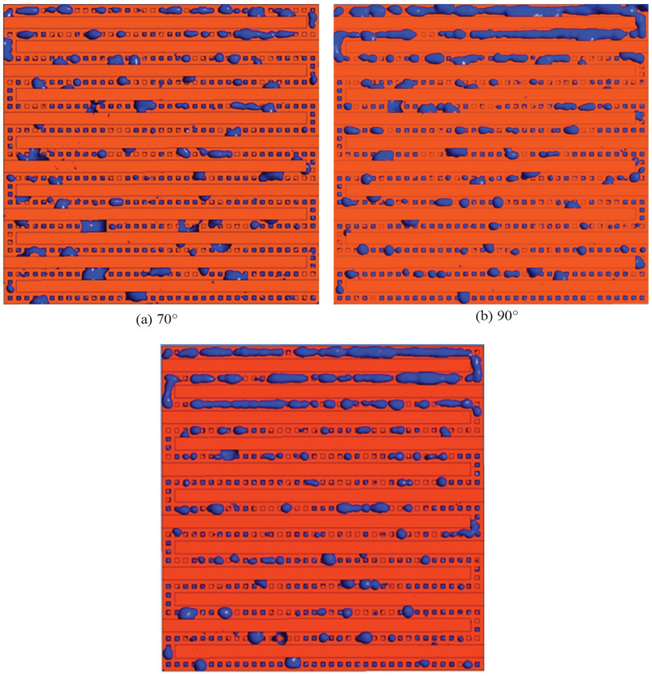
(a) 70° (b) 90°

(c) 120°

Fig.10 The effect of gas bubble behaviour in a serpentine flow channel under different contact angles with the wall surface

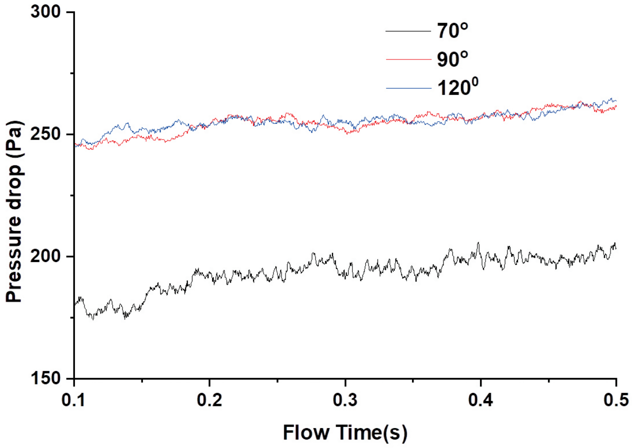

Fig. 11. Pressure drop in the Serpentine flow channel under different contact angles with the wall surface.

5. Conclusions

In the present study, the interaction of feed aqueous methanol and evolved Carbon dioxide (gas)-in PEM based ECMR cell was analysed using three dimensional, transient, turbulent VOF model employing Fluent 19.1 software. In order to reduce the complexity of the modelling, the electrochemical reactions are neglected and only the anode side gas-liquid interactions in the porous electrode layer and flow channels are considered. The influence of applied current density is studied in two different flow channel patterns (serpentine and parallel). Further, the effect of aqueous methanol feed rate and contact angle on the serpentine flow channel is also simulated and the important findings of this study are summarised below:

- In both parallel and serpentine designs, the pressure drops (inlet to outlet) increases with an increase in applied current density (i.e., the rate of production of carbon dioxide gas).
- At higher current densities (i.e., at case -2 and case-3), larger gas bubbles are observed across the channels on the parallel flow channel design, whereas in the case of serpentine design, large gas slugs are seen only at the channels near to the outlet.
- The comparative study between serpentine and parallel flow channels confirms that serpentine flow channel design performs better in terms of the removal of CO_2 bubbles from the porous surface of the electrode effectively.
- The effective removal of carbon dioxide gas bubbles is seen at a higher contact angle between the flow field plate substrate and feed reactant at the expense of a higher pressure drop.

This numerical study is aimed to understand the gas bubble and liquid interaction in PEM based ECMR cell and detailed numerical model, which can predict the entire performance of the ECMR cell are underway and would be published in the future.

Acknowledgement

The authors would like to thank The Director, ARCI, for his constant support and encouragement and the Department of Science and Technology, Government of India, for financial assistance. Yasodhar Surabattula thanks ARCI for the ARCI fellowship under which this work was carried out.

References

[1] M. Carmo, D.L. Fritz, J. Mergel, D. Stolten, A comprehensive review on PEM water electrolysis, Int. J. Hydrogen Energy. 38 (2013) 4901–4934. https://doi.org/10.1016/j.ijhydene.2013.01.151.

[2] H. Ju, S. Badwal, S. Giddey, A comprehensive review of carbon and hydrocarbon assisted water electrolysis for hydrogen production, Appl. Energy. 231 (2018) 502–533. https://doi.org/10.1016/J.APENERGY.2018.09.125.

[3] D.Gang, S.Park, J.Min Yoo, M.Gu, Electrochemical Reforming of Methanol using Multilayer Nanoarchitectonics with Ligand Exchange-Induced Layer-by-Layer Assembly toward Electrocatalytic Hydrogen Production. *ACS Appl. Energy Mater.* 7, 10, (2024) 4572–4580.

https://doi.org/10.1021/acsaem.4c00653

[4] N Manjula, R Balaji, K Ramya, N Rajalakshmi., Hydrogen production by electrochemical methanol reformation using alkaline anion exchange membrane based cell Int. J.Hydrogen Energy 45 (17), (2020) 10304-10312.

https://doi.org/10.1016/j.ijhydene.2019.08.202

[5] S.Menia, H.Tebibel, F.Lassouane, A.Khellaf ,I.Nouicer, Hydrogen production by methanol aqueous electrolysis using photovoltaic energy: Algerian potential, Int. J.Hydrogen Energy 42 , (2017) 8661-8669

https://doi.org/10.1016/j.ijhydene.2016.11.178

[6] A. Bazylak, Liquid water visualization in PEM fuel cells: A review, Int. J. Hydrogen Energy. 34 (2009) 3845–3857. https://doi.org/10.1016/J.IJHYDENE.2009.02.084.

[7] Z.W. Dunbar, R.I. Masel, Magnetic resonance imaging investigation of water accumulation and transport in graphite flow fields in a

polymer electrolyte membrane fuel cell: Do defects control transport?, J. Power Sources. 182 (2008) 76–82. https://doi.org/10.1016/J.JPOWSOUR.2008.03.057.

[8] J. Lee, J. Hinebaugh, A. Bazylak, Synchrotron X-ray radiographic investigations of liquid water transport behavior in a PEMFC with MPL-coated GDLs, J. Power Sources. 227 (2013) 123–130. https://doi.org/10.1016/J.JPOWSOUR.2012.11.006.

[9] S.-G. Kim, S.-J. Lee, A review on experimental evaluation of water management in a polymer electrolyte fuel cell using X-ray imaging technique, J. Power Sources. 230 (2013) 101–108. https://doi.org/10.1016/J.JPOWSOUR.2012.12.030.

[10] H. Yang, T.S. Zhao, Effect of anode flow field design on the performance of liquid feed direct methanol fuel cells, Electrochim. Acta. 50 (2005) 3243–3252. https://doi.org/10.1016/j.electacta.2004.11.060.

[11] T. Hutzenlaub, N. Paust, R. Zengerle, C. Ziegler, The effect of wetting properties on bubble dynamics and fuel distribution in the flow field of direct methanol fuel cells, J. Power Sources. 196 (2011) 8048–8056. https://doi.org/10.1016/j.jpowsour.2011.05.070.

[12] I. Dedigama, P. Angeli, N. van Dijk, J. Millichamp, D. Tsaoulidis, P.R. Shearing, D.J.L. Brett, Current density mapping and optical flow visualisation of a polymer electrolyte membrane water electrolyser, J. Power Sources. 265 (2014) 97–103. https://doi.org/10.1016/J.JPOWSOUR.2014.04.120.

[13] S. Sadeghi Lafmejani, A.C. Olesen, S.K. Kaer, Analysing Gas-Liquid Flow in PEM Electrolyser Micro-Channels, ECS Trans. 75 (2016) 1121-1127. https://doi.org/10.1149/07514.1121ecst.

[14] O.F. Selamet, U. Pasaogullari, D. Spernjak, D.S. Hussey, D.L. Jacobson, M.D. Mat, Two-phase flow in a proton exchange membrane electrolyzer visualized in situ by simultaneous neutron radiography and optical imaging, Int. J. Hydrogen Energy. 38 (2013) 5823-5835. https://doi.org/10.1016/j.ijhydene.2013.02.087.

[15] M.A. Hoeh, T. Arlt, N. Kardjilov, I. Manke, J. Banhart, D.L. Fritz, J. Ehlert, W. Luke, W. Lehnert, In-Operando Neutron Radiography Studies of Polymer Electrolyte Membrane Water Electrolyzers, ECS Trans. 69 (2015) 1135-1140.

https://doi.org/10.1149/06917.1135ecst.

[16] M.A. Hoeh, T. Arlt, I. Manke, J. Banhart, D.L. Fritz, W. Maier, W. Lehnert, In operando synchrotron X-ray radiography studies of polymer electrolyte membrane water electrolyzers, Electrochem. Commun. 55 (2015) 55-59. https://doi.org/10.1016/j.elecom.2015.03.009.

[17] J.O. Majasan, J.I.S. Cho, I. Dedigama, D. Tsaoulidis, P. Shearing, D.J.L. Brett, Two-phase flow behaviour and performance of polymer electrolyte membrane electrolysers : Electrochemical and optical characterisation, Int. J. Hydrogen Energy. 43 (2018) 15659–15672. https://doi.org/10.1016/j.ijhydene.2018.07.003.

[18] P. V Suresh, S. Jayanti, Effect of air flow on liquid water transport through a hydrophobic gas diffusion layer of a polymer electrolyte membrane fuel cell, Int. J. Hydrogen Energy. 35 (2010) 6872–6886. https://doi.org/10.1016/j.ijhydene.2010.04.052.

[19] R.B. Ferreira, D.S. Falc, Numerical simulations of two-phase flow in proton exchange membrane fuel cells using the volume of fluid method - A review, J. Power Sources 277 (2015) 329–342

[20] S. Kang, B. Zhou, Numerical study of bubble generation and transport in a serpentine channel with a T-junction, Int. J. Hydrogen Energy. 39 (2014) 2325–2333. https://doi.org/10.1016/j.ijhydene.2013.11.115.

[21] S. Kang, B. Zhou, M. Jiang, Bubble behaviors in direct methanol fuel cell anode with parallel design, Int. J. Hydrogen Energy. 42 (2017) 20201–20215. https://doi.org/10.1016/j.ijhydene.2017.06.149.

[22] S. Yuan, Zhao, X.Cai, L. An, S.Shen, X.Yan J. Zhang, Bubble evolution and transport in PEM water electrolysis: Mechanism, impact, and management. Progress in Energy and Combustion Science 96 (2023) 101075,1-36.

https://doi.org/10.1016/j.pecs.2023.101075

[23] Y.Li, Z.Kang, J.Mo, G.Yang, S. Yu,D.A. Talley, Bo Han, F.Zhang In-situ investigation of bubble dynamics and two- phase flow in proton exchange membraneelectrolyzer cells. Int.J.Hydrogen Energy 43(2018) 11223-11233.

https://doi.org/10.1016/j.ijhydene.2018.05.006

[24] W. Yuan, A. Wang, Z. Yan, Z. Tan, Y. Tang, H. Xia, Visualization of two-phase flow and temperature characteristics of an active liquid-feed direct methanol fuel cell with diverse flow fields, Appl. Energy. 179 (2016) 85–98. https://doi.org/10.1016/j.apenergy.2016.06.127.

[25] C. W. Hirt, B. D. Nichols, Volume of Fluid (VOF) Method for the Dynamics of Free Boundaries*, J. Comput. Phys. 39 (1981) 201–225. https://doi.org/10.1007/s40998-018-0069-1.

[26] F.R. Menter, Two-equation eddy-viscosity turbulence models for engineering applications, AIAA J. 32 (1994) 1598–1605. https://doi.org/10.2514/3.12149

[27] J.Yuan, Y.Li ,Y.Zhou, “Effect of contact angle on bubble formation at submerged orifices.J Mater Sci 49 (2014) 8084–8094.

https://DOI 10.1007/s10853-014-8516-5

PROFORMA OF SUBSCRIPTION FORM

I /We wish to subscribe **The Journal of Electrochemical Society of India (JECSI)** for .... year(s) for which (i) a Demand Draft vide …………..............…… dated …………….............……… issued from (Name of the bank………………………………………................................)favouring **ELECTROCHEMICAL SOCIETY OF INDIA JOURNAL, payable at Bengaluru or (ii) NEFT/IMPS vide UTR no…………………..dated for Rs/US $……………….is enclosed.**

NAME…………………………………………………………………………………………….

DESIGNATION……………………………………………………………………………….

POSTAL ADDRESS…………………………………………………………………………….

…………………………………………………………PIN………………………................

E-MAIL…………………………………………….Phone no.……………………………………

Subscriber ID (for renewal only)……………………………………………………………

Signature……………………….

Bank account details

Name: Electrochemical Society of India Journal

Account No. 110045333254

Bank Name: Canara Bank

Customer ID: 309740255

IFSC Code: CNRB0000683

MICR Code: 560015023

Indian Institute of Science

Canara Bank IISc, Bangalore - 560012

Subscription details:

Print only: For institutions & Individuals: Annual 6 issues: Rs 2000/- (India), Annual 6 issues: USD 250.00 incl. postages (abroad),

For students: Annual 6 issues: Rs 1000/-

Print & Online (customer type: institution):

USD 100.00 & INR 5000.00

Please note that institutional prices are available only for libraries of higher education institutions and research organizations.

Journal of the Electrochemical Society of India

Vol. No. 73 (3&4), April - June 2024
CODEN - JESIA 73 [3&4] 2024 ISSN:0013-466X
Email : ecsiiisc@gmail.com

FROM IV

See Rule VIII

1. Place of publication : Bengaluru

2. Periodicity of its publication : Quarterly

3. Printer name : Poornima Printers

Whether the Citizen of india : YES

Address of the printer : No. 3&4, Sy. No. 51/14, Chowdeshwarinagar,
Pipeline Road, Laggere, Bengaluru - 560058

4. Publishers Name : **The Electrochemical Society of India**

5. Editor's Name : Dr. U. Kamachi Mudali

Whether Citizen of India : Yes

Address : **The Electrochemical Society of India**
Indian Institute of Science Campus,
Bangalore - 560 012

6. Name and Address of Individuals who own the newspaper/holders and partners and shareholders : **The Electrochemical Society of India**
Indian Institute of Science Campus,
Bangalore - 560 012.
holding more than 1% of the total capital.

I, Dr. U. Kamachi Mudali hereby declare that the particulars given above are true to the best of my knowledge and belief.

Sd/-
Dr. U. Kamachi Mudali
Chief Editor, JECSI
(Publisher)

THE ELECTROCHEMICAL SOCIETY OF INDIA

Indian Institute of Science Campus, Bengaluru - 560 012, India
Phone : +91-80-22932613
E-mail : ecsiiisc@gmial.com | www.ecsi.in

CALL FOR NOMINATIONS FOR ECSI AWARDS- 2024

Shri S.K. Seshadri Memorial Mascot National Award
(Instituted in the year 1980)

With a view to stimulate interest among Scientists and Technologists in the field of corrosion, the Electrochemical Society of India has instituted the prestigious "**Shri S. K. Seshadri Memorial Mascot National Award"** for notable and outstanding contributions in the field of Industrial Corrosion. The award is sponsored by Director, M/s. Biosafe Solutions.

1. The research work considered for this award should be in the field of Corrosion Science and Technology, Corrosion Prevention and Allied aspects. Industrial Significance to be highlighted and Industrial applicability is desired.
2. The work should have been carried out to bring it to the point of application. The process of development and test schedules may have been carried out during the preceding couple of years, but should have culminated in a fruitful result. The work need not necessarily have been published.

THE N. M. SAMPAT AWARD - 2024
(Instituted in the year 1986)

With a view to recognize outstanding services rendered to the Electroplating industry andTechnology, the Governing Council of the ECSI has with great pleasure has instituted "**The N. M. Sampat Award".** This award is sponsored by M/S Canning Mitra Phoenix Limited, Mumbai. Research work considered for this award should be in the field of Metal Finishing, Electroplating, Surface Coating and Modification, and allied fields. Work carried out in these areas with possible industrial applicability or academic excellence would be considered. The work need not have been published but industrial applications should have been established.

ECSI- METROHM National Award - 2023
(Instituted in the year 2021)

With a view to recognize the contributions made by individuals in the field of basic electrochemistry, electrochemical instrumentation and devices, theoretical and; experimental electrochemistry, the Electrochemical Society of India has instituted this prestigious award **"ECSI- METROHM National Award for Electrochemical Science".** The award is sponsored by M/s Metrohm India Ltd. Chennai. Meritorious work in any field of Electrochemical Science would qualify for this award.

ECSI- AMARA RAJA National Award- 2023
(Instituted in the year 2021)

With a view to stimulate interest among Scientists and Technologists in the field of Batteries, Fuel Cells and Sensors, the Electrochemical Society of India has instituted the prestigious award **“ECSI- AMARA RAJA National Award for Advanced Electrochemical Technology”.** The award is sponsored by M/s. Amara Raja Batteries Ltd. Tirupathi. Meritorious work in the field of Batteries, Fuel Cells and Sensors would qualify for this award.

ECSI-Dr. K. Elayaperumal National Award- 2023
(Instituted in the year 2022)

With a view to recognize the outstanding contributions of individuals made in the area of Corrosion Mitigation in Industries, The Electrochemical Society of India has instituted the prestigious award “ECSI- Dr. K. Elayaperumal National Award for Excellence in Industrial **Electrochemical Science and Technology”** from this year. The award is sponsored by Dr. K. Elayaperumal and his family. Meritorious work in the area of corrosion mitigation in industries would qualify for this award.

GUIDELINES FOR NOMINATION

1. Nominations may be made by Research Organizations/Institution/ Industries/Individuals.
2. The nomination should be accompanied by the complete bio-data and important contributions for which the nomination is being made.
3. The work should have been carried out to bring it to the point of application. The process of development and test schedules may have been carried out during the preceding couple of years, but should have culminated into a fruitful result at least during the year of application.

Each of the above awards carries a Scroll of Honor and cash prize.

Awardees are required to present their work in the form of an **Award Lecture** and also submit a written manuscript for publication in the Journal of Electrochemical Society of India. Complete Nominations in all respects for the above awards should reach The Secretary, The Electrochemical Society of India, Indian Institute of Science Campus, Bengaluru - 560 012.

Nominations complete in all respects for the above awards should reach
Hon President or General Secretary,
The Electrochemical Society of India, Indian Institute of Science Campus,
Bengaluru - 560 012,
E-Mail: ecsiiisc@gmail.com

on or before 31st of July 2024
The Awards will be presented during the annual
ICONEST-2024 Conference

Dr. S. T. Aruna
Hon. President, ECSI

Dr. Ajay Krishnan
Hon. Gen. Secretary, ECSI

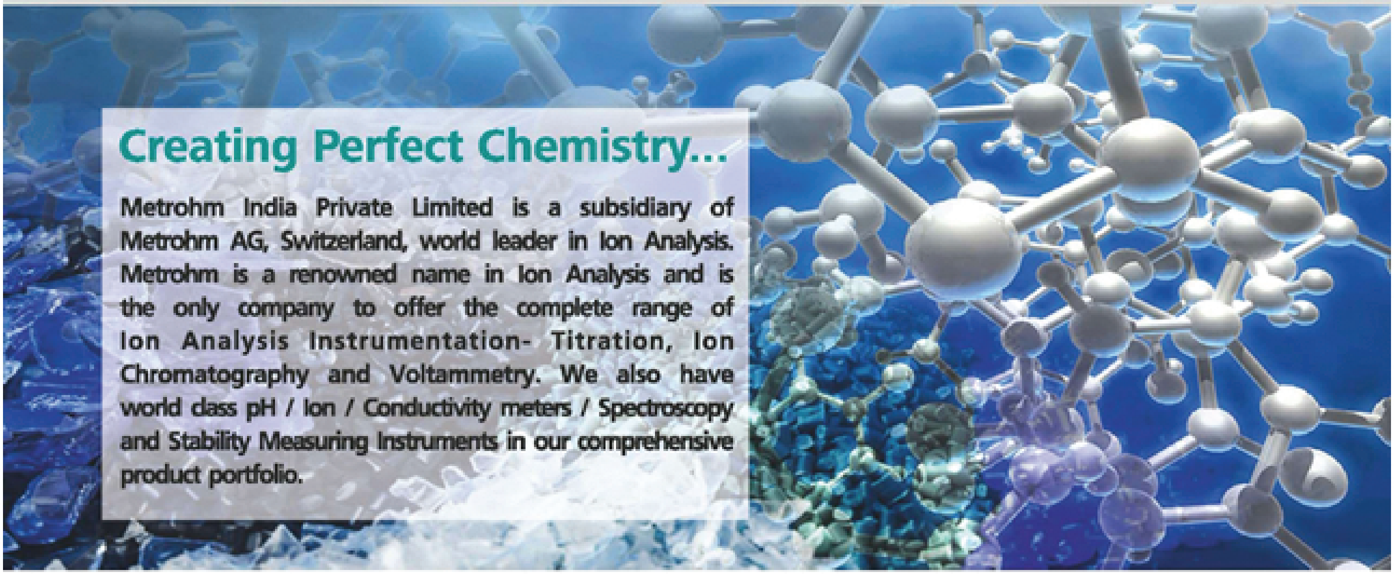

Creating Perfect Chemistry...

Metrohm India Private Limited is a subsidiary of Metrohm AG, Switzerland, world leader in Ion Analysis. Metrohm is a renowned name in Ion Analysis and is the only company to offer the complete range of Ion Analysis Instrumentation- Titration, Ion Chromatography and Voltammetry. We also have world class pH / Ion / Conductivity meters / Spectroscopy and Stability Measuring Instruments in our comprehensive product portfolio.

Titrator

Ion Chromatography

Voltammetry

Electrochemical station

NIRS Analyzer

Raman Spectroscopy

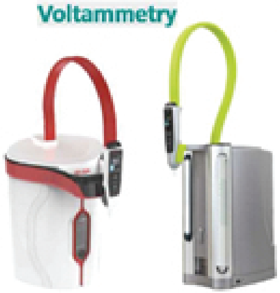

Labwater Purification

Surface Area Analyzer

We also have:

- Electrochemical research instrumentation from Metrohm Autolab
- On-line and at-line process analyzers for process monitoring from Metrohm Process Analytics
- NIR and Raman Spectroscopy solutions from Metrohm and B&W Tek
- Innovative technology for electrochemistry research from Dropsens
- BET surface area, pore size distribution from MicrotracBEL Corp., Japan
- Testing instrumentation for the energy storage device and energy conversion device markets from Arbin instruments
- Lab water solutions from Elga
- Pipetting and dispensing solutions from Socorex

PARTICIPATE IN WATER SURVEY

SCAN ME

GET YOUR FREE GIFT!

Metrohm India Private Limited
Metrohm-SIRI Towers, 3&4, Fourrts Avenue, Annai Indira Nagar
Okkiyam, Thoraipakkam, Chennai - 600097, India.
Ph: +91 44 40440440 | Customer support: +91 44 40440444

For details, e-mail us at **info@metrohm.in** or visit us at **www.metrohm.in**

Metrohm
India Private Ltd.